Prediction of Galloping of Transmission Line Conductors by a Computational Aeroelastic Approach

Amir Borna

Doctor of Philosophy

Department of Mechanical Engineering
McGill University
Montreal, Quebec

May 2014

A Thesis Submitted to McGill University
in Partial Fulfillment of the Requirements of the Degree of
Doctor of Philosophy

DEDICATION

I would like to dedicate this work to my wife, Fatemeh, and son, Benyamin, for their patience, dedication, faith and love.

ACKNOWLEDGEMENTS

I would like to express my deepest appreciation to my supervisor, Professor Wagdi G. Habashi, for his advice, guidance, and financial support during the course of this study. Performing research under his supervision has been a great honor and an opportunity for me to practice team spirit, self-confidence, and world-class deliveries. I thank him also for providing me parallel computing resources, through his account in *CLUMEQ* and *RQCHP* supercomputer facilities, in order to perform the heavy simulations.

I would like also to thank to a great extent my co-supervisor, Professor Ghyslaine McClure, for her invaluable scientific contributions and generous financial support through her research grant from *Le Fonds québécois de la recherche sur la nature et les technologies*. She has always been a great consultant for me with brilliant quotes for life and work. In addition, I express my best appreciation to Professor Siva K. Nadarajah for his inputs in my research. It has been a great opportunity for me to benefit from his technical comments in the earlier stages of the research.

My great gratitude also goes to Newmerical Technologies International (NTI) and its personnel for providing me access to FENSAP-ICE and partial financial support to conclude the study. They have been available for me to consult and provide technical help about FENSAP-ICE. Moreover, I sincerely thank my current and former colleagues and system administrators in the CFD Lab for providing a pleasant and unique group experience in a friendly environment.

Finally, I would like express my eternal appreciation to my father and entire family for their never-ending love, faith, and encouragement during my life. In particular, I am so grateful to my lovely wife who patiently accepted my ups and downs, and accompanied me throughout my graduate study journey.

TABLE OF CONTENT

ABSTRACT

Various types of overhead transmission line vibration instabilities are introduced and their impact on reliability and serviceability of electrical power networks is discussed in detail. By following a historical background, different mechanisms to describe these events, particularly galloping, are investigated and the advantages and drawbacks of each method are discussed. In addition, important factors affecting the galloping and the necessary conditions to expect large instabilities are addressed. In order to overcome the limitations of the current methods, a practical cost-effective computational methodology, with adequate accuracy, is designed to study galloping as an aeroelastic instability problem in two- and three-dimensions for single and bundled conductors subjected to various wind and atmospheric icing conditions. The proposed methodology is a two-way loosely coupled fluid-structure interaction analysis consisting of three key modules: Computational Fluid Dynamics (CFD), Computational Structural Dynamics (CSD), and communication and data-handling modules. The CFD analysis module is based on the Unsteady Reynolds-Averaged Navier-Stokes (URANS) equations and uses the one-equation Spalart-Allmaras turbulence model for the Reynolds stresses. The conductor displacements obtained from the CSD analysis module are handled by the CFD module, using an Arbitrary Lagrangian Eulerian (ALE) formulation. In essence, the CSD module determines the nonlinear dynamic response of the conductors to the unsteady flow loading predicted by CFD analysis at each time increment. The nonlinear equations of the conductor's motion are solved by a direct time-step integration using the second order time-

accurate and unconditionally stable Newmark-Beta operator (trapezoidal rule). Finally, due to the non-matching finite element grids used for fluid and structure discretization, a fast communication module is designed for load and displacement transfer between the CFD and CSD modules. The methodology is validated using the results of different two- and three-dimensional test cases reported in the open scientific literature, and detailed computational predictions of galloping events are presented for different incident wind conditions and ice accretions.

SOMMAIRE

Plusieurs types d'instabilités vibratoires des lignes de transmission aériennes sont présentées et leurs impacts sur la fiabilité et la fonctionnalité des réseaux électriques sont discutés en détail. En suivant la démarche historique des travaux réalisés dans le domaine, les différents mécanismes pour décrire ces phénomènes, en particulier du galop des conducteurs, sont étudiés et les avantages et les inconvénients de chaque méthode sont discutés. Les facteurs déterminants qui affectent le galop et les conditions nécessaires au déclenchement de grandes instabilités sont discutés. Afin de surmonter les limites des méthodes actuelles, une méthodologie de calcul pratique, efficace et suffisamment précise, est proposée pour l'étude du galop posé en tant que problème d'instabilité aéro-élastique bi- ou tridimensionnel, pour des conducteurs simples ou en faisceaux soumis à diverses conditions de vent et de givrage atmosphérique. La méthodologie proposée est basée sur l'analyse par faible couplage bidirectionnel des interactions fluide-structure, composée de trois modules principaux: Mécanique des fluides numérique (MFN ou CFD en anglais), Mécanique des structures numérique (MSN ou CSD en anglais) et un module de communication et de traitement des données servant d'interface entre les deux modules computationnels précédents. Le module CFD est basé sur les équations de Navier-Stokes moyennées et instationnaires (URANS) avec un modèle de turbulence Spalart-Allmaras à une équation. Les déplacements des conducteurs, obtenus à partir du module d'analyse CSD, sont considérés par le module CFD en utilisant une formulation eulérienne-lagrangienne arbitraire (ALE). En substance, le

module CSD détermine la réponse dynamique non-linéaire des conducteurs pour le chargement d'écoulement instationnaire prédit par l'analyse CFD à chaque pas en temps. Les équations non linéaires du mouvement du conducteur sont résolues par une méthode d'intégration directe de second ordre et inconditionnellement stable Newmark-Bêta (règle trapézoïdale). Enfin, en raison de la non-correspondance des maillages d'éléments finis utilisés pour la discrétisation des domaines fluide et solide (air et conducteur glacé), un module de communication rapide est conçu pour le transfert des charges et des déplacements entre les module CFD et CSD. La méthode proposée est validée à l'aide de résultats expérimentaux disponibles dans la littérature, et les prédictions des calculs détaillés du galop sont présentées pour différents angles d'incidence du vent et accumulation de la glace.

LIST OF TABLES

LIST OF FIGURES

CHAPTER 1: INTRODUCTION

Overhead transmission line conductors are flexible structures subject to unsteady wind-induced loading and consequent motion. The dynamic characteristics of such motion, namely its frequency and amplitude, are directly related to the magnitude and frequency of the wind loading and the structural characteristics of the transmission line. These wind-induced motions can be classified as very small amplitudes and high frequency (Aeolian vibrations), small amplitudes and moderate frequency, recognized as oscillations (wake-induced oscillations), and, finally, a self-sustained, high-amplitude, and low frequency flutter instability known as galloping [1-4]. These three motions are also distinguished by other factors such as energy transfer mechanism, type of motion, and different forms of damage to transmission line components. For example, Aeolian vibrations and wake-induced oscillations have moderate to high frequency low-amplitude characteristics that may cause wear and fatigue of conductor components, while large galloping motion, in addition, may cause flashover between adjacent phases, which may lead to power outage and direct cable damage, cable tension increase, dynamic loading on the supporting towers and connecting hardware, and, in extreme situations, cable rupture, structural damage, and tower failure.

1.1 Aeolian Vibrations and Wake-Induced Oscillations

Aeolian vibrations are characterized by very small amplitudes (less than or at most equal to the diameter of the conductor) and high frequencies (between 3 and 150 Hz). In Aeolian vibrations, the motions are related to the small pressure fluctuations applied by the wind on the surface of a conductor. These pressure

fluctuations, present whether the conductor is in motion or not, initiate unsteady vortex shedding behind the bluff body[1] conductor, that detach periodically from either side of the body with a frequency called vortex shedding frequency. These vortices start from the separation point of the flow on the conductor. The separation point differs with Reynolds number (Re) and body shape. For a bare conductor the separation point is around 91° at $\mathrm{Re}=10^{4}$, increasing the Reynolds number moves it upstream: for instance at $\mathrm{Re}=3.9\times10^{4}$, the flow separates at 83° [5]. The vortex shedding frequency is related to the structure through the Strouhal number (St). The Strouhal number varies with Re; however, its variation is limited between 0.15 and 0.3 [6, 7]. When the flow separates and the vortex shedding frequency approaches one of the conductor's resonance frequencies, Aeolian vibration initiates; however, continuity of vibrations, their amplitude, and frequency, depend on energy balance, i.e. energy gained from wind power minus damping ability of the line (self-damping ability or by dampers). As the energy balance increases the amplitude of conductor vibration, the nature of vortex shedding changes and its frequency increases. However, since the conductor's internal damping increases with frequency, the amplitude of the Aeolian vibrations will seldom exceed the diameter of the conductor [8]. Because of this small amplitude, visual detection of Aeolian vibration is difficult, but can be identified by its high frequency noise; a buzzing noise spreading along a telegraph line on a windy day reveals an Aeolian vibration. As the final point, it should be

[1] A bluff structure is one in which the flow separates from large section of the structure's surface such as transmission lines, bridges, heat-exchanger tubes, etc.

noted that from a structural point of view, the amount of loads induced by the Aeolian vibrations on a transmission line structure compared to other loads is negligible.

The second category of the wind-induced motions of the transmission line conductors is called wake-induced oscillations. These oscillations happen when the number of conductors in the transmission line is more than one. These oscillations have larger amplitude (up to three times of the diameter of the conductor) as well as lower frequency (3 to 50 Hz) than Aeolian vibrations. To understand the physics of wake-induced oscillations, it is useful to start with the definition of a wake. When flow passes over a bluff body, at some point the shear stress on the body reaches zero leading to flow separation. Due to flow separation, a disturbed and usually turbulent region with a reversed flow area forms behind the body. This region moves downstream the flow and is called wake. Based on the definition, in the wake-induced oscillation, one conductor should be placed in the wake of another conductor in order to oscillate. Therefore, the wake-induced oscillation is usually linked to the bundle of conductors in which some of the conductors are affected by the wakes of the windward cables. The wakes initiated from a windward conductor travel all the way downstream and reach the other conductors (leeward conductors); therefore, these conductors experience a disturbed fluctuating pressure field and start to oscillate. These oscillations depend mainly on the ratio of the spacing to diameter of the conductors, the sub-span length (distance between spacers), distribution of spacers, and the angle of attack or tilt of the bundle. In addition, ice accretion has a great effect on

developing the wake-induced oscillations. Ice accretion decreases the ratio of the spacing to diameter of conductors and causes an increase in aerodynamic forces on the leeward conductors. Furthermore, ice accretion may increase a negative tilt and can result in placing the leeward conductor in an appropriate position to gain more energy from wind. Thus, ice accretion increases the wake intensity and the strength of oscillations. Finally, it should be noted that the loads induced by wake on structure are greater than the loads caused by the Aeolian vibration but are not so great to worry about structural failure; however, what makes the wake-induced oscillation important is its lower frequency which in case of resonance with one of the structural natural frequencies may lead to the other type of wind-induced motion called galloping; more dangerous phenomenon for structure.

1.2 Galloping

Galloping is a term used by engineers when referring to a one- or multi-degree-of-freedom instability of a bluff structure in crosswinds. The kind of instability in galloping is velocity-dependent and damping-controlled [4, 9, 10]. It means that in a galloping event, a bluff body receives energy supplied by wind, and the effective damping plays an important role to decrease or increase the amplitude of displacements. Effective damping includes both structural and aerodynamic damping, and in order to have an oscillatory instability, it is required to have a negative effective damping. Galloping frequencies observed on overhead conductors range from 0.1 to 1 Hz, and displacement amplitudes and mid span can be up to several times the sag of the conductor [2, 8].

Galloping, if not controlled, can lead to severe events, such as tower failure and blackouts. These events may occur during winter and in remote areas, complicating the repair process. The damages and other impact of transmission line vibrations on reliability and serviceability of electrical power networks are well studied in the literature (e.g. see [1, 2]). Each year, millions of dollars are spent worldwide to repair such damages and/or overcome the cost of subsequent economical impact. Hence, wind-induced motions of conductors, and in particular galloping, are an important consideration in designing transmission lines in geographical regions having severe and stormy winters.

1.3 Ice Accretion and Galloping

Normally, in the case of bare conductors, wind loading, damping, and inertia forces do not impose large motions in the vertical direction, but this changes when atmospheric icing accretes on a conductor [1]. In fact, it is shown that bare smooth-surface cylinders are immune to very large-amplitude, galloping-type oscillations [4], and there are only few galloping cases on bare conductors reported in the literature [8]. Therefore, in almost all of the galloping events, ice accretion and threshold of wind speeds combinations are present. Ice accretion alters the conductor's profile and makes it aerodynamically and/or aeroelastically unstable [1, 3]. Even very small amounts of non-symmetric glaze ice accretion over a conductor can dramatically change the behavior of the transmission line, leading to large galloping instabilities [10, 11]. Ice accretion generally modifies the initial symmetric cross section and its surface roughness and increases the exposed area to incident wind [8], altering the flow pattern, separation points and

vortex shedding. These effects generally result in higher aerodynamic forces and vortex streets and shedding frequencies different from bare conductors. In many instances, the changes in the vortex street due to icing also increase the risk of galloping instability and sub-span oscillations for leeward conductors in bundled phases [10]. Thus, the occurrence of large flutter oscillations, i.e. galloping, is more likely for iced conductors than bare ones, especially when the primary frequency band of loading coincides with the natural frequency of the structure.

1.4 Literature Survey

Predicting conductor galloping, due to its complex mechanism, has been a difficult task ever since overhead lines were erected at the beginning of the last century: Some researchers would call it an "art", while others would call it "inexact science". Galloping is usually initiated by small perturbations and at the earlier stages could be an Aeolian vibration or a wake-induced oscillation. However, in the absence of sufficient damping, either structural or aerodynamic, and by supplying continuous energy by sustained wind or via profile changes caused by ice accretion, the low-amplitude Aeolian vibration or wake-induced oscillation could turn into a galloping event. Different mechanisms are proposed to explain galloping, including the Den Hartog mechanism (aerodynamic approach) and flutter mechanism (aeroelastic approach). The most complete one to date is the aeroelastic approach, in which the structural parameters (frequencies ratio, inertia effect, damping, and stiffness) and aerodynamic loads (lift, drag, and moment) are coupled and actively participate in this instability. In other words, in

this mechanism, galloping is treated as an aeroelastic instability inherently linked to the motion of the bluff body, not solely as an aerodynamic instability.

The first explanation for galloping as an aerodynamic mechanism was presented by Den Hartog [12]. He used a galloping model representing the transverse motion of an elastically mounted airfoil subjected to a uniform and laminar wind flow based on a quasi-steady assumption. He proposed a simple relation between the aerodynamic coefficients and their gradient with respect to the angle of attack in order to predict a negative effective damping condition that would cause the instability of the system. Den Hartog's criterion states that a body is susceptible to gallop in one direction (vertical) when the rate of change of the lift coefficient (C_L) with respect to the angle of attack (α) becomes negative and its value exceeds the drag coefficient (C_D), or simply,

$$\frac{dC_L}{d\alpha} + C_D < 0 \tag{1.1}$$

Since Den Hartog's quasi-steady galloping model was introduced in the early 1930's, a large literature has been generated to understand the various physical aspects of cable galloping. Parkinson [13] was among the first to explain galloping as cross-sectional flow separation and reattachment from bluff bodies (see also [14]). He recognized different classes of galloping and made a significant contribution by studying different parameters affecting the instability, including conductor shape, after-body length, shear layer separation and reattachment, reduced velocity, and lock-in [15, 16]. Den Hartog's and

Parkinson's one degree-of-freedom (1-DOF) models of galloping are, however, too simple to describe galloping events for systems with multiple degrees of freedom. In fact, Den Hartog's criterion needs an ice profile generating a region of negative lift derivative in the normal orientation of the conductor. Such negative lift derivative regions do not occur in the presence of glaze ice shapes which are thin, smooth, and crescent-like [8]. Thus, while in the case of wet snow accretion, the Den Hartog model demonstrates good physical agreement [1, 8], it fails to predict galloping in the case of glaze ice, except for the particular case of reverse wind in which the wind direction changes dramatically [1].

Nigol and Buchan [17] showed other cases in which the Den Hartog mechanism cannot explain galloping. They also showed that dynamic instabilities of iced conductors cannot be predicted using the quasi-steady response assumption. More studies by Nigol et al. [18, 19] on the coupled vertical-torsional oscillation mechanism showed that the torsional freedom plays an important role in the vertical oscillations. In other words, the coupling between vertical and torsional displacements is a fundamental factor in the galloping of conductors [1]. This finding explained a possible mechanism of instabilities in the absence of the Den Hartog's criterion where the derivative of lift is positive [1, 2, 8]. Other 2-DOF studies with similar approaches were conducted by Desai et al. [20] and Blevins [3]. Desai [20] concluded that the behavior of a bluff body is very sensitive to structural parameters, and the response can be periodic, quasi-periodic, or even chaotic. They also emphasized that torsion (twist) can either "aggravate" or "alleviate" the galloping, when coupled with translational motion.

Yu et al. [21, 22] developed an analytical formulation for 3-DOF galloping (vertical, horizontal, and torsional) with eccentric inertia coupling, and studied a transmission line problem to assess a galloping instability criterion and predict the potential for flashover during the design process. However, their structural model has been oversimplified as they used only one three-node element for the entire conductor. Later, in 1995 [23], the same researchers extended their static model for cable-supported structures and developed a finite element model for galloping of multi-span single conductors. In that work, large-amplitude vibrations of iced, multi-span line conductor sections are studied using three-node isoparametric cable elements having three translational and one torsional degrees-of-freedom at each node. The effect of remote conductors and supports (insulator strings) are also considered in their model. In this study, the time integration of the equations of motion is performed in the sub-space using the principal coordinates. The sub-space method requires solving the eigenvalue problem and computing eigenvectors, and is well suited for systems with time-invariant coefficient matrices (mass, damping, and stiffness). Hence, the geometric nonlinearities inherent to large kinematics galloping cables are ignored in this approach in order to reduce the computational time. Despite this deficiency, this model made a significant improvement in the structural model of the galloping of transmission line conductors. Wang and Lou [24] used the same formulation on a single conductor span and applied Newton-Raphson stiffness updating with direct time integration to consider the geometric nonlinearities. Moreover, they considered wind turbulence effects reported in the literature, see for example [1, 8, 25].

Along with the numerical studies, various experiments are reported in the literature that explore different aspects of galloping events (see e.g. [1, 8, 26, 27] and the references cited therein). However, these works will not be covered here as the focus is on computational approaches.

Although structural models have extensively improved through time, in the case of conductor galloping, the fluid force modeling methods have not advanced much. While coupled numerical fluid-structure interaction (FSI) is widely used to study vortex-induced vibrations (VIV) and low-amplitude oscillations of circular cylinders and prisms (see e.g. [28-32]), in most numerical studies of galloping, the fluid loading on the structure is assumed quasi-steady. This is because of the complexity of the flows over bluff bodies that vary with profile shape, Reynolds number, incoming flow turbulence intensity, and the structural response, such as displacement and frequency of oscillations.

To qualify for the quasi-steady assumption, the frequency of oscillations has to be sufficiently low with respect to the loading frequency. Under these conditions, the aerodynamic load on a predefined 2D profile is assumed to be identical to that of the stationary profile at the equivalent incidence angle (the angle of attack of the profile in the relative frame of reference). This assumption ignores the instantaneous loading and gives only a time-averaged loading. As the flow behind a bluff body and consequent loading are inherently unsteady, the quasi-steady assumption cannot provide a good representation in all cases. Measurements of vertical and rotational forced motions, within the amplitude and frequency range of the galloping, show that the quasi-steady computations generally agree with

unsteady measurements of the lift coefficient; however, the unsteady moment coefficient and the moment obtained with the quasi-steady method can differ significantly [4, 8]. Moreover, the literature shows that the angular velocity does not affect the unsteady lift, while the unsteady moment changes considerably [1]. Therefore, if the aerodynamic moment is important in simulations, which is essential to study conductor galloping, the difference between quasi-steady and unsteady calculations can be considerable. In addition, even if the quasi-steady assumption is valid, it will be limited to single conductors. In other words, as the incidence angle and magnitude of the velocity reaching the leeward conductor are a function of the vortex shedding and relative displacements of the conductors, computing the exact incident angle for leeward conductors is impossible. Finally, it is shown that the transverse motion of bluff bodies causes the mean drag to increase [33], making the drag coefficient a function of the amplitude of vibrations. This effect is assumed small in a quasi-steady analysis.

1.5 Approaches to Study Galloping

As many other fields of science and physics, there are three major approaches to study galloping: theoretical, experimental and numerical. Theoretical methods are limited to simple one- or two-dimensional cases. This method studies the galloping mainly from a structural point of view, i.e. fluid loads are considered predefined. Den Hartog analysis (1932) made the first analytical attempt to study the galloping of iced conductors and its important variables and mechanisms [3]. He described the galloping from a strictly aerodynamic point of view. Parkinson (1971) was first to explain the galloping by means of separated flow from bluff

bodies (see [8, 15]). All theoretical methods are limited to explaining the basic behavior of the galloping, rather than providing applied tools for its study and control.

In experimental methods, there are three main issues to perform the simulation: scale of model (full or down-scaled), simulating natural conditions, and accreted ice profile and its material (i.e. using real or artificial ice to simulate actual profile). In experiments, both full and scaled models are used; however, because of the large aspect ratio of conductors, constructing a scaled model seems to be inappropriate and the results are difficult to trust. Conducting a full-scale test is, on the other hand, very expensive, but what makes it questionable is simulating natural conditions. There is no control on natural conditions at test sites; therefore, results are limited to the specific test condition of the site, making it difficult to predict galloping under different conditions. Modeling the ice profile is another issue. Natural ice profile and artificial ice (made of other materials) are two methods to model the actual ice. Using natural ice is difficult; therefore, most experiments are conducted with artificial profiles constructed using materials such as aluminum or wood which do not have the properties of real ice. More importantly, models applied in experiments are usually constant along the span and do not vary with time. However, it is known that unsteady and non-uniform ice accretion could be important parameters in galloping. When all model set-ups are done, a camera set-up is required for mode analysis and recording the behavior of the model for future post-processing. The mentioned concerns make

experimental methods not only expensive, but also limited to specific conditions of the test site.

Therefore, numerical methods for predicting and preventing galloping through unsteady flow calculation become of great interest. Numerical aeroelastic analysis is a more elaborate method that dispenses with the quasi-steady assumption, and makes it possible to capture a time-accurate response of the structure under varying conditions. In addition, it can model different natural conditions and ice profiles that are non-uniform along the span. All these factors contribute to the added credibility and realism of a numerical aeroelastic approach.

1.6 Objectives and Research Methodology

The objective of this research is to develop a high-fidelity multidisciplinary analysis (MDA) of vibrations of iced overhead electrical conductors. The project couples a Computational Fluid Dynamics (CFD) code with a Computational Structural Dynamics (CSD) code, to produce a high-fidelity aeroelastic simulation system for galloping of transmission line conductors.

The simulation is conducted by developing and assembling the following three-module system. The first module consists of the FENSAP-ICE [34] flow solver for the simulation of the fluid flow. The second module is a fluid-structure preprocessor that exchanges information between the CFD and CSD codes and controls the fluid-structure interaction (FSI). The third module consists of the CSD solver. After developing the frameworks, each framework is tested in 2D for

debugging, verification, and validation purposes, and then the 3D representation is completed and demonstrated.

1.7 Outline of Thesis

The thesis is organized into four main chapters. The current introductory chapter begins with reviewing flow-induced instabilities, making a literature review, defining the state of the current work in the field, and outlining the research methodology and the philosophy behind it. In chapter 2, the governing equations of the flow, the equations of motions of structure, derivation of these equations, numerical solution of the governing equations, the coupling algorithm, and the details of the aeroelastic methodology are explained. Chapter 3 covers numerical results, validations, and discussions. Finally, chapter 4 contains concluding remarks, contribution, and recommendations for future work.

CHAPTER 2: Computational Aeroelastic Modeling

In this chapter, the aeroelastic methodology implemented to study galloping problems is presented. The governing equations for both fluid and structural fields are described with detail and coupling between these two domains and data transfer between them are depicted. Moreover, the numerical methods to solve the governing equations are presented. In addition, different versions of the methodology are explained. The flow equations are solved using FENSAP-ICE, a second order time accurate, 3D finite element compressible Navier-Stokes solver [34-36] which is an in-house flow solver developed by Newmerical Technologies International. The transmission line conductors are modeled by employing the finite element method and the resultant equations of motions are integrated via a second order time accurate Newmark-beta method. A conservative data transfer module is designed for load and displacement exchange between flow and structure solvers.

2.1 Flow Governing Equations

The flow governing equations are the compressible Unsteady Reynolds-Averaged Navier-Stokes (URANS) equations and the continuity equation. These equations, along with the energy equation, form a complete set of equations for a flow field with significant energy transfer in the system. The Arbitrary Lagrangian Eulerian (ALE) formulation [37] of the governing equations is applied to compute the time-accurate solution of the flow field with moving meshes.

The Reynolds-Averaged, ALE formulation of the governing flow equations for a single phase, Newtonian fluid with no external work, in the Cartesian framework, can be expressed as follows.

$$\frac{d\rho}{dt} - \frac{dx_i}{dt}\rho_{,i} + \left(\rho U_i\right)_{,i} = 0 \tag{2.1}$$

$$\frac{d\rho U_i}{dt} - \frac{dx_i}{dt}\left(\rho U_i\right)_{,i} + \left(\rho U_i U_j\right)_{,j} = -p_{,i} + \left(\tau_{ij} - \rho\overline{u_i u_j}\right)_{,j} \tag{2.2}$$

$$\begin{aligned}\frac{d\rho h_0}{dt} - \frac{dx_j}{dt}\left(\rho h_0\right)_{,j} - \left(\frac{dp}{dt} - \frac{dx_j}{dt}p_{,j}\right) + \left(\rho U_j h_0\right)_{,j} = \\ \left(\lambda T_{,j} - \rho\overline{u_j h}\right)_{,j} + \left[U_i\left(\tau_{ij} - \rho\overline{u_i u_j}\right)\right]_{,j}\end{aligned} \tag{2.3}$$

where,

$$\tau_{ij} = \mu\left(U_{i,j} + U_{j,i}\right) - \frac{2}{3}\mu\delta_{ij}U_{k,k} \tag{2.4}$$

$$h_0 = h + K + k \tag{2.5}$$

$$h = C_p T, \quad K = \frac{1}{2}U_i U_i, \quad k = \frac{1}{2}\overline{u_i u_i} \tag{2.6}$$

In these equations, ρ is air density; t, time; U_i, the i^{th} component of the time averaged velocity; u_i, the i^{th} component of the time varying velocity; dx_i/dt, the i^{th} component of the mesh velocity; p, the time averaged pressure; T, the time averaged temperature; τ_{ij}, the stress tensor; $-\overline{u_i u_j}$ is the Reynolds stress tensor,

$-\overline{u_j h}$, the turbulent flux or Reynolds heat flux, k, the turbulent kinetic energy, K, the time averaged kinetic energy, h, the time averaged enthalpy, h_0, the time averaged total enthalpy, λ, the thermal conductivity, μ, the dynamic viscosity, and C_p is the specific heat capacity at constant pressure. Equation (2.1) stands for the continuity or conservation of mass, Eq. (2.2) represents the Navier-Stokes equations, and, finally, Eq. (2.3) shows the total energy equation.

2.1.1 Closure Problems

Examining the number of equations and unknowns presented in §2.1 discloses two types of closure problems requiring extra equations in order to close the system of equations. The equation of state provides one of these extra equations. For ideal gases in the thermodynamic equilibrium, the equation of state in non-dimensional form can be stated as below (see Eq. (2.12) for non-dimensional variables).

$$p = \frac{\rho T}{\gamma_\infty M_\infty^2} \tag{2.7}$$

This equation closes the time averaged system; however, the turbulent terms, including the Reynolds stress tensor, turbulent heat flux, and turbulent kinetic energy terms need to be determined for solving the entire system of equations. This is called the turbulence closure problem.

Various turbulence models from less complex correlation-based turbulent-viscosity models (such as algebraic, one-equation, two-equation), and Reynolds

stress models, to more complex higher order models (such as Large Eddy Simulation (LES), Detached Eddy Simulation (DES), and their variants), are available to solve this closure problem (see e.g. [38]). Although each turbulence model is designed for certain flow regimes, in general, the accuracy of the model increases with the order of the turbulence model and the model coding becomes more complicated. At the same time, the computational cost and CPU time increase tremendously due to the additional variables introduced and the highly refined grids required by higher order models. Since computational cost and a reasonable size of the computational grid are important factors in unsteady applications, a turbulent-viscosity model is chosen; being practical and accurate enough.

Based on the Bousinessq approximation, the transport of momentum by turbulence is a diffusive process and is similar to that of the molecular viscosity. Hence, the Reynolds stress can be related to the mean strain rate tensor. The Reynolds heat flux is also approximated by a similar analogy with heat transfer. Therefore,

$$-\overline{u_i u_j} = 2\nu_t S_{ij} - \frac{2}{3} k \delta_{ij} \tag{2.8}$$

$$-\overline{u_j h} = -\frac{\lambda_t}{\rho} T_{,j} \tag{2.9}$$

where subscript t holds for the turbulent variables and,

$$S_{ij} = \frac{1}{2}\left(U_{i,j} + U_{j,i}\right) \tag{2.10}$$

$$\frac{\lambda_t}{\rho} = \frac{\nu_t C_p}{\mathrm{Pr}_t} \tag{2.11}$$

The local mean rate of the strain, S_{ij}, is calculated using the mean flow velocities, and the eddy (or turbulent) viscosity, $\nu_t = \mu_t / \rho$, and the turbulent kinetic energy, k, are estimated from the turbulent-viscosity model. The parameter Pr_t is the turbulent Prandtl number. Experiments have shown that this number varies a little throughout the flow field [39], thus Pr_t can be taken constant and equal to that of the free-stream. By applying this assumption, the equation set is closed.

The Spalart-Allmaras (S-A) model [40] is chosen to model the eddy viscosity. This model is a computationally stable and numerically efficient method while practically accurate to estimate the eddy viscosity. In the S-A model, the turbulent viscosity is only a function of the modified eddy viscosity, $\tilde{\nu}$, requiring one PDE equation to be solved. Other advantage of the S-A model is that it does not require a very refined mesh close to the body. Full derivation of the S-A model, the governing equation, and functionality of the turbulent viscosity can be found in turbulence books, see e.g. [39-41].

2.1.2 Non-dimensional Form of the Governing Equations

The non-dimensional form of the governing equations is found by applying the following set of dimensionless variables.

$$\begin{aligned} x_i' &= \frac{x_i}{l_\infty},\ U_i' = \frac{U_i}{U_\infty},\ \rho' = \frac{\rho}{\rho_\infty},\ T' = \frac{T}{T_\infty}, \\ C_p' &= \frac{C_p}{C_{p_\infty}},\ \mu' = \frac{\mu}{\mu_\infty},\ \lambda' = \frac{\lambda}{\lambda_\infty}, \\ t' &= \frac{tU_\infty}{l_\infty},\ p' = \frac{p}{\rho_\infty U_\infty^2},\ h' = \frac{h}{C_{p_\infty} T_\infty} \end{aligned} \tag{2.12}$$

where l is the characteristic length and subscript ∞ represents the reference condition (i.e. the free-stream).

By replacing these variables in the governing equations and using Equations (2.8) and (2.9), the non-dimensional form of the governing equations is found (note that primes are omitted for simplicity).

$$\frac{\partial \rho U_i}{\partial t} - \frac{dx_i}{dt}\left(\rho U_i\right)_{,i} + \left(\rho U_i U_j\right)_{,j} = -\tilde{p}_{,i} + \mathrm{Re}_\infty^{-1}\left(\sigma_{ij}\right)_{,j} \tag{2.13}$$

$$\begin{aligned} &\frac{d\rho h}{dt} - \frac{dx_j}{dt}\left(\rho h\right)_{,j} + \left(\rho U_j h\right)_{,j} = \\ &\left(\gamma_\infty - 1\right) M_\infty^2 \left(\frac{dp}{dt} - \frac{dx_j}{dt} p_{,j} + U_j \tilde{p}_{,j} \right) + \\ &\left(\gamma_\infty - 1\right) M_\infty^2 \,\mathrm{Re}_\infty^{-1} U_{i,j}\sigma_{ij} + \mathrm{Re}_\infty^{-1}\left(\left(\lambda \,\mathrm{Pr}_\infty^{-1} + \lambda_t \,\mathrm{Pr}_{t\infty}^{-1}\right) T_{,j}\right)_{,j} \end{aligned} \tag{2.14}$$

$$\sigma_{ij} = 2\left(\mu + \mu_t\right)\left(S_{ij} - \frac{1}{3} S_{kk}\delta_{ij} \right) \tag{2.15}$$

$$\tilde{p} = p + \frac{2}{3}\rho k \delta_{ij} \tag{2.16}$$

where Re_∞ is the free-stream Reynolds number; γ_∞, the free-stream specific heat ratio; M_∞, the free-stream Mach number; and Pr_∞ stands for the free-stream Prandtl number.

It should be noted that, as the non-dimensional form of the continuity equation is identical to its dimensional form, this equation is not repeated here. Equations (2.13) represent the non-dimensionalized momentum equations, and Eq. (2.14) stands for the thermal energy equation. In order to derive this equation from that of the total energy, i.e. Eq. (2.3), the dot product of the continuity equations and the velocity vector is subtracted from the total energy equation. Finally, it also should be noted that the turbulent kinetic energy, k, is often ignored in the definition of the total enthalpy [39]. Hence, in the energy equation, this value is omitted.

2.1.3 ALE Formulation and Moving Fluid Mesh

The governing equations presented in the previous sections are in the ALE form. It means that the formulation is capable of handling the moving grids which are required for the aeroelastic approach. In order to consider the grid motion in the ALE formulation, the time derivative of any variable f, such as density, pressure, enthalpy, etc., in the original Eulerian equations has been replaced by the following ALE time derivative [37, 42].

$$\frac{\partial f}{\partial t} = \frac{df}{dt} - \frac{dx_i}{dt} f_{,i} \tag{2.17}$$

where the time derivative $\frac{d}{dt}$ is taken along the trajectory of the grid node moving at speed $\frac{d\mathbf{x}}{dt}$. A grid speed of zero recovers the pure Eulerian description, and one equal to the flow velocity recovers the pure Lagrangian formulation.

In the ALE formulation, the moving boundary conditions are modified to include the grid velocity, i.e. the non-slip boundary condition on the wall will be $U_i = dx_i / dt$.

In order to move the boundary in the flow field, it is required to adjust and move the entire computational grid in such a way that 1) at all times the grid stays valid without returning a negative volume; 2) it follows the boundary move smoothly; and 3) keeps an acceptable quality of the original grid. By moving the grid, the grid nodal velocity at each fluid mesh node is computed. There are several grid movement strategies such as algebraic mapping, smoothing operator, unsteady mesh adaptation, or global re-meshing [42]. Moving grid by a smoothing operator has benefits over the other methods that make it optimal for general purposes. This method is practically efficient; there is no need for CPU-time intensive operations to interpolate the solution that are required in the global re-meshing and unsteady mesh adaptation methods. Moreover, there is no accuracy concern due to the interpolation of the flow solution. Besides, despite the algebraic mapping, the smoothing strategy is able to handle complex geometries

and unknown motions, making the method suitable for fluid-structure interaction applications.

In the smoothing technique, the nodal displacement of the internal nodes of the grid is found by solving a smoothing operator. The smoothing operator is Laplace's equation, $\nabla^2(\Delta x_i) = 0$, which for each component of the displacement vector forms an elliptic system of equations to be solved at each time step. This boundary-value problem is solved by employing appropriate boundary conditions. Displacements at wet surfaces (the moving structures) are imposed as non-zero Dirichlet boundary conditions, and a zero displacement is applied for non-moving surfaces and other type of boundaries such as far-field, inlet, and exit.

2.1.4 Numerical Discretization of Flow Governing Equations

The flow governing equations in FENSAP-ICE are discretized using a finite element method. The weak-Galerkin form of the equations is found as the equations are multiplied first by weight functions equal to the interpolation shape functions, and then integrated over the volume. There are also several considerations such as stabilization and pressure decoupling issues which are addressed inside the software. As FENSAP-ICE was fully developed at the time of this research, the numerical discretization details are not presented here. All details regarding the discretization, stability, artificial dissipation, numerical solution, and etc. can be found in the FENSAP-ICE publications [42-45]. There have been also several modifications in FENSAP-ICE in order to make it possible to communicate with the current aeroelastic code.

2.2 Equations of Motion

The equations of motion (EOM) are derived by applying the Hamilton principle [46, 47] as stated in the following equation.

$$\int_{t_1}^{t_2} \left(\delta \mathscr{U} - \delta \mathscr{T} - \delta \mathscr{W} \right) dt = 0 \tag{2.18}$$

where δ stands for the variation operator. The strain energy, $\mathscr{U}$, the kinetic energy, $\mathscr{T}$, and the work done by all conservative and non-conservative loads, $\mathscr{W}$, are defined as below [47].

$$\delta \mathscr{U} = + \int_{\mathscr{V}} \{\delta \varepsilon\}^T \{\sigma\} \, d\mathscr{V} \tag{2.19}$$

$$\begin{aligned} \delta \mathscr{T} &= + \int_{\mathscr{V}} \{\delta \dot{u}\}^T \, \rho \{\ddot{u}\} \, d\mathscr{V} \\ &= - \int_{\mathscr{V}} \{\delta u\}^T \, \rho \{\ddot{u}\} \, d\mathscr{V} \end{aligned} \tag{2.20}$$

$$\delta \mathscr{W} = + \int_{\mathscr{V}} \{\delta u\}^T \{F\} \, d\mathscr{V} + \text{other non-conserv. work} \tag{2.21}$$

In these equations, the concentrated masses and loads are not included. The $\{\varepsilon\}$ is the strain tensor; $\{\sigma\}$, the stress tensor; $\{u\}$, the displacement vector of a point in the volume $\mathscr{V}$, measured from the initial static equilibrium; ρ, the mass density; and $\{F\}$ stands for the external dynamic fluid loading vector at a point in the volume $\mathscr{V}$. The dot operator is the differentiation with respect to time, t. In the following sub-sections, all components of the Hamilton's principle are

evaluated over the finite element representation of the transmission line conductors, and the finite element form of the EOM is represented.

2.2.1 Finite Element Representation

In Figure 2-1, schematic drawing of the 3D finite element model of a multi-span transmission line with a bundled iced conductors is shown, and in Figure 2-2, a typical cross section of an iced conductor in local coordinates, $\mathbf{x} = (x, y, z)$, is illustrated. The displacement in the local coordinates is defined as $\mathbf{u} = \{u\} = (u, v, w)$. In Figure 2-3, the global coordinates, $\mathbf{X}(S) = (X, Y, Z)$, and the global displacements, $\mathbf{q}(S) = (U, V, W, \theta)^T$ are defined, and a three-node parabolic cable element used to discretize the conductors is shown in the initial and deformed shapes.

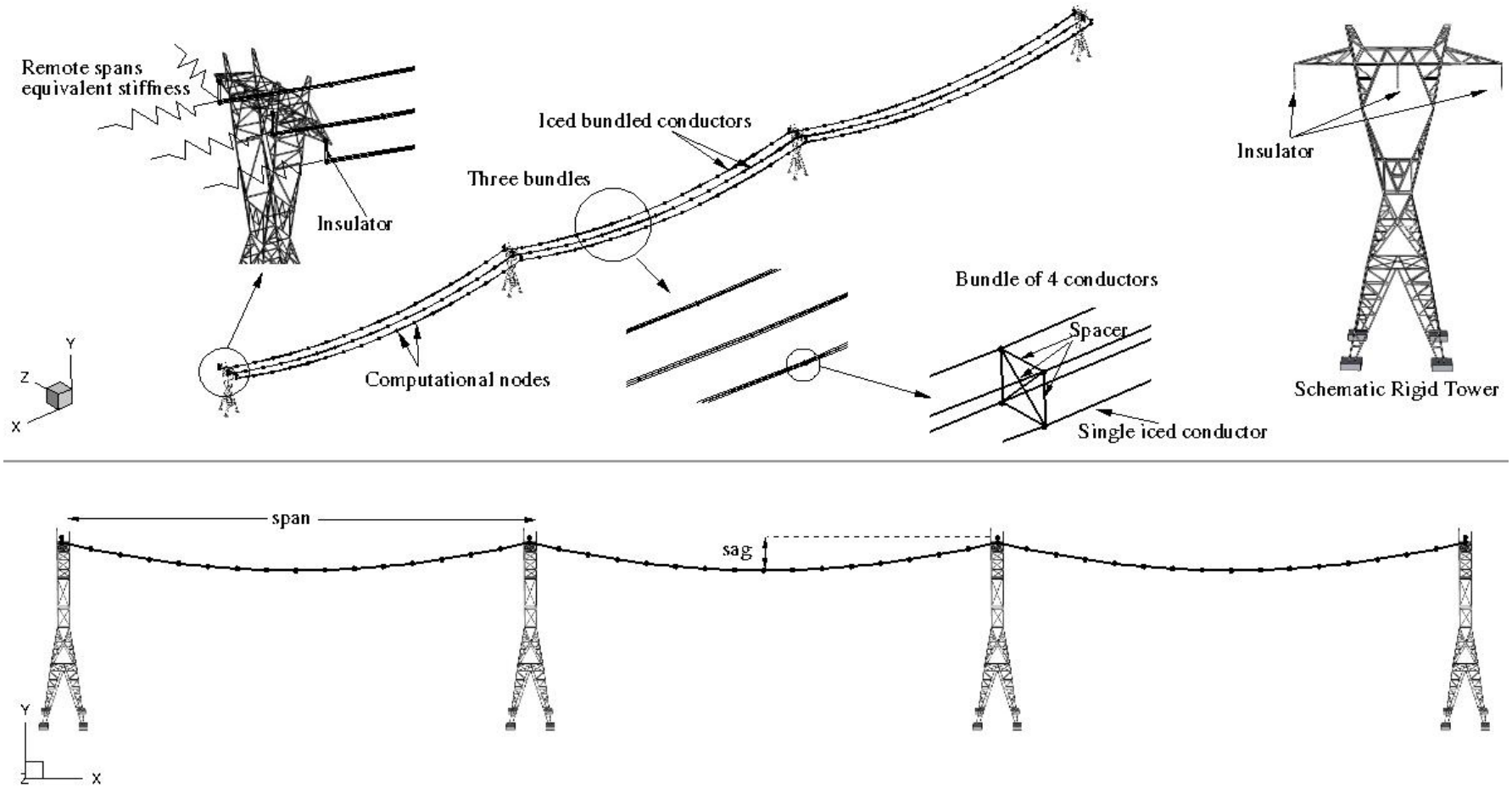

Figure 2-1: Schematic drawing representing 3D model of a multi-span transmission line with bundled iced conductors

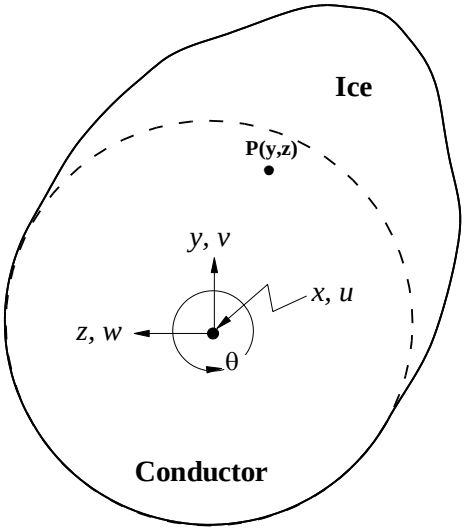

Figure 2-2: Typical cross section of an iced conductor in local coordinate

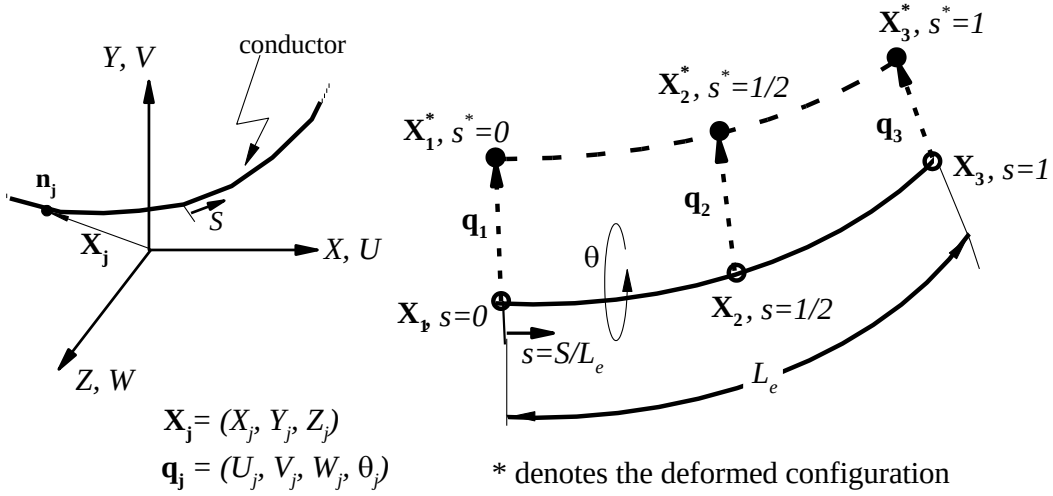

Figure 2-3: Three-node parabolic cable element in initial and deformed forms, in local and global coordinates

By following the isoparametric form of the finite element model, the same shape functions are used to interpolate all variables including the displacement, velocity, acceleration, and etc. Hence (index *e* stands for element),

$$\begin{aligned}
&\mathbf{X} = \left[\tilde{N}\right]\mathbf{X}_e;\ \dot{\mathbf{X}} = \left[\tilde{N}\right]\dot{\mathbf{X}}_e;\ \ddot{\mathbf{X}} = \left[\tilde{N}\right]\ddot{\mathbf{X}}_e \\
&\mathbf{x} = \left[\tilde{N}\right]\mathbf{x}_e;\quad \dot{\mathbf{x}} = \left[\tilde{N}\right]\dot{\mathbf{x}}_e;\quad \ddot{\mathbf{x}} = \left[\tilde{N}\right]\ddot{\mathbf{x}}_e \\
&\boldsymbol{\theta} = \left[\underset{\sim}{N}\right]\boldsymbol{\theta}_e;\quad \dot{\boldsymbol{\theta}} = \left[\underset{\sim}{N}\right]\dot{\boldsymbol{\theta}}_e;\quad \ddot{\boldsymbol{\theta}} = \left[\underset{\sim}{N}\right]\ddot{\boldsymbol{\theta}}_e \\
&\mathbf{q} = \left[N\right]\mathbf{q}_e;\quad \dot{\mathbf{q}} = \left[N\right]\dot{\mathbf{q}}_e;\quad \ddot{\mathbf{q}} = \left[N\right]\ddot{\mathbf{q}}_e
\end{aligned} \tag{2.22}$$

$$\begin{aligned}
&\mathbf{X}_e = \{X_e\} = (\mathbf{X}_1, \mathbf{X}_2, \mathbf{X}_3)^T;\quad \mathbf{X}_j = \{X_j\} = (X_j, Y_j, Z_j) \\
&\mathbf{x}_e = \{x_e\} = (\mathbf{x}_1, \mathbf{x}_2, \mathbf{x}_3)^T;\quad \mathbf{x}_j = \{x_j\} = (x_j, y_j, z_j) \\
&\mathbf{q}_e = \{q_e\} = (\mathbf{q}_1, \mathbf{q}_2, \mathbf{q}_3)^T;\quad \mathbf{q}_j = \{q_j\} = (U_j, V_j, W_j, \theta_j) \\
&\boldsymbol{\theta}_e = \{\theta_e\} = (\theta_1, \theta_2, \theta_3)^T;\quad j = 1,2,3
\end{aligned} \tag{2.23}$$

The shape functions are defined in terms of the natural coordinate, S, and the element length, L_e, (Figure 2-3).

$$[N] = \left[N_1[I_4]\ N_2[I_4]\ N_3[I_4]\right] \tag{2.24}$$

$$\left[\tilde{N}\right] = \left[N_1[I_3]\ N_2[I_3]\ N_3[I_3]\right] \tag{2.25}$$

$$\left[\underset{\sim}{N}\right] = \left[N_1\ N_2\ N_3\right] \tag{2.26}$$

$$[N_1] = s(2s-3)+1;\ [N_2] = -4s(s-1);\ [N_3] = s(2s-1) \tag{2.27}$$

$$s \equiv S/L_e;\ [I_n] \equiv n \times n \text{ identity matrix} \tag{2.28}$$

2.2.2 Kinetic Energy Variation

Consider an arbitrary point at cross section of the iced conductor, i.e. point P in Figure 2-2, which moves in the local coordinate $\mathbf{x}$. Variation of the kinetic energy density of the point P, $\delta\mathcal{T}^P$ can be written as,

$$\delta\mathcal{T}^P = -\delta\mathbf{u}^T \rho \ddot{\mathbf{u}} \tag{2.29}$$

In order to evaluate the kinetic energy variation in the global coordinate system, it is required to define the local to global transformation matrix. The transformation matrix, $[R]$, maps the global displacements to the local and takes the form of Eq. (2.30). By examining the definition of the global and local coordinate systems in Figure 2-2 and Figure 2-3, the matrix can be represented as Eq. (2.31) for small torsions (θ).

$$\mathbf{u} = [R]\mathbf{q} = [R][N]\mathbf{q}_e \tag{2.30}$$

$$[R] = \begin{bmatrix} 1 & 0 & 0 & 0 \\ 0 & 1 & 0 & -z \\ 0 & 0 & 1 & y \end{bmatrix} \tag{2.31}$$

Hence,

$$\delta\mathcal{T}^P = -\delta\mathbf{q}^T [R]^T \rho [R]\ddot{\mathbf{q}} \tag{2.32}$$

The variation of the kinetic energy for an element, $\delta\mathcal{T}_e$, can be expressed as (note that $A_c = A_c(S)$ is the total area of the cross section of the iced conductor),

$$\begin{aligned}\delta\mathscr{T}_e &= -\int_{\mathscr{V}_e} \delta\mathscr{T}^P \, d\mathscr{V} = -\int_0^{L_e}\int_{A_c} \delta\mathbf{q}^T [R]^T \rho [R]\ddot{\mathbf{q}} dA_c \, dS \\ &= -\int_0^{L_e}\int_{A_c} \delta\mathbf{q}_e^T [N]^T [R]^T \rho [R][N]\ddot{\mathbf{q}}_e dA_c \, dS \\ &= -\delta\mathbf{q}_e^T \left[\int_0^{L_e} [N]^T \left(\int_{A_c} \rho [R]^T [R] dA_c\right)[N] dS\right]\ddot{\mathbf{q}}_e\end{aligned} \tag{2.33}$$

By defining the mass density matrix, $[\mu]$, and the element mass matrix, $[M_e]$,

$$[\mu] = \int_{A_c} \rho [R]^T [R] dA_c \tag{2.34}$$

$$[M_e] = \int_0^{L_e} [N]^T [\mu][N] dS \tag{2.35}$$

Eq. (2.33) takes the following form.

$$\begin{aligned}\delta\mathscr{T}_e &= -\delta\mathbf{q}_e^T \left[\int_0^{L_e} [N]^T [\mu][N] dS\right]\ddot{\mathbf{q}}_e \\ &= -\delta\mathbf{q}_e^T \left[M^e\right]\ddot{\mathbf{q}}_e\end{aligned} \tag{2.36}$$

The elements of the mass density matrix are formed explicitly by substituting $[R]$ from Eq. (2.31) into Eq. (2.34) and performing the integration.

$$[\mu] = \begin{bmatrix} m & 0 & 0 & 0 \\ 0 & m & 0 & -S_y \\ 0 & 0 & m & S_z \\ 0 & -S_y & S_z & I_\theta \end{bmatrix} \tag{2.37}$$

where, m is the total mass density; I_θ, the mass moment of inertia; S_y, the first mass moment of area about axis z; and S_z is the first mass moment of area about

axis y, per unit length of the conductor. These variables are functions of intrinsic coordinate, S, and are approximated using the same shape functions as the displacements.

$$m = \int_{A_c} \rho dA_c \tag{2.38}$$

$$I_\theta = \int_{A_c} \rho\left(y^2 + z^2\right) dA_c \tag{2.39}$$

$$S_y = \int_{A_c} \rho z dA_c \tag{2.40}$$

$$S_z = \int_{A_c} \rho y dA_c \tag{2.41}$$

$$[\mu] = [N][\mu_e] \tag{2.42}$$

$$[\mu_e] = [\mu_1\ \mu_2\ \mu_3]^T\ ;\ [\mu_j] \text{ evaluated at local node } j \tag{2.43}$$

2.2.3 Strain Energy Variation

In this section, the variation of the strain energy in Eq. (2.19) is evaluated for one cable element. The cable element can deform axially along the cable and twist around it, thus the total strain tensor can be written as Eq. (2.44). The ε_S takes the form of Eq. (2.45) in global coordinate [48], and the ε_θ is simply the derivative of θ with respect to S, i.e. Eq. (2.47).

$$\{\varepsilon\} = \begin{Bmatrix} \varepsilon_S \\ \varepsilon_\theta \end{Bmatrix} \tag{2.44}$$

$$\begin{aligned} \varepsilon_S &= \frac{1}{2}\left\{\left(\frac{\partial \mathbf{X}^{*T}}{\partial S}\right)\left(\frac{\partial \mathbf{X}^{*}}{\partial S}\right) - 1\right\} \\ &= \underbrace{\frac{\partial X}{\partial S}\frac{\partial U}{\partial S} + \frac{\partial Y}{\partial S}\frac{\partial V}{\partial S} + \frac{\partial Z}{\partial S}\frac{\partial W}{\partial S}}_{\text{small displacement strain}} + \underbrace{\frac{1}{2}\left[\left(\frac{\partial U}{\partial S}\right)^2 + \left(\frac{\partial V}{\partial S}\right)^2 + \left(\frac{\partial W}{\partial S}\right)^2\right]}_{\text{large displacement strain}} \end{aligned} \tag{2.45}$$

$$\mathbf{X}^{*} = \mathbf{X} + (U, V, W) \tag{2.46}$$

$$\varepsilon_\theta = \frac{\partial \theta}{\partial S} \tag{2.47}$$

Similar to the strain, the stress tensor $\{\sigma\}$ is composed of the axial, σ_S, and torsional, τ_θ, stresses. For linear elastic displacements, the stress-strain relations are expressed by employing Hooke's law and using the modulus of elasticity, E, the area, A, and the torsional rigidity, GJ. Also, the effect of coupling between the torsional and axial displacements [49] is added via axial-torsional coupling parameter, B. In the following equations, matrix $[E]$ is called the elasticity matrix, and $\{\sigma_0\}$ is known as the initial stress vector defined in terms of the initial static tension, T, and the internal moment, M, which the later resists the moment caused by the initial eccentric ice weight.

$$\begin{aligned} \sigma_S &= \frac{EA}{A}\varepsilon_S + \frac{B}{A}\varepsilon_\theta \\ \tau_\theta &= \frac{GJ}{A}\varepsilon_\theta + \frac{B}{A}\varepsilon_S \end{aligned} \tag{2.48}$$

$$\{\sigma\} = \begin{Bmatrix} \sigma_S \\ \tau_\theta \end{Bmatrix} + \{\sigma_0\} = [E]\{\varepsilon\} + \{\sigma_0\} \tag{2.49}$$

$$[E] = \frac{1}{A}\begin{bmatrix} AE & B \\ B & GJ \end{bmatrix} \tag{2.50}$$

$$\{\sigma_0\} = \frac{1}{A}\begin{Bmatrix} T \\ M \end{Bmatrix} \tag{2.51}$$

By substituting Eqs. (2.48)-(2.51) into Eq. (2.19), the variation of the strain energy for an element can be formed.

$$\begin{aligned} \delta \mathscr{U}_e &= \int_{\mathscr{V}} \delta\varepsilon\, \sigma\, d\mathscr{V} = \int_0^{L_e}\int_{A_c} \delta\varepsilon\, \sigma\, dA_c\, dS \\ &= \int_0^{L_e} \delta\varepsilon_S\, AE\, \varepsilon_S dS + \int_0^{L_e} \delta\varepsilon_\theta\, GJ\, \varepsilon_\theta dS \\ &+ \int_0^{L_e} \delta\varepsilon_S B\, \varepsilon_\theta dS + \int_0^{L_e} \delta\varepsilon_S\, B\, \varepsilon_\theta dS \\ &+ \int_0^{L_e} T_0 \delta\varepsilon_S dS + \int_0^{L_e} M_0 \delta\varepsilon_\theta\, dS \\ &= \underbrace{\int_0^{L_e} \{\delta\varepsilon\}^T\, A[E]\{\varepsilon\}\, dS}_{\delta \mathscr{U}_{e_1}} + \underbrace{\int_0^{L_e} \{\delta\varepsilon\}^T\, A\{\sigma_0\}\, dS}_{\delta \mathscr{U}_{e_2}} \end{aligned} \tag{2.52}$$

Through employing a finite element approximation, the integrant of the first integral, $\delta \mathscr{U}_{e_1}$, in Eq. (2.52) takes the following form, (note that $[\,...'] = \frac{\partial}{\partial S}[...]$).

$$\{\delta\varepsilon\}^T A[E]\{\varepsilon\} = \begin{Bmatrix} \delta \mathbf{X}_e^{*T}\left[\tilde{N}'\right]^T\left[\tilde{N}'\right]\mathbf{X}_e^* \\ \delta\theta_e\left[\underset{\sim}{N}'\right]^T \end{Bmatrix} A[E] \begin{Bmatrix} \frac{1}{2}\left[\mathbf{X}_e^{*T}\left[\tilde{N}'\right]^T\left[\tilde{N}'\right]\mathbf{X}_e^* - 1\right] \\ \left[\underset{\sim}{N}'\right]\theta_e \end{Bmatrix} \tag{2.53}$$

Let's define the matrix $[\mathbb{SD}]$ which is called strain-displacement relationship [23], such that,

$$[\mathbb{SD}] = \left[[\mathbb{SD}_1][\mathbb{SD}_2][\mathbb{SD}_3]\right] \tag{2.54}$$

where,

$$\left[\mathbb{SD}_j\right] = N_j' \begin{bmatrix} X^{*'} & Y^{*'} & Z^{*'} & 0 \\ 0 & 0 & 0 & 1 \end{bmatrix} \quad j = 1,2,3 \tag{2.55}$$

By using the strain-displacement relationship matrix and following the standard linearization process for the geometrically non-linear problems (in order to avoid high order terms), Eq. (2.53), equation of deflections from the initial static equilibrium, can be represented as,

$$\{\delta\varepsilon\}^T A[E]\{\varepsilon\} = \delta\mathbf{q}_e^T [\mathbb{SD}]^T A[E]\ [\mathbb{SD}]\ \mathbf{q}_e \tag{2.56}$$

Thus,

$$\begin{aligned} \delta\mathscr{U}_{e_1} &= \int_0^{L_e} \delta\mathbf{q}_e^T [\mathbb{SD}]^T A[E]\ [\mathbb{SD}]\ \mathbf{q}_e dS \\ &= \delta\mathbf{q}_e^T \int_0^{L_e} [\mathbb{SD}]^T A[E]\ [\mathbb{SD}]\ dS\, \mathbf{q}_e \\ &= \delta\mathbf{q}_e^T [K_e]\mathbf{q}_e \end{aligned} \tag{2.57}$$

$$\left[K_e^e\right] = \int_0^{L_e} [\mathbb{S}\mathbb{D}]^T \, A[E] \, [\mathbb{S}\mathbb{D}] \, dS \tag{2.58}$$

where $\left[K_e^e\right]$ is the element elastic stiffness matrix. By substituting $\delta\{\varepsilon\}$ and $\{\sigma_0\}$, and retaining only linear terms, $\delta\mathscr{U}_{e_2}^2$ is evaluated such that,

$$\begin{aligned}
\delta\mathscr{U}_{e_2} &= \int_0^{L_e} \begin{Bmatrix} \delta\mathbf{X}_e^{*T}\left[\tilde{N}'\right]^T\left[\tilde{N}'\right]\mathbf{X}_e^* \\ \delta\theta_e\left[\underset{\sim}{N}'\right]^T \end{Bmatrix}^T \begin{Bmatrix} T \\ M \end{Bmatrix} dS \\
&= \delta\mathbf{q}_e^T \int_0^{L_e} [N']^T [\mathbb{S}][N'] dS \mathbf{q}_e \\
&= \delta\mathbf{q}_e^T \left[K_\sigma^e\right]\mathbf{q}_e
\end{aligned} \tag{2.59}$$

$$\left[K_\sigma^e\right] = \int_0^{L_e} [N']^T [\mathbb{S}][N'] dS \tag{2.60}$$

where $\left[K_\sigma^e\right]$ is known as the element geometric stiffness matrix, and the initial stress matrix, $[\mathbb{S}]$, is defined as,

$$[\mathbb{S}] = \begin{bmatrix} T & 0 & 0 & 0 \\ 0 & T & 0 & 0 \\ 0 & 0 & T & 0 \\ 0 & 0 & 0 & M \end{bmatrix} \tag{2.61}$$

2.2.4 Load Work Variation

In this section, the work done by all conservative and non-conservative loads in Eq. (2.21) is evaluated. There are three types of time-dependent internal and

external loads applied to the iced conductors; the aerodynamic loading, $\mathbf{F}$, the damping load due to friction of the internal elements of structure, $\mathbf{F}_D$, and the eccentric ice weight, $\mathbf{F}_{ice}$, hence one can write $\delta\mathscr{W}_e = \delta\mathscr{W}_{e_F} + \delta\mathscr{W}_{e_D} + \delta\mathscr{W}_{e_{ice}}$. Let $\mathbf{F}$ to be the time varying surface integral of the fluid loading per unit length at S, thus the $\delta\mathscr{W}_{e_F}$ is simply,

$$\begin{aligned} \delta\mathscr{W}_{e_F} &= \delta\mathbf{q}_e^T \int_0^{L_e} \mathbf{F} dS \\ &= \delta\mathbf{q}_e^T \int_0^{L_e} [N]\mathbf{F}_e dS \end{aligned} \tag{2.62}$$

where,

$$\begin{aligned} &\mathbf{F}_e = [\mathbf{F}_1\mathbf{F}_2\mathbf{F}_3]^T \\ &\mathbf{F}_j = \left(F_{x_j}, F_{y_j}, F_{z_j}, M_{\theta_j}\right);\ j = 1,2,3 \end{aligned} \tag{2.63}$$

The eccentric ice weight plays as a restoring moment, W_{ice}. For small sag to span ratios, the cross section of the conductor can be considered normal to the span vector (X-axis). Hence, for small twists around the initial static position, the W_{ice} can be expressed as,

$$W_{ice} = -gS_z \sin\theta \approx -gS_z\theta \tag{2.64}$$

where g is the gravity constant. Therefore, the contribution of the ice weight work can be written as,

$$\begin{aligned}\delta \mathscr{W}_{e_{ice}} &= -\delta\theta \int_0^{L_e} -gS_z \theta dS \\ &= -\delta \mathbf{\theta}_e \int_0^{L_e} \left[\underset{\sim}{N}\right]^T g \left[\underset{\sim}{N}\right] \mathbf{\theta}_e dS\end{aligned} \tag{2.65}$$

This equation can be re-casted in terms of $[N]$ and $\mathbf{q}_e$ such that,

$$\begin{aligned}\delta \mathscr{W}_{e_{ice}} &= -\delta \mathbf{q}_e^T \int_0^{L_e} [N]^T [P] g [N] dS \, \mathbf{q}_e \\ &= \delta \mathbf{q}_e^T \left[K_{ice}^e\right] \mathbf{q}_e\end{aligned} \tag{2.66}$$

where,

$$P_{ij} = \begin{cases} S_z & i = j = 4 \\ 0 & \text{else} \end{cases} \quad i, j = 1,2,3,4 \tag{2.67}$$

$$\left[K_{ice}^e\right] = -g \int_0^{L_e} [N]^T [P][N] dS \tag{2.68}$$

The last part of the work is that done by damping. Modeling of damping is very difficult, and the experimental data is very limited and incomplete to construct the work done by damping for all frequencies involved in the system. Therefore, approximate models are developed to include the damping of the known frequencies. Usually, the work done by damping takes the following form,

$$\delta \mathscr{W}_{e_D} = \delta \mathbf{q}_e^T \left[C^e\right] \dot{\mathbf{q}}_e \tag{2.69}$$

where, $\left[C^e\right]$ is called the element structural damping matrix. The model to construct the elements of this matrix will be explored later in §2.2.6.

2.2.5 Discretized Form of EOM

Let's substitute the expressions found for $\delta\mathscr{U}_e$, $\delta\mathscr{T}_e$, and $\delta\mathscr{W}_e$ into Eq. (2.18) and expand it. Hence,

$$\int_{t_1}^{t_2}\sum_e\left(\delta\mathscr{U}_e-\delta\mathscr{T}_e-\delta\mathscr{W}_e\right)dt=0 \tag{2.70}$$

$$\int_{t_1}^{t_2}\sum_e\delta\mathbf{q}_e^T\left(\left[M^e\right]\ddot{\mathbf{q}}_e+\left[C^e\right]\dot{\mathbf{q}}_e+\left[K_T^e\right]\mathbf{q}_e+\int_0^{L_e}[N]\mathbf{F}_e dS\right)dt=0 \tag{2.71}$$

$$\left[K_T^e\right]=\left[K_e^e\right]+\left[K_\sigma^e\right]+\left[K_{ice}^e\right] \tag{2.72}$$

$$\int_{t_1}^{t_2}\delta\mathbf{q}^T\left([M]\ddot{\mathbf{q}}+[C]\dot{\mathbf{q}}+[K_T]\mathbf{q}-\mathbf{F}\right)dt=0 \tag{2.73}$$

$$[M]=\sum_e\left[M^e\right];\ [C]=\sum_e\left[C^e\right];\ [K_T]=\sum_e\left[K_T^e\right] \tag{2.74}$$

where, $[M]$ is the mass/inertia matrix; $[C]$, the structural viscous damping matrix; $\left[K_T\right]$, the tangent stiffness matrix ($\left[K_T\right]=\left[K_e\right]+\left[K_\sigma\right]+\left[K_{ice}\right]$); and $\mathbf{F}$ the global nodal load vector. These global matrices are formed by performing a standard finite element assembly procedure [36], and calculation of the nodal load vector is presented in §2.3.

The $\delta\mathbf{q}^T$ is the variation of an arbitrary vector $\mathbf{q}$ which can take any value; therefore, in order to impose the equality in Eq. (2.73) for all conditions, the expression inside the parenthesis should be zero, i.e.

$$[M]\ddot{\mathbf{q}}+[C]\dot{\mathbf{q}}+[K_T]\mathbf{q}=\mathbf{F}(t) \tag{2.75}$$

This equation is known as the finite element discretized form of the equations of motion, and is employed for dynamic analysis of most systems. However, forming the mass, stiffness, and damping matrices for different elements used in the finite element analysis is required.

2.2.6 Structural Damping

Damping plays an important role in the dynamic analysis of systems. Two types are involved in the current system, the aerodynamic and structural dampings. The aerodynamic damping is the property of the fluid-structure system imposed by their interaction, and is naturally included through the unsteady loading in the fluid-structure interaction analysis. The structural damping is, however, an inherent property of the structure itself, which dissipates the internal energy of the structure through the work done by friction between different components of the system. The structural damping is very small for large displacements of the conductors and can be ignored for cases with loadings that occur for a short period of time such as impact; however, due to numerical stability requirements, this cannot be ignored for problems with time-dependent loading.

The mechanism of structural damping is complicated, making the modeling and quantification difficult, particularly for systems with a large number of degrees of freedom. Among several models introduced to approximate the effect of damping, Rayleigh damping is widely used for its simplicity and possibility of

decoupling the equations of motions [46]. The Rayleigh damping takes the following form.

$$[C] = \alpha[M] + \beta[K_T] \tag{2.76}$$

where α and β are constant coefficients known as the mass and stiffness damping coefficients, respectively. The following equation relates these coefficients by employing the natural frequency of the system, ω, and the relevant critical damping ratio, ζ.

$$2\zeta\omega = \alpha + \beta\omega^2 \tag{2.77}$$

$$\zeta = \frac{\alpha}{2\omega} + \frac{\beta\omega}{2} \tag{2.78}$$

Examining Eq. (2.78) shows that at low frequencies, the α coefficient dominates and, at high frequencies, the β coefficient controls the damping ratio. This demonstrates that the α coefficient targets the low frequency (rigid body) motions and β damps the high frequency motions. In order to find the damping coefficients, only two equations are needed. This means that with Rayleigh damping, we can control only two natural frequencies with given damping ratios. Hence,

$$\begin{aligned} \beta &= 2\frac{\zeta_1\omega_1 - \zeta_2\omega_2}{\omega_1^2 - \omega_2^2} \\ \alpha &= 2\omega_1\omega_2\frac{\zeta_2\omega_1 - \zeta_1\omega_2}{\omega_1^2 - \omega_2^2} \end{aligned} \tag{2.79}$$

By using Rayleigh damping, the target frequencies, ω_1 and ω_2, are damped with damping ratios of ζ_1 and ζ_2, respectively, and the damping ratio for other frequencies is imposed by Eq. (2.78). It should be noted that Rayleigh damping, if not used correctly, may impose under- or over-damping. For an accurate studying of instabilities, including galloping, preventing over-damping is very important. Therefore, in the presence of the aerodynamic damping, the damping ratio for linear displacements is kept very small in order to just prevent numerical instabilities and damp the high frequency non-physical responses. On the other hand, for the twist (torsion) degree-of-freedom, the damping ratio is very high due to very high friction between the strands of the conductors. Hence, the damping ratio for this degree-of-freedom needs to be much larger than that of the linear displacements. Hence, the damping matrix is constructed as follows.

$$\begin{aligned} c_{ij} &= \alpha_d M_{ij} + \beta_d K_{T_{ij}} \qquad \text{for } i \text{ which corresponds to } U,V,W \text{ DOF} \\ c_{ij} &= \alpha_\theta M_{ij} + \beta_\theta K_{T_{ij}} \qquad \text{for } i \text{ which corresponds to } \theta \text{ DOF} \end{aligned} \tag{2.80}$$

where α_d & β_d are the coefficients for the linear displacements, and α_θ & β_θ are those of the torsional displacement.

2.2.7 Remote Spans, Insulators, and Boundary Conditions

Remote spans are modeled with linear static springs, K_{ST}, in the horizontal direction, see Figure 2-1. This stiffness is associated to the horizontal displacement and is assembled accordingly into the diagonal entry of the $[K_T]$

during the finite element assembly procedure. Following the model presented by Veletsos and Darbre [50], the effective stiffness of the remote spans is computed.

$$\frac{1}{K_{ST}} = \frac{1}{K_e} + \frac{1}{K_i} \tag{2.81}$$

$$\begin{aligned} K_e &= \frac{AE}{L_c}\cos^2\Theta \\ K_i &= 12\frac{H_h^3}{q_v L_h^3}\cos^2\Theta \end{aligned} \tag{2.82}$$

where, L_c and L_h are the total length of the cable and the horizontal span between the adjacent towers; H_h, the horizontal component of the tension; q_v, the total vertical load intensity; and Θ is the angle between the line connecting two adjacent towers and the horizon (this is considered zero for remote spans).

The effect of support insulators are modeled by two linear springs, K_{Ix} and K_{Iz}, acting at the horizontal plane along X- and Z- axes, respectively [23]. These springs are added to the relative diagonals of the $[K_T]$ during the finite element assembly procedure.

$$K_{Ix} = \frac{1}{L_I}\left(p_v L_e + \frac{W_I}{2}\right) \tag{2.83}$$

$$K_{Iz} = K_{Ix} + \frac{2H_0}{L_x} \tag{2.84}$$

where L_I and W_I are the length and weight of the insulator, accordingly.

Two types of Dirichlet boundary conditions at the points where the conductors are attached to the towers are implemented; dead-end and simple support. Dead-end boundary condition sets all the degrees of freedom to zero, $\mathbf{q} = 0$, while simple support fixes only the vertical and torsional degrees of freedom, $V = 0; \theta = 0$. These Dirichlet boundary conditions are applied via a standard Payne-Irons method.

2.2.8 Incremental Form of Equations of Motion

Due to a geometric nonlinearity, it is preferred to solve the incremental form of the EOM. The equation of motion (2.75) is valid at time t and $t + \Delta t$, where Δt is the time step. Let's first define the $\mathbf{F}_I$, $\mathbf{F}_D$, and $\mathbf{F}_E$ such that,

$$ {}^{t}\mathbf{F}_I = {}^{t}[M]\,{}^{t}\ddot{\mathbf{q}} \tag{2.85} $$

$$ {}^{t}\mathbf{F}_D = {}^{t}[C]\;{}^{t}\dot{\mathbf{q}} \tag{2.86} $$

$$ {}^{t}\mathbf{F}_E = {}^{t}[K_T]\,{}^{t}\mathbf{q} \tag{2.87} $$

where the left superscript means evaluation at time t. Thus, the instantaneous equilibrium of the EOM at t and $t + \Delta t$ can be written as,

$$ {}^{t+\Delta t}\mathbf{F}_I + {}^{t+\Delta t}\mathbf{F}_D + {}^{t+\Delta t}\mathbf{F}_E = {}^{t+\Delta t}\mathbf{F} \tag{2.88} $$

$$ {}^{t}\mathbf{F}_I + {}^{t}\mathbf{F}_D + {}^{t}\mathbf{F}_E = {}^{t}\mathbf{F} \tag{2.89} $$

Subtracting the latest equations and defining $\Delta\mathbf{F}_{...} = {}^{t+\Delta t}\mathbf{F}_{...} - {}^{t}\mathbf{F}_{...}$, leads to the incremental form of the equations of motion in terms of the forces.

$$\Delta\mathbf{F}_I + \Delta\mathbf{F}_D + \Delta\mathbf{F}_E = \Delta\mathbf{F} \tag{2.90}$$

The mass matrix is a weak function of the displacement and consequently time; however, the stiffness and damping matrices change with displacement (geometric non-linearity). We assume that the stiffness and damping are functions of displacement and velocity increments accordingly. Thus, the inertia, damping, and elastic force increments are,

$$\Delta\mathbf{F}_I = \left[M \right]\Delta\mathbf{q} \tag{2.91}$$

$$\Delta\mathbf{F}_D = \left[\hat{C} \right]\Delta\dot{\mathbf{q}} \tag{2.92}$$

$$\Delta\mathbf{F}_E = \left[\hat{K}_T \right]\Delta\mathbf{q} \tag{2.93}$$

where the incremental displacement, velocity, and acceleration are,

$$\Delta\mathbf{q} = {}^{t+\Delta t}\mathbf{q} - {}^{t}\mathbf{q} \tag{2.94}$$

$$\Delta\dot{\mathbf{q}} = {}^{t+\Delta t}\dot{\mathbf{q}} - {}^{t}\dot{\mathbf{q}} \tag{2.95}$$

$$\Delta\ddot{\mathbf{q}} = {}^{t+\Delta t}\ddot{\mathbf{q}} - {}^{t}\ddot{\mathbf{q}} \tag{2.96}$$

Then, the incremental form of the equations of motion can be introduced in the following form.

$$\left[M \right]\Delta\ddot{\mathbf{q}} + \left[\hat{C} \right]\Delta\dot{\mathbf{q}} + \left[\hat{K}_T \right]\Delta\mathbf{q} = \Delta\mathbf{F} \tag{2.97}$$

In order to avoid iterations per time step, the tangent (rather than secant) stiffness and damping are employed. This means that the damping and stiffness matrices are evaluated based on initial values at time t. This assumption requires small time steps. Hence, the damping and stiffness matrices take the following form.

$$\left[\hat{C} \right] = \left. \frac{\partial \mathbf{F}_D}{\partial \dot{\mathbf{q}}} \right|_t = \left[C \right] \tag{2.98}$$

$$\left[\hat{K}_T \right] = \left. \frac{\partial \mathbf{F}_S}{\partial \mathbf{q}} \right|_t = \left[K_T \right] \tag{2.99}$$

2.2.9 Numerical Step-by-Step Integration of EOM

The equations of motion are solved in full-space by a direct implicit step-by-step integration using the second order time accurate and unconditionally stable Newmark-Beta operator (trapezoidal rule) [46, 51]. The step-by-step integration provides the possibility to include the geometrical non-linearity. In addition, the Newmark-Beta method introduces no amplitude decay which makes it superior to other integration methods. However, this method suffers from period elongation [46] which can be healed by controlling the time step (see §2.4).

In Newmark-Beta method, the acceleration is considered to vary linearly from time t to $t + \Delta t$, and the following relations are employed.

$$\Delta\dot{\mathbf{q}} = {}^{t}\ddot{\mathbf{q}}\Delta t + \tilde{\delta}\,\Delta\ddot{\mathbf{q}}\Delta t \tag{2.100}$$

$$\Delta\mathbf{q} = {}^{t}\dot{\mathbf{q}}\Delta t + \frac{1}{2}{}^{t}\ddot{\mathbf{q}}\Delta t^2 + \tilde{\beta}\,\Delta\ddot{\mathbf{q}}\Delta t^2 \tag{2.101}$$

where parameters $\tilde{\beta}$ and $\tilde{\delta}$ can be determined in such a way that the required stability and accuracy conditions are met. By finding the acceleration increment from Eq. (2.100) and then substituting it into Eq. (2.101), two equations are found for $\Delta\dot{\mathbf{q}}$ and $\Delta\ddot{\mathbf{q}}$ in terms of $\Delta\mathbf{q}$ and known values at time t. That is,

$$\Delta\ddot{\mathbf{q}} = \frac{1}{\tilde{\beta}\Delta t^2}\Delta\mathbf{q} - \frac{1}{\tilde{\beta}\Delta t}{}^{t}\dot{\mathbf{q}} - \frac{1}{2\tilde{\beta}}{}^{t}\ddot{\mathbf{q}} \tag{2.102}$$

$$\Delta\dot{\mathbf{q}} = \frac{\tilde{\delta}}{\tilde{\beta}\Delta t}\Delta\mathbf{q} - \frac{\tilde{\delta}}{\tilde{\beta}}{}^{t}\dot{\mathbf{q}} + \Delta t\left(1 - \frac{\tilde{\delta}}{2\tilde{\beta}}\right){}^{t}\ddot{\mathbf{q}} \tag{2.103}$$

Substituting Eqs. (2.102) and (2.103) into Eq. (2.97) forms the modified incremental EOM,

$$\left[\tilde{K}\right]\Delta\mathbf{q} = \Delta\tilde{\mathbf{F}} \tag{2.104}$$

where $\left[\tilde{K}\right]$ stands for the effective incremental stiffness matrix, and $\Delta\tilde{\mathbf{F}}$ is the effective incremental force vector defined in the following.

$$\Delta\tilde{\mathbf{F}} = \Delta\mathbf{F} + [M]\left(\frac{1}{\tilde{\beta}\Delta t}{}^{t}\dot{\mathbf{q}} + \frac{1}{2\tilde{\beta}}{}^{t}\ddot{\mathbf{q}}\right) + \left[\tilde{C}\right]\left(\frac{\tilde{\delta}}{\tilde{\beta}}{}^{t}\dot{\mathbf{q}} - \Delta t\left(1 - \frac{\tilde{\delta}}{2\tilde{\beta}}\right){}^{t}\ddot{\mathbf{q}}\right) \tag{2.105}$$

$$\left[\tilde{K}\right]=\left[\hat{K}_T\right]+\frac{\tilde{\delta}}{\tilde{\beta}\Delta t}\left[\hat{C}\right]+\frac{1}{\tilde{\beta}\Delta t^2}[M] \tag{2.106}$$

Newmark-Beta method induces more than needed damping for values of $\tilde{\delta}$ other than $\frac{1}{2}$ [52], hence this parameter is kept fixed at $\frac{1}{2}$. For other parameter, $\tilde{\beta}$, Newmark proposed the range of $\frac{1}{6}\le\tilde{\beta}\le\frac{1}{2}$. Examining equations for $\tilde{\beta}=\frac{1}{6}$ shows that the method become the linear acceleration scheme which is only conditionally stable [46]. Hence, the original value suggested by Newmark, $\frac{1}{4}$, which is unconditionally stable is chosen. This choice enforces that the velocity vector, $\dot{\mathbf{q}}$, varies linearly and that the average acceleration vector, $\bar{\ddot{\mathbf{q}}}$, be fixed in the time interval Δt. This method is known as the constant-average-acceleration method of Newmark-Beta.

Finally, it should be noted that the non-incremental form of the EOM can be integrated in the same manner. In this case, the following equations should be solved. Here, only the main relations are outlined.

$$\left[\tilde{K}\right]^{t+\Delta t}\mathbf{q}={}^{t+\Delta t}\tilde{\mathbf{F}} \tag{2.107}$$

$$\begin{aligned}{}^{t+\Delta t}\tilde{\mathbf{F}}={}^{t+\Delta t}\mathbf{F}+[M]&\left(\frac{1}{\tilde{\beta}\Delta t^2}{}^{t}\mathbf{q}+\frac{1}{\tilde{\beta}\Delta t}{}^{t}\dot{\mathbf{q}}-\left(1-\frac{1}{2\tilde{\beta}}\right){}^{t}\ddot{\mathbf{q}}\right)\\&+\left[\hat{C}\right]\left(\frac{\tilde{\delta}}{\tilde{\beta}\Delta t}{}^{t}\mathbf{q}-\left(1-\frac{\tilde{\delta}}{\tilde{\beta}}\right){}^{t}\dot{\mathbf{q}}-\Delta t\left(1-\frac{\tilde{\delta}}{2\tilde{\beta}}\right){}^{t}\ddot{\mathbf{q}}\right)\end{aligned} \tag{2.108}$$

$$ {}^{t+\Delta t}\ddot{\mathbf{q}} = \frac{1}{\tilde{\beta}\Delta t^2}\left({}^{t+\Delta t}\mathbf{q} - {}^{t}\mathbf{q}\right) - \frac{1}{\tilde{\beta}\Delta t}\,{}^{t}\dot{\mathbf{q}} + \left(1 - \frac{1}{2\tilde{\beta}}\right){}^{t}\ddot{\mathbf{q}} \tag{2.109} $$

$$ \begin{aligned} {}^{t+\Delta t}\dot{\mathbf{q}} &= \frac{\tilde{\delta}}{\tilde{\beta}\Delta t}\left({}^{t+\Delta t}\mathbf{q} - {}^{t}\mathbf{q}\right) + \left(1 - \frac{\tilde{\delta}}{\tilde{\beta}}\right){}^{t}\dot{\mathbf{q}} + \Delta t\left(1 - \frac{\tilde{\delta}}{2\tilde{\beta}}\right){}^{t}\ddot{\mathbf{q}} \\ &= {}^{t}\dot{\mathbf{q}} + \left[\left(1-\tilde{\delta}\right){}^{t}\ddot{\mathbf{q}} + \tilde{\beta}\,{}^{t+\Delta t}\ddot{\mathbf{q}}\right]\Delta t \end{aligned} \tag{2.110} $$

2.3 Coupling Algorithm and Conveying Data

There are two coupling methods widely used in the literature: tightly coupled (aka direct or two-way coupling), and loosely coupled (aka iterative or one-way coupling).

In tightly coupled approaches, the governing equations of both fluid and solid are combined and solved in a combined computational domain, on a single grid. This approach offers great robustness when solving difficult FSI problems, for example, large deformations with "soft" structures [53]. However, tightly coupled approaches often suffer from the ill-conditioning of the associated matrices [54]. Moreover, two-way coupled schemes are incapable of using existing fluid and solid solvers.

In the loosely coupled approaches, many, if not most, of the disadvantages of tightly coupled methods are avoided [54]. The fluid and solid equations are successively and separately solved with independent solvers, using different grids if needed. Each part (i.e. structure or flow solver) calls the latest information provided by the other part of the coupled system. This approach takes advantage of evolving flow and structure solvers, requires less memory than tightly-coupled

approaches, and is applicable to large problems [53, 54]. Although having these benefits, there are two other issues in loose coupling approach to consider: iterative concerns of 1) stability, convergence, and accuracy [55] and 2) data transfer (loads and motion) via non-matching meshes at the surfaces.

Considering the pros and cons of both approaches, a two-way loosely coupled approach is applied, and the flow and structure equations are successively and separately solved with independent solvers using non-matching grids. Then, the latest information provided by each part of the coupled system is called by the other part in order to proceed in time. The stability, convergence, and accuracy issues are handled by taking small time steps and acquiring higher order of accuracy from flow and structure solvers. The general three-dimensional coupling algorithm includes three modules (Figure 2-4): the flow solver, the structural dynamic solver, and the load/motion transfer operator that relays the relevant analysis parameters between the two solution domains.

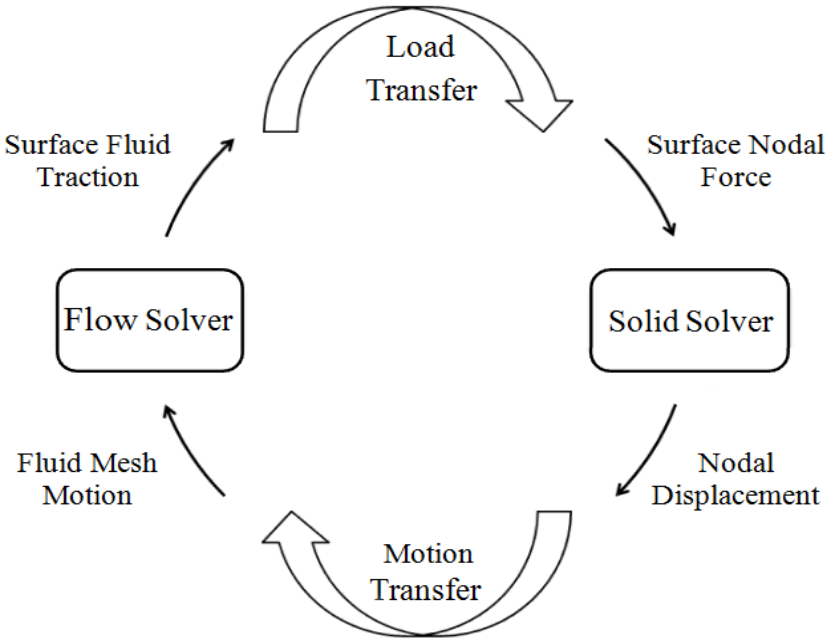

Figure 2-4: FSI simulation loop

The conservative load/motion transfer operator imposes the compatibility of the velocities and the equilibrium of the tractions along the fluid/structure interface (Γ) [54, 56], i.e.,

$$\mathbf{t}_s = \mathbf{t}_f \tag{2.111}$$

$$\frac{\partial \mathbf{u}_f}{\partial t} = \frac{\partial \mathbf{u}_s}{\partial t} \quad \text{or} \quad \mathbf{u}_f = \mathbf{u}_s \tag{2.112}$$

where $\mathbf{t}$ is the traction tensor, $\mathbf{u}$, the displacement, and the subscripts f and s represent the fluid and structure respectively. The tractions for the fluid and structure can be expressed as,

$$\mathbf{t}_f = -p\mathbf{n}_f + \boldsymbol{\sigma}_f \cdot \mathbf{n}_f \quad \text{on} \quad \Gamma_f \tag{2.113}$$

$$\mathbf{t}_s = \boldsymbol{\sigma}_s \cdot \mathbf{n}_s \quad \text{on} \quad \Gamma_s \tag{2.114}$$

where $\mathbf{n}$ is the normal unit vector at Γ. By employing the finite element approximation for tractions, Eq. (2.111) can be presented as,

$$\sum_{i=1}^{n_s} N_s^i \mathbf{t}_s^i = \sum_{j=1}^{n_f} N_f^j \mathbf{t}_f^j \qquad \text{at any point on } \Gamma \tag{2.115}$$

where n is the number of nodes, $\mathbf{t}^i$, the approximate traction at node i, and N stands for the shape function.

In the load transfer, the fluid tractions and the shape functions are given and the loads on the nodes of the structure are required. Hence, in order to impose Eq. (2.115) and find the concentrated structure load vector at the i^{th} node of the structure grid, $\mathbf{F}_s^i = \left(F_{x_i}, F_{y_i}, F_{z_i}\right)$, a node-projection based method (see Figure 2-5) is employed [54, 57].

$$\mathbf{F}_s^i = \int_\Gamma N_s^i \left(\sum_{j=1}^{n_f} N_f^j \mathbf{t}_f^j \right) d\Gamma = \sum_{j=1}^{n_f} \int_\Gamma N_s^i N_f^j d\Gamma \mathbf{t}_f^j \tag{2.116}$$

As the fluid surface load needs to be transferred in the space over a curved line (center of cable), a torsional moment, $M_{\theta s}^i$, around the center of the torsion (see Figure 2-2) will be generated due to the displacement of the load vector. Hence,

$$M_{\theta s}^i = \left(\sum_{j=1}^{n_f} \mathbf{r} \times \int_\Gamma N_s^i N_f^j d\Gamma \mathbf{t}_f^j \right) \cdot \vec{\imath} \tag{2.117}$$

where $\vec{i}$ is the unit vector along the x-axis in the local coordinate system (Figure 2-2), and $\mathbf{r}$ is the position vector of the fluid load on the domain Γ_f measured from origin of the local coordinate. Finally, the global load vector, $\mathbf{F}$, can be written as,

$$\mathbf{F} = \left(\mathrm{F}^1 \, \mathrm{F}^2 \ldots \mathrm{F}^{n_s} \right)^T ; \quad \mathbf{F}^i = \left(\mathbf{F}_s^i \;\; M_{\theta s}^i \right) \; i = 1, 2, ..., n_s \tag{2.118}$$

In a similar fashion, the compatibility condition for displacement (motion transfer) is imposed (see Figure 2-6).

$$\sum_{i=1}^{n_f} N_f^i \mathbf{u}_f^i = \sum_{j=1}^{n_s} N_s^j \mathbf{t}_s^j \qquad \text{at any point on } \Gamma \tag{2.119}$$

In the displacement transfer procedure, the nodal displacements of the structure and associated shape functions are given and the displacements at the fluid surface nodes are required. Hence,

$$\mathbf{u}_f^i = \int_\Gamma N_f^i \left(\sum_{j=1}^{n_f} N_s^j \mathbf{u}_s^j \right) d\Gamma = \sum_{j=1}^{n_f} \int_\Gamma N_f^i N_s^j d\Gamma \mathbf{u}_s^j \tag{2.120}$$

The vector $\frac{\partial \mathbf{u}_f}{\partial t}$ is indeed the surface nodal velocity used by mesh movement scheme as a boundary condition in order to compute the fluid mesh velocity, $\frac{\partial \mathbf{x}}{dt}$, used in ALE formulation of the flow governing equations.

Finally, it should be stressed that data at each time step is transmitted by employing sockets via an IP address and network for a fast data transfer between different modules. This method is much faster than transferring the data through I/O files, especially when the number of communications is high.

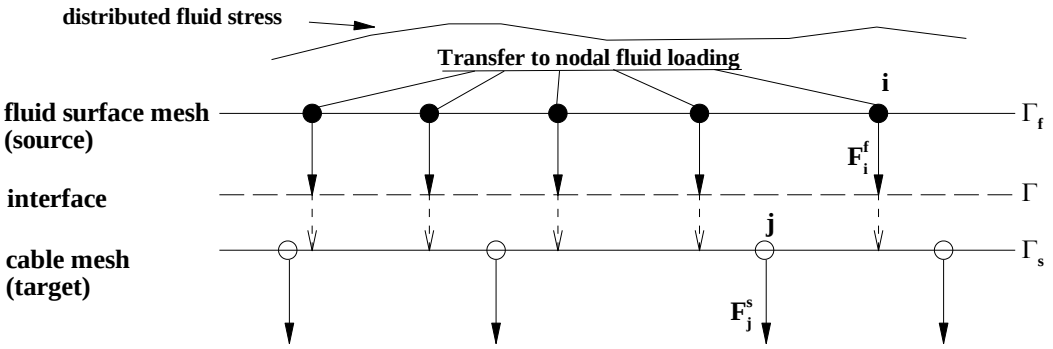

Figure 2-5: Node-projection based load transfer

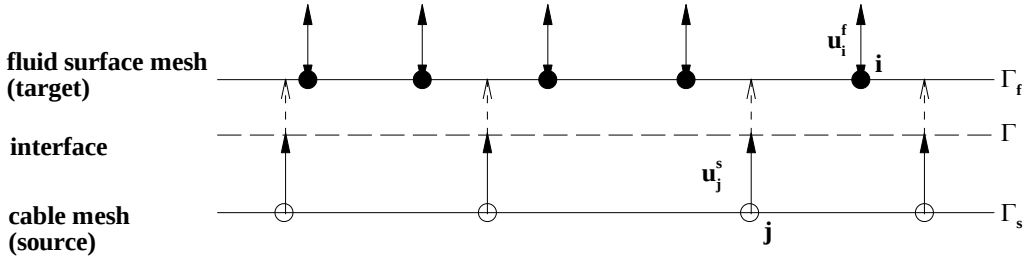

Figure 2-6: Node-projection based motion transfer

2.4 Q3D and 2D Versions

The 3D aeroelastic analysis is also customized for two specific cases: two dimensional (2D) and Quasi-3D (Q3D) analysis. In the case of 2D computations, the bluff body under the study is considered infinitely long by applying appropriate flow and structural boundary conditions. In the flow part, as FENSAP works with 3D meshes only, 2D meshes are extruded from one layer and the periodic boundary condition is applied on the extruded faces. For the structure,

only one node is considered at the center of the rotation of the body and the linear stiffness values are imposed. In this case, there is no need for boundary conditions, and the EOM are simplified to 3 DOF (two displacements in the plane and one rotation).

The second version of the code, Q3D, is designed to prevail over the difficulties associated with 3D calculations of the unsteady flow over slender objects with low fundamental frequencies. The 3D calculations of the unsteady flow field over a transmission line with a typical span of hundreds of meters and a conductor diameter of only a few centimeters requires a huge fluid mesh in order to meet all mesh quality requirements in the boundary layer, wake, and upstream, for an accurate flow calculation. This imposes onerous computations at each time step. Moreover, as the frequency of the oscillations is very low (large period), the physical time required to be simulated in order to reach a limit cycle and/or a large un-damped instability is very long. At the same time, the fluid loading frequency (closely related to the shedding frequency) is very high requiring small time steps. These conditions make the 3D aeroelastic analysis of the multi-span transmission lines very CPU time intensive and impractical at this time.

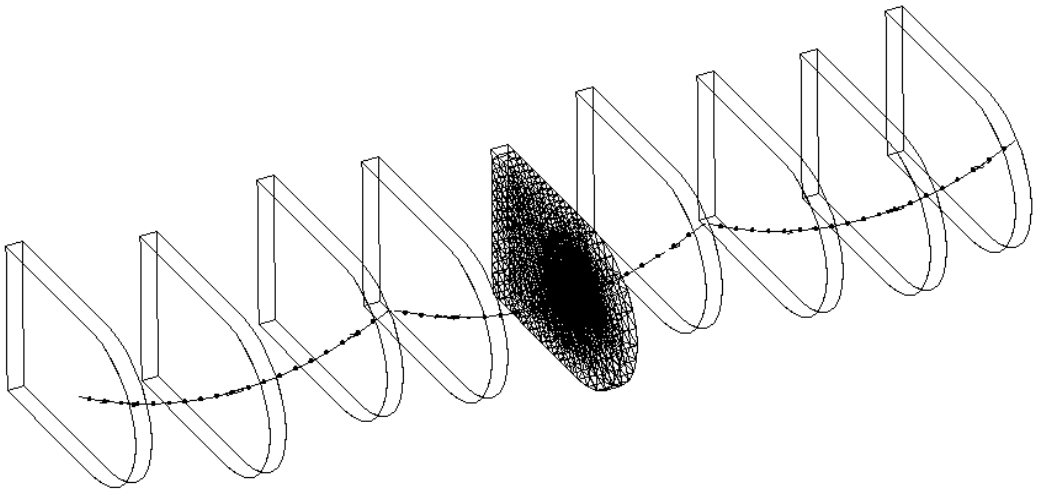

Figure 2-7: Schematic presentation of the Q3D method

In typical transmission lines, the sag to span ratio is very small (of the order of 3%) and the lines are slender bodies due to the small diameter to span ratio (of the order of 0.01%). On the basis of these assumptions, the fluid loading and nodal displacement along the conductor are ignored. Hence, in the Q3D calculations, the 3D flow field around the conductor is reconstructed by solving the flow field over the separate 2D extruded meshes associated to the different cross sections of the line, see Figure 2-7. This requires a multiple separate CFD calculations and a large number of data exchange between CFD and CSD solvers at each time step; therefore, the load/motion transfer module is implemented by employing sockets for a fast and efficient communication. The fluid loading computed by each CFD calculation is integrated and transferred to the finite element model of the structure for the rest of the calculations. In return, the displacement of the fluid surface nodes at each section is computed and transferred to the CFD solver.

2.5 Methodology and Control Parameters

The methodology designed for the aeroelastic analysis and the placements of different components is shown in Figure 2-8. The solution process starts with an initial flow field solution that provides the surface fluid tractions along the fluid/structure mesh interface. Then, using the conservative load transfer operator, the surface tractions are integrated to yield the resultant nodal forces applied on the solid mesh. The solution of the equations of motion provides the displacement, velocity and acceleration at every time step. After each time increment, the structural displacement is imposed via the compatibility condition to the surface nodes of the fluid mesh along the fluid/structure interface. Then, the flow solver uses this interface motion in the formulation to compute the fluid mesh motion in the entire domain, and then solves the flow field. This loop proceeds in time until the total analysis duration is achieved.

As a starting point for the computations, the initial flow solution around the body is required; however, at the first time step, there is no converged CFD solution available. Due to the inherent unsteadiness of the flow around bluff bodies, one common approach in the literature for fluid-structure interaction analysis, to circumvent these implicit initial conditions, is to let the flow around the body establish completely until the shedding vortices reach the unsteady limit cycle. From that point forth, the body starts to move freely. However, in this study, initialization has been done differently. First, enough time iterations (few hundred time steps) are performed in order to get a time-accurate flow established around the body without necessarily reaching the unsteady limit cycle, and then

the conductors are freed to move. Since the source of the vortex shedding behind the bluff body is the flow instabilities, this method helps to reach the limit cycle sooner than the first approach and models the physical problem more accurately. Therefore, as soon as an accurate flow field develops in the field at time t_0, the conductors are released to move from rest. i.e.,

$$^{t_0}\mathbf{q} = ^{t_0}\dot{\mathbf{q}} = \{0\} \tag{2.121}$$

Selection of an appropriate time step is important in time accurate solutions, and it is required to be computed based on the lowest physical time scale present in the problem. The shedding frequency of the oscillating body (f_c) and the dominant natural frequency of the structure (f_n) are two important frequencies governing the time scales. At the beginning of the computations, f_c is unknown; however, generally the frequency ratio of the oscillations ($f^* = f_c / f_n$) is limited by either the shedding frequency ratio of the fixed body (f_s / f_n), or the lock-in frequency ratio. The lock-in frequency ratio is generally less than 1.5 for low mass ratios[1] and around unity for high mass ratios [30], and the shedding frequency ratio is estimated from that of a smooth circular cylinder. The shedding frequency of a circular cylinder is computed from an estimated Strouhal number (St) at each Reynolds number (see e.g. [58] for Re-St functionality). Thus, the time step is computed by dividing one complete shedding or fundamental period, whichever is smaller, by a reasonably large number, between 50 and 500, which

[1] mass ratio is mass of the body to the displaced fluid

provides a suitable response resolution on one hand, and, on the other hand, justifies the constant load assumption and use of the tangent damping and stiffness matrices at each time step. Usually, in the Newmark-Beta method, the numerical integrations of the EOM are accurate with no period elongation if $f_n \Delta t$ is smaller than 0.01 [46]. As the frequency of fluid loading is much higher than the dominant natural frequency of the structure in the case of transmission lines, this criterion is satisfied via the proposed technique. Usually, this time step satisfies the stability criterion of the ALE formulation as well. In summary, relations (2.122) are used to compute the time step.

$$\begin{aligned} &\Delta t = \frac{T}{\mathrm{N}}, \qquad T = \min\left(\frac{1}{f_s}, \frac{1}{f_n}\right), \qquad 50 \le \mathrm{N} \le 500 \\ &f_s = \mathrm{St}\frac{u_\infty}{D}, \qquad \mathrm{St} = \mathrm{St}\left(\frac{1}{\sqrt{\mathrm{Re}}}\right) \qquad D: \text{ conductor diameter} \end{aligned} \tag{2.122}$$

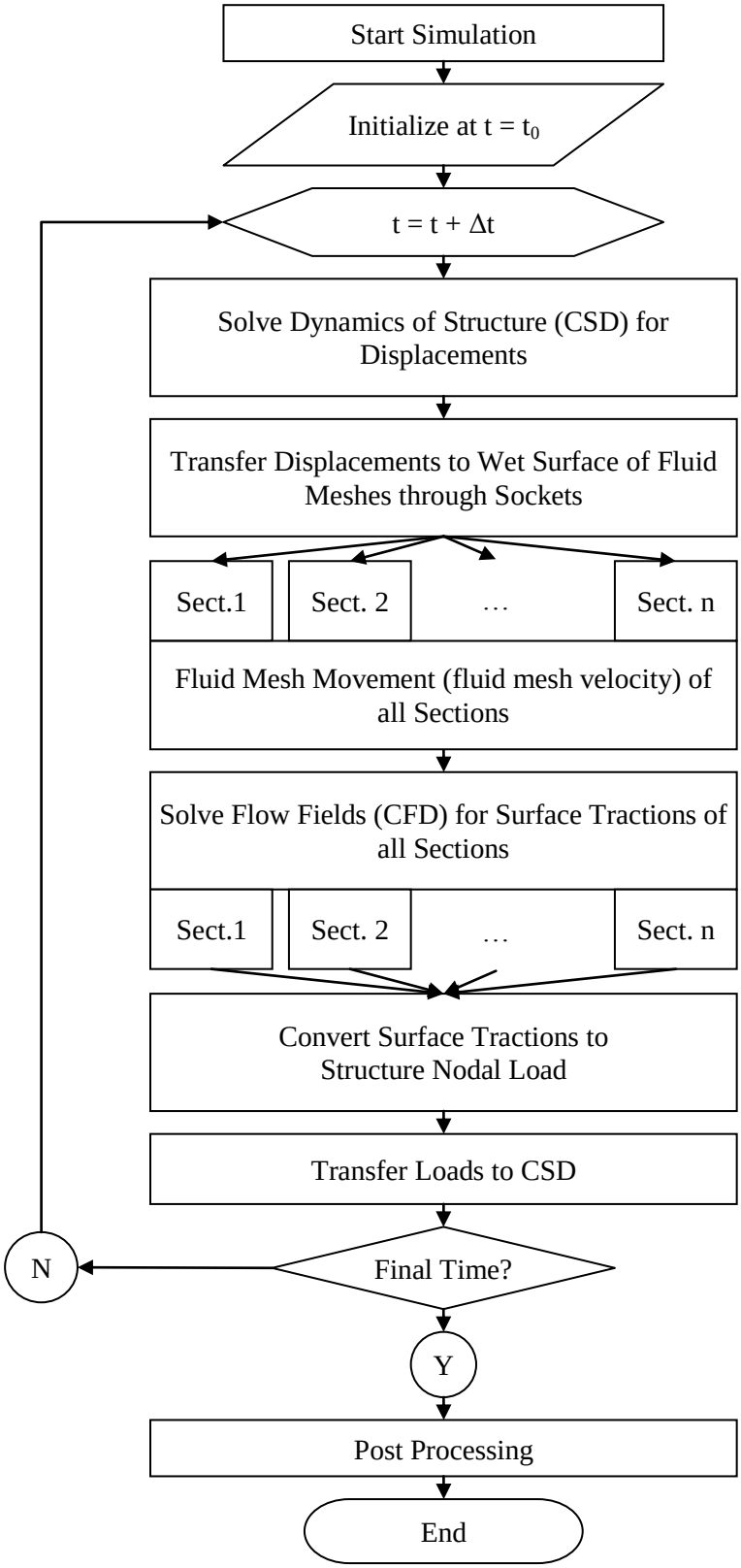

Figure 2-8: Simplified simulation flow chart

CHAPTER 3: Computational Results

In this chapter, numerical results are presented. First, considerations for a typical quality fluid mesh are explained and the fluid boundary conditions are clarified. Next, the validation test cases for the solvers are presented, and the FSI validations are described. Moreover, 2D and 3D test cases are presented to study different aspects of the galloping events, including ice accretion effect, behavior of leeward and windward conductors, wake effects, ice orientation, velocity dependency, effect of aerodynamic damping, and other related phenomena.

3.1 Computational Fluid Mesh

In order to perform an accurate flow simulation, an appropriate computational fluid mesh needs to be employed. An appropriate mesh should be able to capture important features of the flow that contribute in an accurate fluid loading estimation (both magnitude and frequency). In Figure 3-1, a typical spatial grid, type of boundary conditions, and dimensions used for the fluid domain model are shown. This is a typical fluid mesh used in 2D and Q3D calculations throughout this study. In this hybrid mesh, an O-grid is used around the profile, and the first node off the wall is placed at $y^+ < 1$ and 5 to 8 nodes are placed at $y^+ < 10$ to thoroughly capture the boundary layer. In order to capture the details of the near wake, a high resolution structured grid is used within15D[1] to 30D behind the conductor; an unstructured triangular grid is applied everywhere else. The total number of nodes is set based on the problem and placement of the far-field.

[1] D stands for diameter of the conductor or profile

However, in all cases, at least 200 nodes are placed on the profile, 60% of the nodes are placed within 4D of the profile, and the 15D to 30D near wake region has 30% of the total nodes. As the Mach number is quite low, far field boundaries are placed far enough in order to avoid boundary reflection interferences with the numerical solution. Other considerations in placing boundaries are the maximum estimated amplitude of the displacements and stability of the mesh movement algorithm in order to be able to handle large displacements and keep an acceptable grid quality at the same time. For example, if 50D peak-to-peak amplitude is estimated in a direction, a minimum of 300D far-field distance from the center of profile is considered in that direction. The boundary conditions at far-field are Dirichlet (inlet) at the upstream and upper and lower faces, and Neumann (exit) downstream (Figure 3-1). It should be noted that the grid is extruded normal to the plane, for 2 dimensional and Q3D cases, and periodic boundary conditions are applied accordingly.

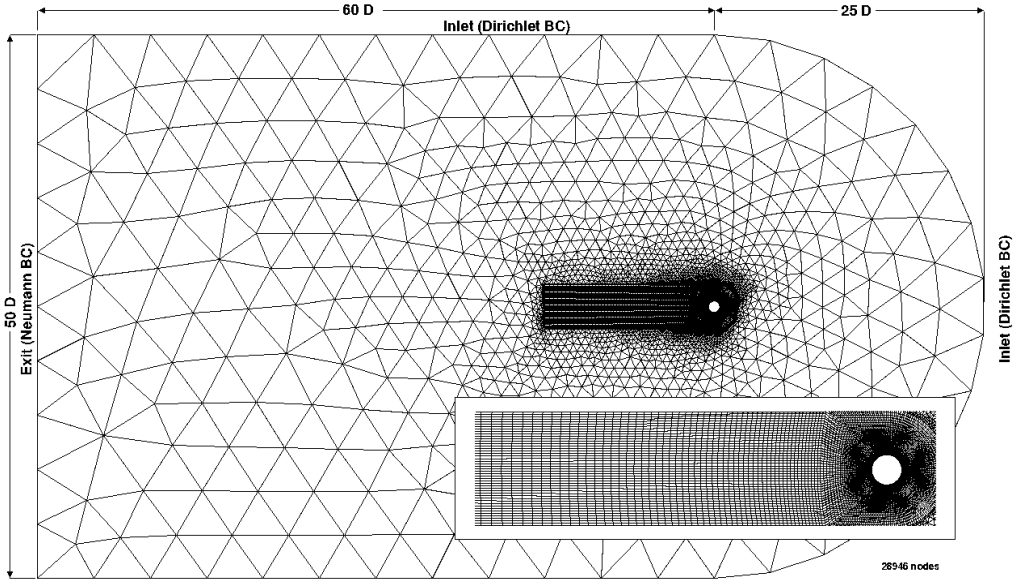

Figure 3-1: Typical spatial grid, dimensions, and boundary conditions

3.2 Validation Test Cases

In order to demonstrate the capability of the flow solver to predict details of the flow, several tests are performed. First, the time-averaged CFD results (namely drag and lift coefficients) are compared with wind tunnel experiments. Next, an infinitely long stationary cylinder has been studied over a wide range of Reynolds numbers (from 100 to 100,000) in order to explore the accuracy of CFD solver in estimating frequency of loading (or equivalently the shedding frequency). Finally, free vibration of a cylinder for which experimental and other numerical data are available is studied in order to validate the FSI framework.

3.2.1 Accuracy of Computational Aerodynamic Coefficients

In order to validate the computational aerodynamic loading, an iced shape for which wind tunnel results are available is chosen. In Figure 3-2, the wind tunnel results for time averaged aerodynamic coefficients of the M. Tunssal's shape #1 versus angle of attack are shown [27]. The rough ice thickness shown in the figure is 132% of the bare conductor diameter, and the incident wind velocity is 9.7 m/s (Re 24707). Due to the inherent unsteadiness of the flow over bluff bodies caused by vortex shedding, the aerodynamic coefficients are alternating in time. Hence, the correct comparison of these coefficients with wind tunnel data requires discarding data before the limit cycle, and performing time-averaging afterward. In Figure 3-3, the unsteady aerodynamic coefficients computed by FENSAP-ICE for angle of attack of 30° are illustrated, and in Table 3-1, the limit-cycle time-averaged values are compared with experiment. The comparison shows a good agreement.

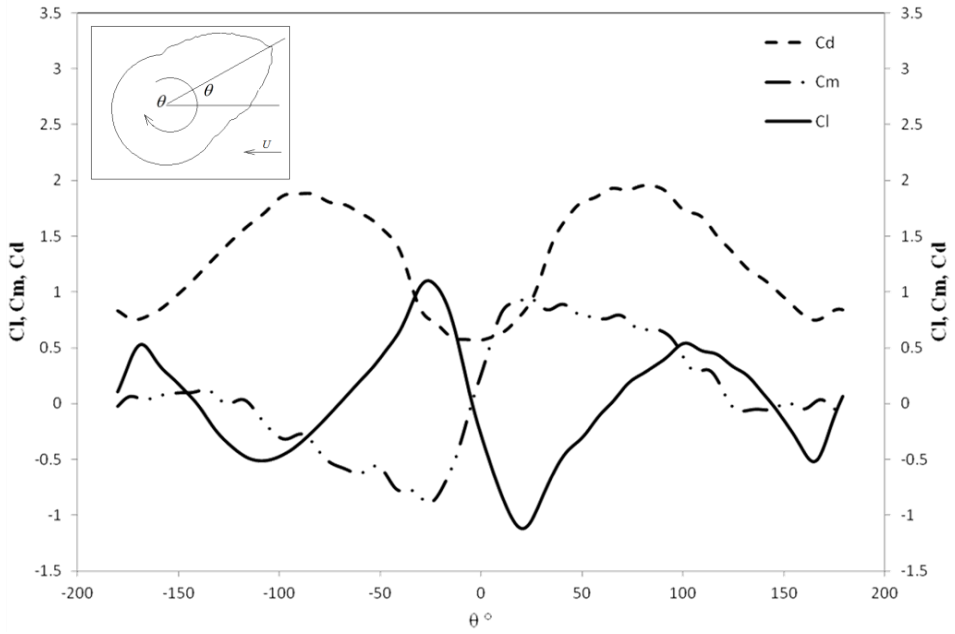

Figure 3-2: Aerodynamic coefficients of M. Tunssal Shape # 1, reproduced from Keutgen and Lilien [27]

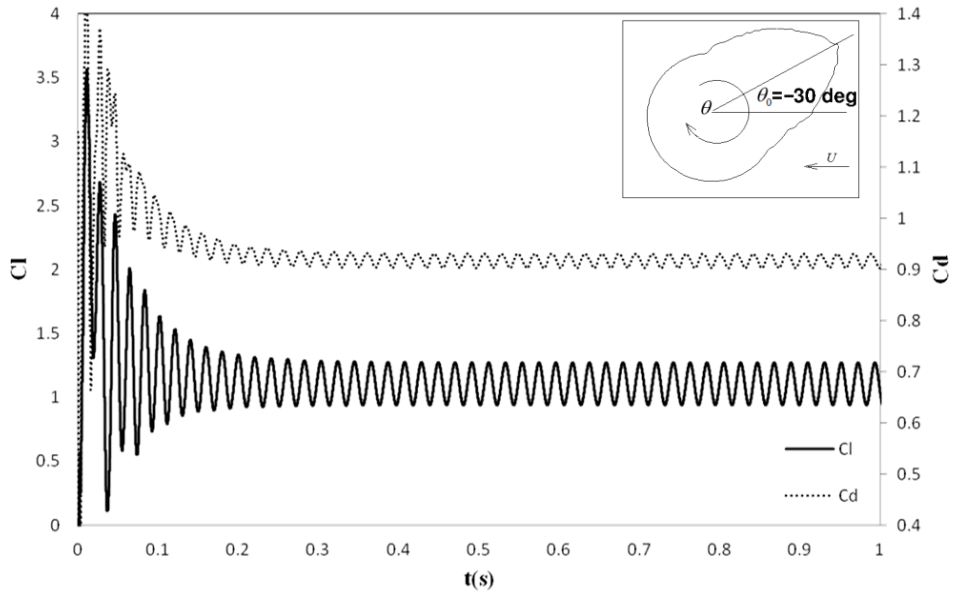

Figure 3-3: Computed unsteady aerodynamic coefficients

Table 3-1: Comparison of aerodynamic coefficients, angle of attack 30°

	Experiment	CFD
Lift coefficient	1.06	1.10
Drag coefficient	0.85	0.92

3.2.2 Loading Frequency over Stationary Cylinder

The Strouhal number is the non-dimensional form of the shedding frequency which itself is equal to the frequency of the transverse loading (lift). Therefore, studying this number reveals the capability of the flow solver in simulating the loading frequency. For each Re number, the flow field is solved around an infinitely long cylinder and the fundamental frequency of the lift coefficient[1] is obtained by performing spectral analysis (Fourier Transform). In Figure 3-4, Strouhal number versus Reynolds number is plotted along with a wide range of available experimental results [6, 58] for an infinitely long stationary cylinder. As shown, there is a good agreement with experimental results at low and moderate Reynolds numbers up to around 20,000; however, by increasing the Reynolds number, CFD over-predicts the Strouhal number. Comparison between CFD and median of the experimental results shows that for Re larger than 20,000 the difference becomes more than 7% and reaches a maximum of 20% at higher Re. Usually, CFD simulations suffer from over-predicting St at high Re numbers, unless higher order turbulence models such as LES, DES, or DNS are employed. The cost of these turbulence models at high Re numbers prevents them from being practical, particularly for unsteady simulations. On the other hand, the experimental results shown in Figure 3-4 are widely scattered for Re>100, hence there are uncertainty in the available experiments such as roughness of the cylinder and infinitely long cylinder assumption. Hence, the CFD results seem satisfactory for the current application.

[1] In the case of the smooth cylinder, there is only one frequency in the loading.

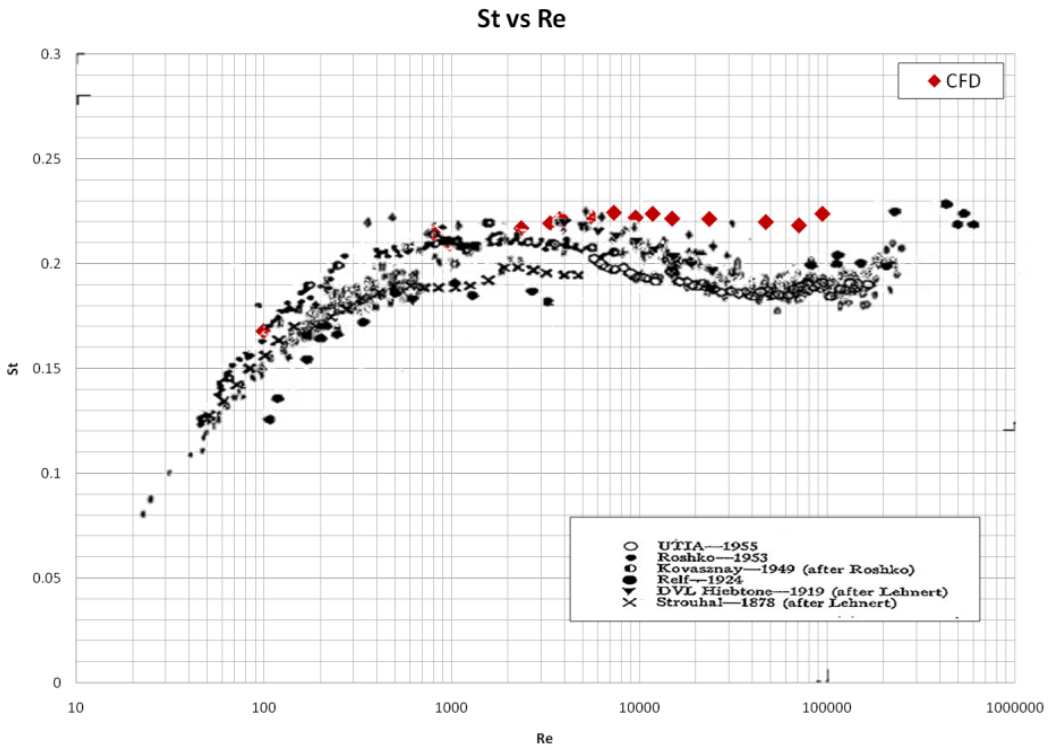

Figure 3-4: Strouhal vs. Reynolds, comparison of CFD and experiments [6]

3.2.3 Freely Vibrating Cylinder

The first step validation of the aeroelastic framework is performed by studying free vibration of a cylinder. This choice is supported by availability of reliable experiments which include different features of the problem such as flow field around and in the wake, the structural response, lock-in, phase change, and etc. The following salient analysis features are presented in this section: time accurate evolution of vortices, accuracy of the model in predicting structural response, near-wake flow structure, shedding frequency, unsteady fluid loading, and interpretation of the structural response [33].

In order to compare the results with other published studies, the structural parameters and Reynolds number range correspond to those of an experimental study performed by Khalak and Williamson [59] and a numerical study done by

Guilmineau and Queutey [32]. Hence, a mass ratio of 2.4, a mass-damping ratio of 0.013 and a Reynolds number range of 975-14923, representing a reduced velocity range of 1.124-17.21, are chosen. For all Reynolds numbers, the same structural damping is applied.

In this analysis, the EOM (2.75) can be reduced to the vertical motion of the rigid cylinder by a viscously damped linear single degree-of-freedom system with the following classical non-dimensional equation,

$$\frac{d^2Y}{d\tau^2} + 4\pi \bar{f}_n \zeta \frac{dY}{d\tau} + \left(2\pi \bar{f}_n\right)^2 Y = \frac{4}{m^* \pi} C_L \ , \tag{3.1}$$

where Y is the transverse normalized displacement, τ, the normalized time, ζ, the structural viscous damping ratio, $\bar{f}_n$, the normalized natural frequency, m^*, the mass ratio, and C_L is the unsteady lift coefficient. The normalized variables used in this equation, and other normalized variables, are defined as follows:

$$\begin{gathered} Y = y/D, \quad \tau = tU_\infty/D, \quad m^* = \frac{m}{m_d}, \quad m_d = \frac{\pi}{4}\rho D^2, \\ U^* = \frac{U_\infty}{f_n D}, \; C_L = \frac{F_y}{\rho U_\infty^2 D}, \; \zeta = \frac{c}{2\sqrt{km}}, \; \bar{f}_n = f_n \frac{D}{U_\infty} = \frac{1}{2\pi}\sqrt{\frac{k}{m}}\frac{D}{U_\infty} \ , \end{gathered} \tag{3.2}$$

In these definitions, D is the diameter of the cylinder, m, the mass of cylinder, c, the structural viscous damping, k, the stiffness, f_n, the natural frequency, F_Y, the fluid loading resulting from the fluid surface loads, U_∞, the

free-stream velocity, ρ, the free-stream density, U^*, the reduced velocity, y, the vertical displacement, and m_d is the displaced fluid mass.

Figure 3-5 shows the normalized displacement of the cylinder versus the normalized time for different reduced velocities. In these plots, the oscillations start with very small amplitudes, and as time passes, the amplitude increases until it reaches its limit cycle value. The limit cycle amplitude is unique for most of the cases; however, for some reduced velocities, e.g. at $U^* = 2.883$ and to some extend also at $U^* = 3.460$, the limit cycle amplitude beats periodically. This beating behavior in the synchronization (or transition) region is in agreement with the experimental studies of Brika and Laneville [60]. The onset of relatively large oscillations differs with reduced velocity. For $\mathrm{Re} < 1500$ and $\mathrm{Re} \geq 9000$, corresponding to the head of the initial excitation branch and the tail of the lower branch, respectively, large oscillations start at around $\tau = 100 - 150$; while, for $1500 < \mathrm{Re} < 9000$, which includes the transition regions and the upper branch, instabilities become noticeable quite earlier at around $\tau = 40 - 50$.

A close investigation of Figure 3-5 shows that within the initial excitation and lower branches, oscillations are of regular bell shape type with one dominant frequency, but inside the upper branch, varying amplitude and beating behavior can be seen. At low reduced velocities, amplitudes are very small (e.g. 0.013 at $U^* = 1.124$), but as velocity increases, the amplitude amplifies dramatically. In the initial-upper transition region, oscillations do not stabilize at a constant value. For example, at $U^* = 2.883$, the amplitude changes between 0.15 and 0.35 (see

Figure 3-5 and scatter lines in Figure 3-7). The amplitude increases through the upper branch and reaches a limit value; however, in this region large displacements start with an overshoot. By further increasing U^*, the amplitude decreases rapidly until the beginning of the lower branch at $U^* \approx 6.4$ where the decrease rate is reduced. At $U^* \approx 9$, the amplitude decreases rapidly until $U^* = 12$ where it reaches the small value of 0.034, from this point forth, the change of amplitude with reduced velocity is negligible. Similar to the initial branch, the response of the cylinder in the lower branch is regular and only one dominant frequency is notable.

In Figure 3-6, the power spectral density (PSD) estimates for various Reynolds numbers representing the frequency response of the cylinder in different branches, are plotted. In the initial branch, e.g. Re 1500, the PSD of the vertical displacement shows one dominant frequency at 4.78 Hz which is equivalent to the frequency ratio of 0.39, this compares well with the experimental data in Figure 4 of Khalak and Williamson [61] in which the expected frequency ratio for this Re is around 0.38. By increasing the reduced velocity and reaching the initial-upper transition region, the PSD becomes broader. For instance at Re 2500, at least two distinct peaks with almost equivalent strengths exist, demonstrating the beating behavior. In the upper branch, at Re 3911 for instance, Figure 3-6 demonstrates a single dominant frequency as observed by Khalak and Williamson [61]. In the lower branch, at higher Reynolds numbers such as 7310 and 12000, the shedding returns to a single dominant frequency.

The normalized amplitude of displacements at their limit cycle versus reduced velocity is presented in Figure 3-7. In this figure, vertical bars are used to show the range of varying amplitude in the limit cycle, and where the large displacements start with an overshoot. Also in the same figure, the experimental results of Khalak and Williamson [59] are included for comparison. The maximum computed amplitude happens at $U^* = 4.510$. At this reduced velocity, large displacements start with an overshoot of 0.94, and then the oscillations end up at the limit cycle amplitude of 0.83. These values are lower than the experimental value of 0.96. In the numerical study of Guilmineau and Queutey [32], a maximum amplitude of 0.98 is reported at $U^* = 4.510$, with increasing velocity initial condition[1]. Considering the different initial condition used in this study, the predicted maximum amplitude and the overall trend of the results are deemed satisfactory and show agreement with the experiment. The computed amplitudes in the initial and lower branches consistently agree with the experiment. Moreover, the upper branch results are encouraging. It seems that employing greater concentration of points around the cylinder and in the near wake region has made it possible to capture the upper branch while the upper branch had not been captured by other published numerical studies, see e.g. [32, 62].

In Figure 3-8, the frequency ratio versus the reduced velocity is compared with the experimental results. The computed frequency follows the experimental

[1] The free stream velocity is increased from an initial value gradually up to a target value while the cylinder oscillates.

results everywhere, except in the tail of the lower branch where the amplitude of oscillations is very small and the frequency is high. In fact, numerical studies suffer from predicting accurate shedding frequency at high Reynolds numbers. Even in the case of the fixed cylinder, the numerical shedding frequency at high Reynolds numbers is lower than the experimental values. This difference for $U^* > 12$ is also reported in other computational studies. In this region, the cylinder experiences very small oscillations; therefore, the importance of the frequency ratio is secondary. Several studies show the presence of the lock-in phenomenon in vortex-induced vibrations in which the structural motion dominates the shedding development, then the shedding frequency shifts to the structural frequency, i.e. $f_s \approx f_n \approx f_c$, see, e.g., [30, 60, 63]. It is shown experimentally that for high mass ratios, the frequency ratio f^* is close to unity; however, as the mass ratio decreases, the frequency ratio departs from unity and reaches a higher value. Figure 3-8 shows the frequency ratio of 1.2 within the lock-in region, i.e. $U^* = 4.6 - 12$, which is lower than the experimental value of 1.4 reported by Khalak and Williamson [61]. Close investigation of the frequency response and time history of the displacements (Figure 3-5) shows that the onset of the large oscillations happens within the lock-in region. Past the lock-in region, the amplitude of oscillations drops to a very small value and remains unchanged.

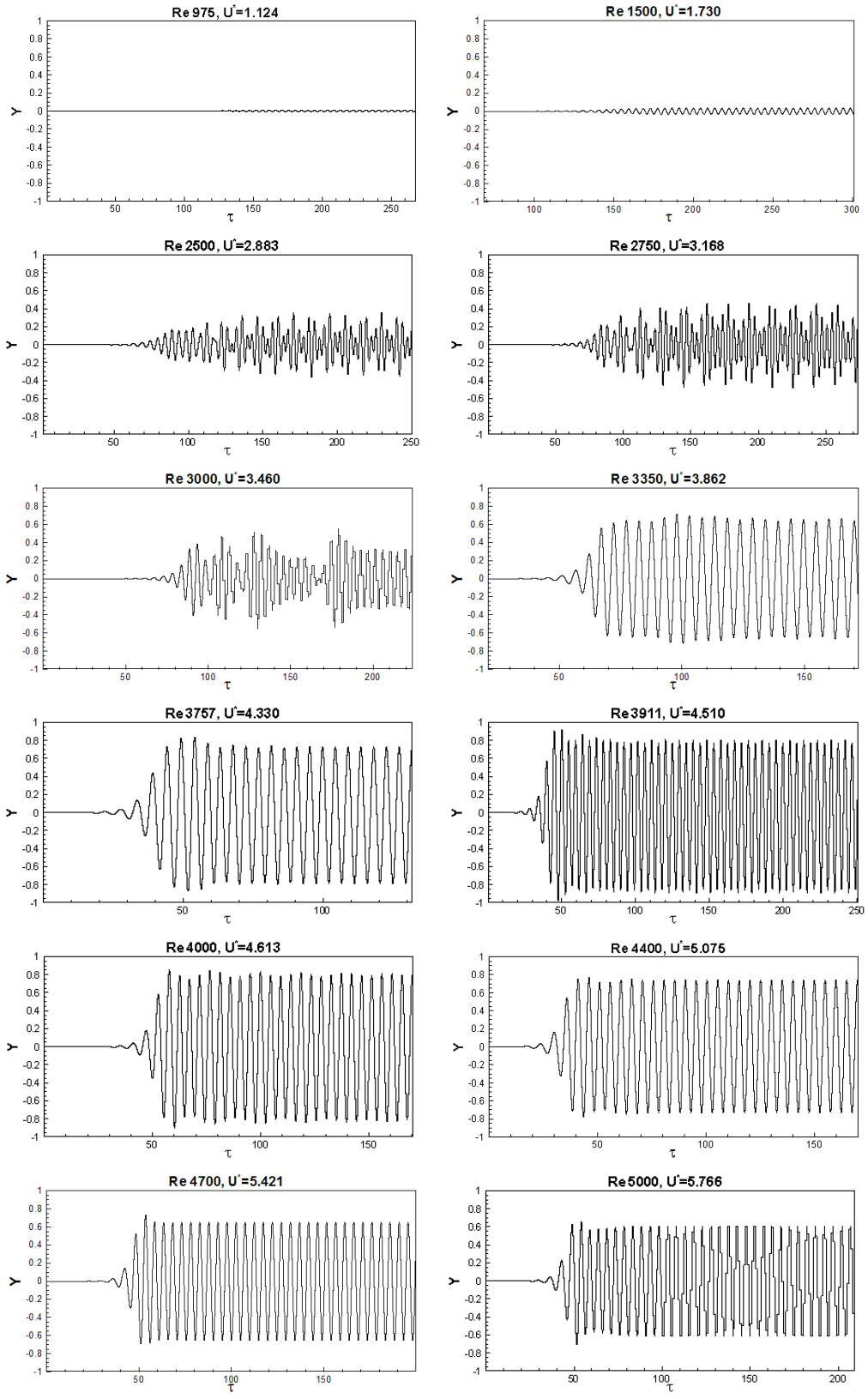

Figure 3-5: Normalized time history of vertical displacement of the cylinder ($m^* = 2.4,\ m^*\zeta = 1.3\times10^{-2}$) at various reduced velocities

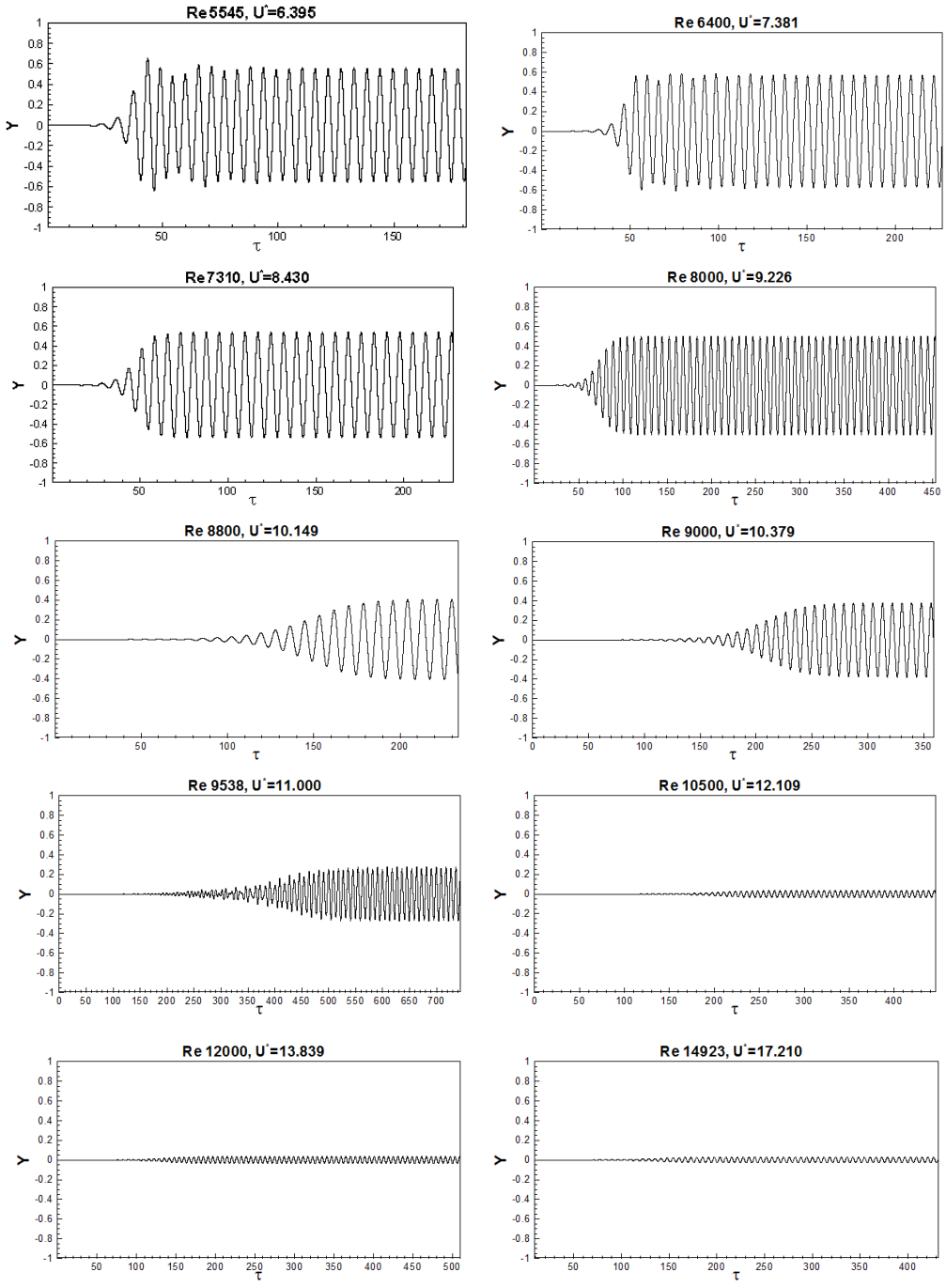

Figure 3-5 (cont'd.). Normalized time history of displacement of the cylinder ($m^* = 2.4,\ m^*\zeta = 1.3\times10^{-2}$) at various reduced velocities

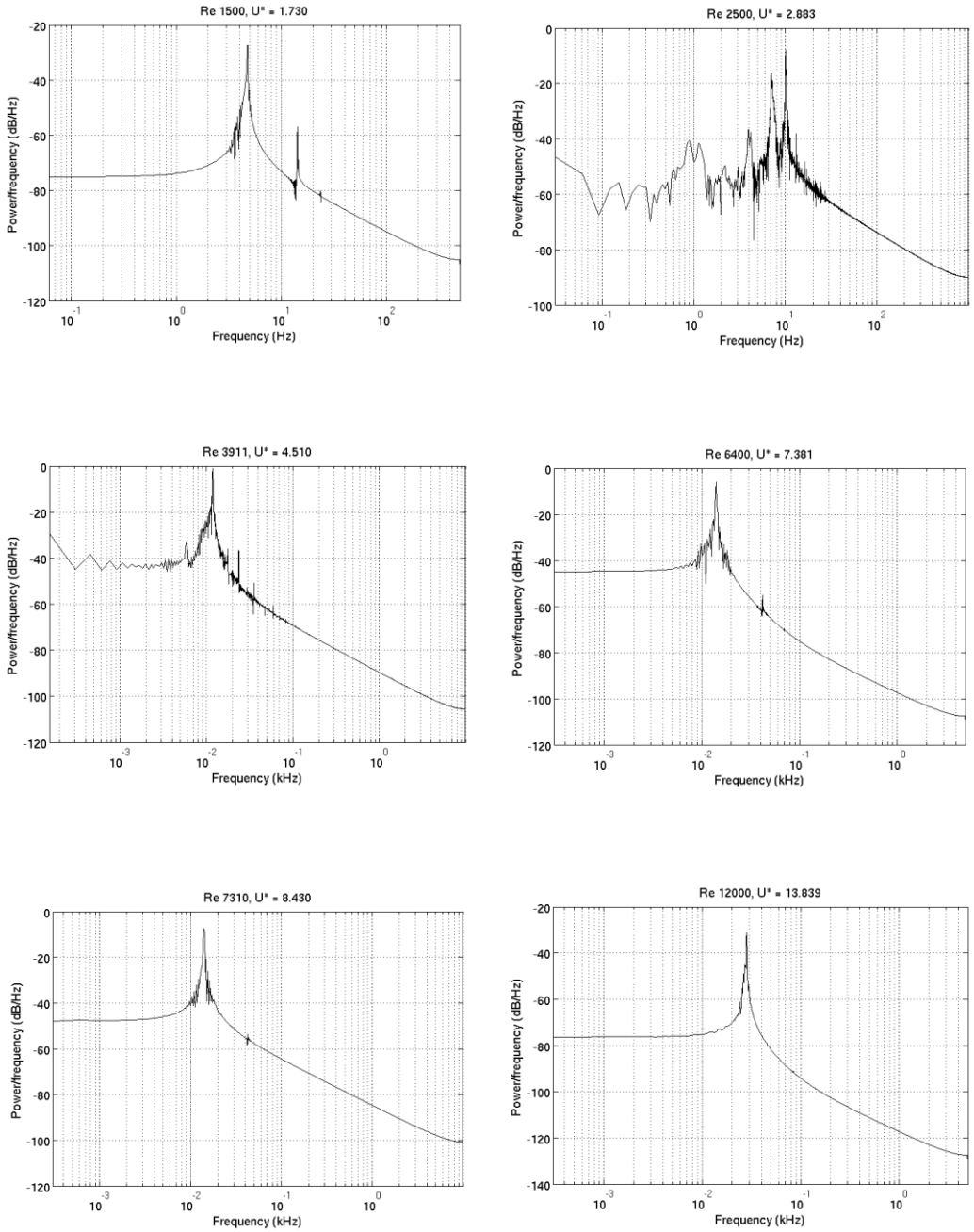

Figure 3-6: Periodogram Power Spectral Density (PSD) Estimate of the vertical displacements at various reduced velocities

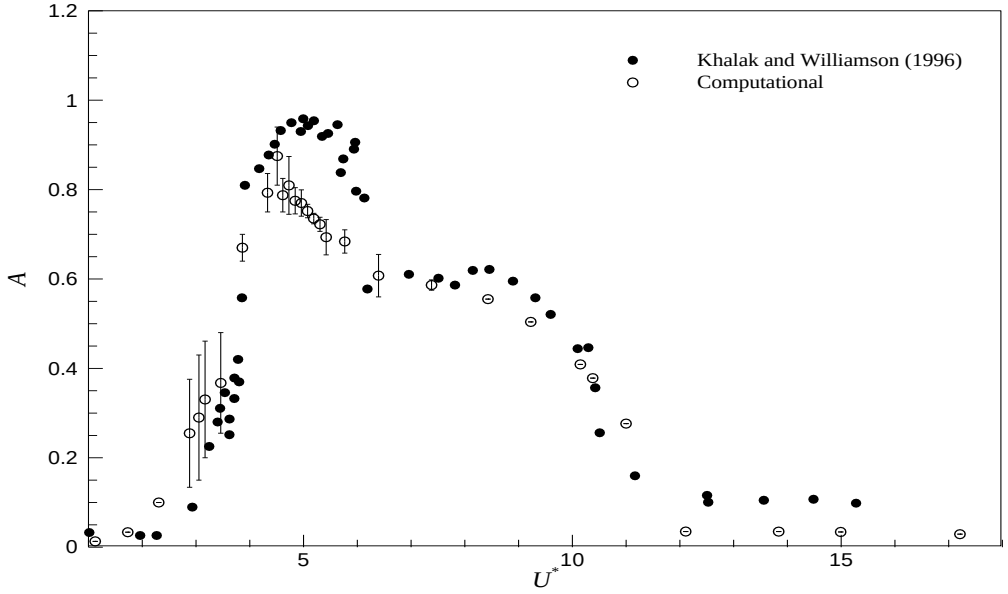

Figure 3-7: Limit-cycle amplitude versus reduced velocity, $m^* = 2.4$, $m^*\zeta = 1.3\times10^{-2}$; scatter bars show varying amplitudes obtained by FSI analysis

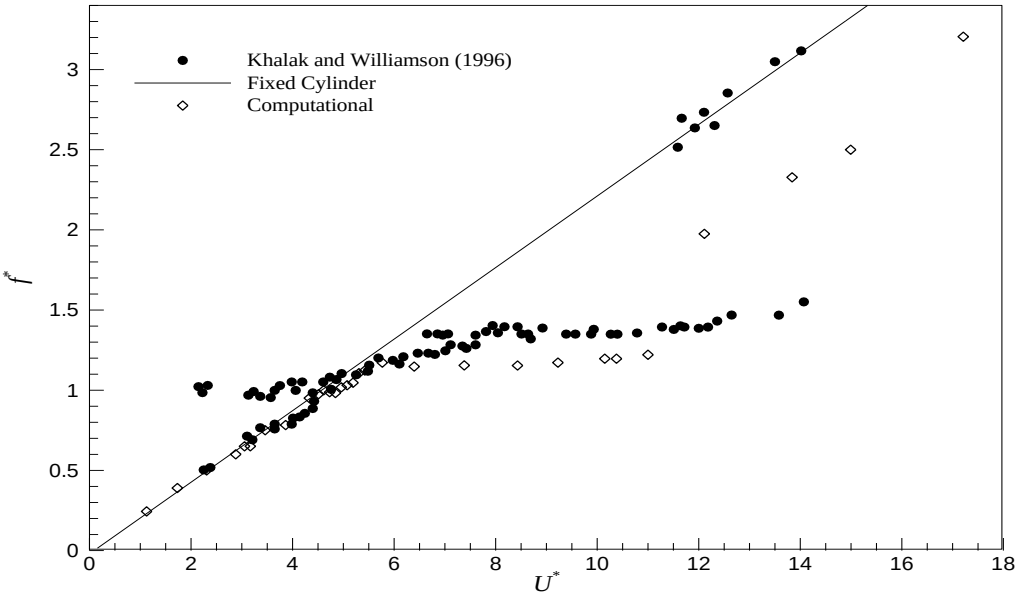

Figure 3-8: Frequency ratio versus reduced velocity, ($m^* = 2.4,\ m^*\zeta = 1.3\times10^{-2}$)

Figure 3-9 presents the loading (lift and drag coefficients) history for different reduced velocities. At low reduced velocities, the fluctuations of the drag coefficient are smaller than those of the lift coefficient, but by increasing the reduced velocity, these fluctuations become of the same order until the cylinder

reaches its maximum amplitude. From this point forth, the fluctuations of drag become greater than lift fluctuations, and the mean drag coefficient reaches its maximum value at maximum amplitude. As exposed area of cylinder reaches its maximum at the highest amplitude, coincidence of the maximum amplitude and maximum drag is predictable. By further increasing the reduced velocity, fluctuations of both the lift and drag coefficients decrease and reach a small value at high reduced velocities. An interesting observation is the loading history at the initial-upper transition region (Figure 3-9, $U^* = 2.883 - 4.330$). In this region, similar to the displacement response, the amplitude of the loading varies with time and the regular loading seen in other regions is not observed.

Figure 3-10 shows the effect of transverse oscillations on the drag coefficient. In this figure, the computed mean and maximum drag coefficients are plotted versus reduced velocity. As the area of the cylinder exposed to the flow increases with amplitude, the cylinder is expected to experience a greater drag force as amplitude increases. As expected, results show that both the mean and maximum drag coefficients reach their peak value at maximum amplitude. The peak drag force on the oscillating cylinder is larger than on a fixed cylinder; in the current case, the peak mean drag is three times larger than the drag coefficient of a similar fixed cylinder. This phenomenon cannot be captured by quasi-steady assumption in which the drag is considered only function of relative angle of attack. Hence, another limitation of quasi-steady analysis is shown.

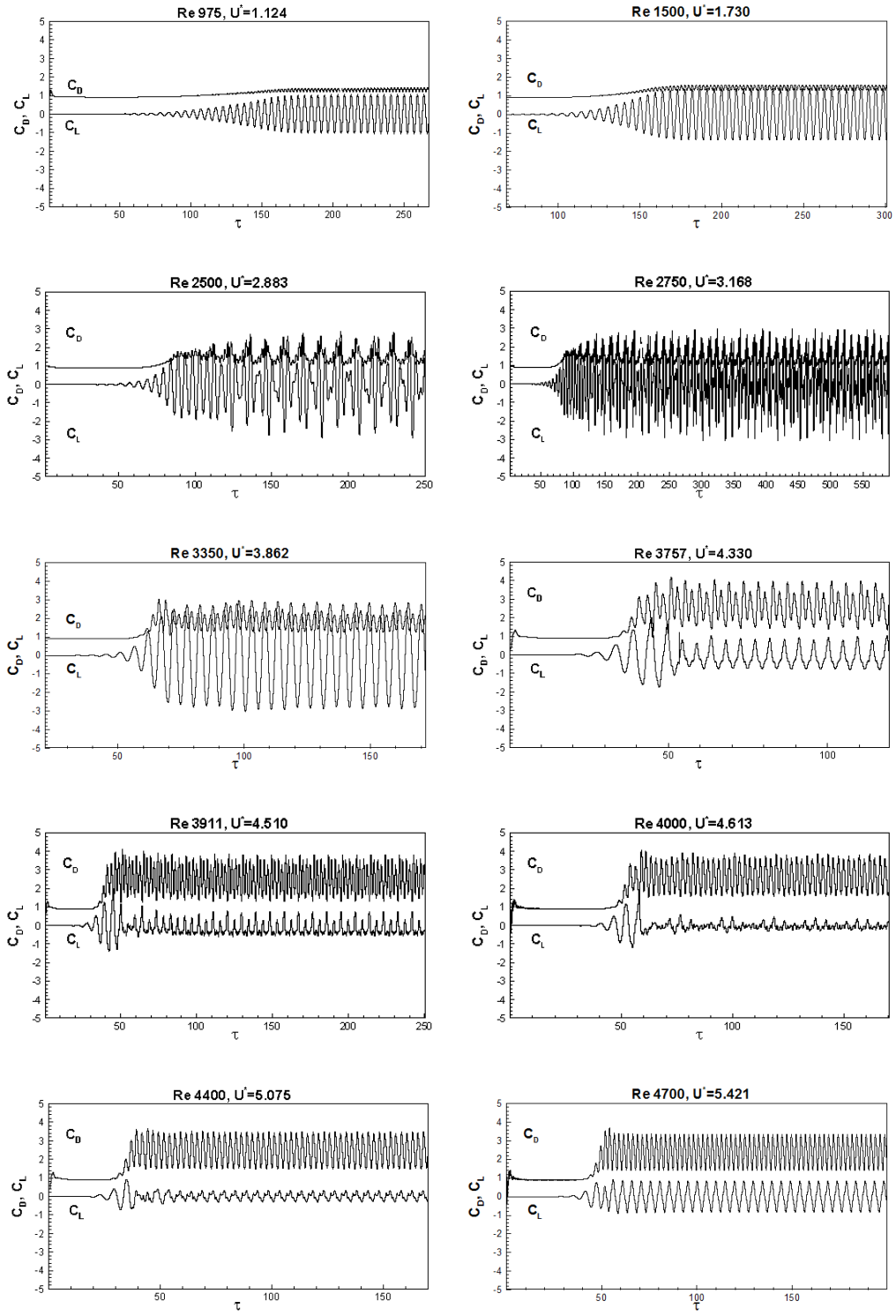

Figure 3-9: Normalized Time history of loading over the vibrating cylinder ($m^* = 2.4,\ m^*\zeta = 1.3\times10^{-2}$) at various reduced velocities

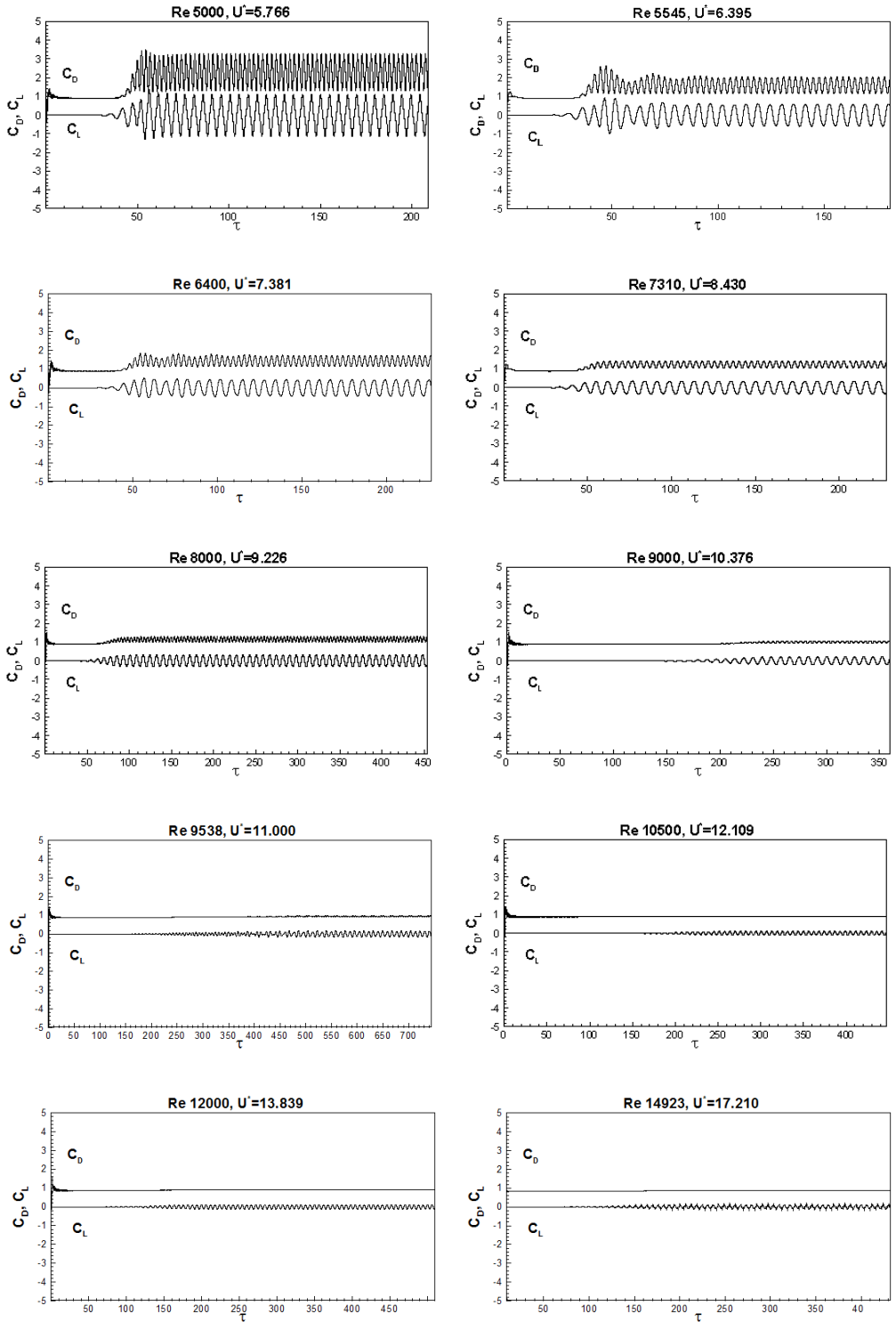

Figure 3-9: (cont'd): Normalized Time history of loading over the vibrating cylinder ($m^* = 2.4,\ m^*\zeta = 1.3\times10^{-2}$) at various reduced velocities

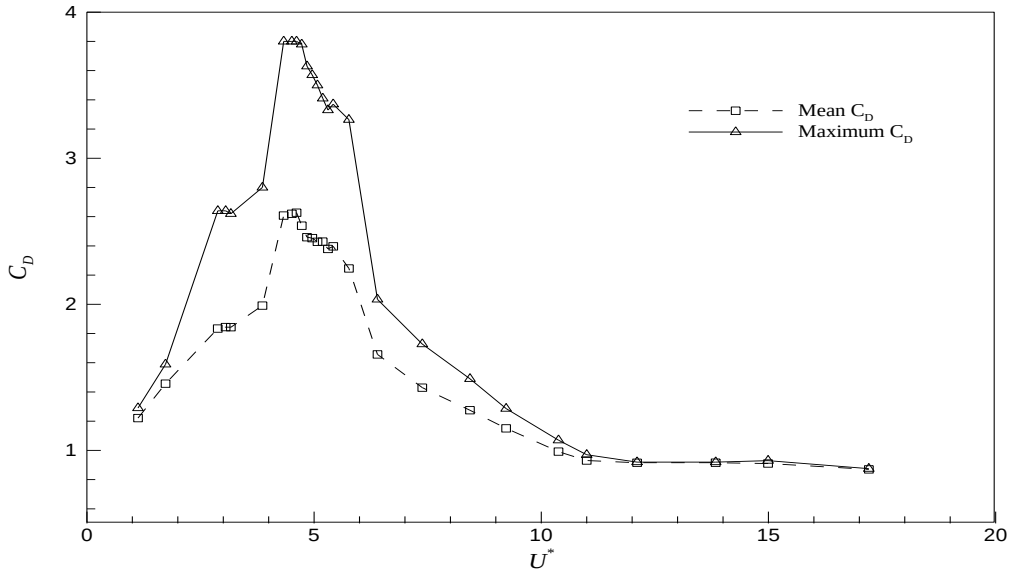

Figure 3-10: Mean and maximum drag coefficients versus reduced velocity of oscillating cylinder, ($m^* = 2.4,\ m^*\zeta = 1.3\times10^{-2}$)

The phase angle, Φ, between the lift force and the displacement response, versus the reduced velocity is plotted in Figure 3-11. For $U^* < U^*_{\max\_Y}$, the phase angle is near zero while, after passing the maximum amplitude, the phase angle jumps to around +185 degrees.

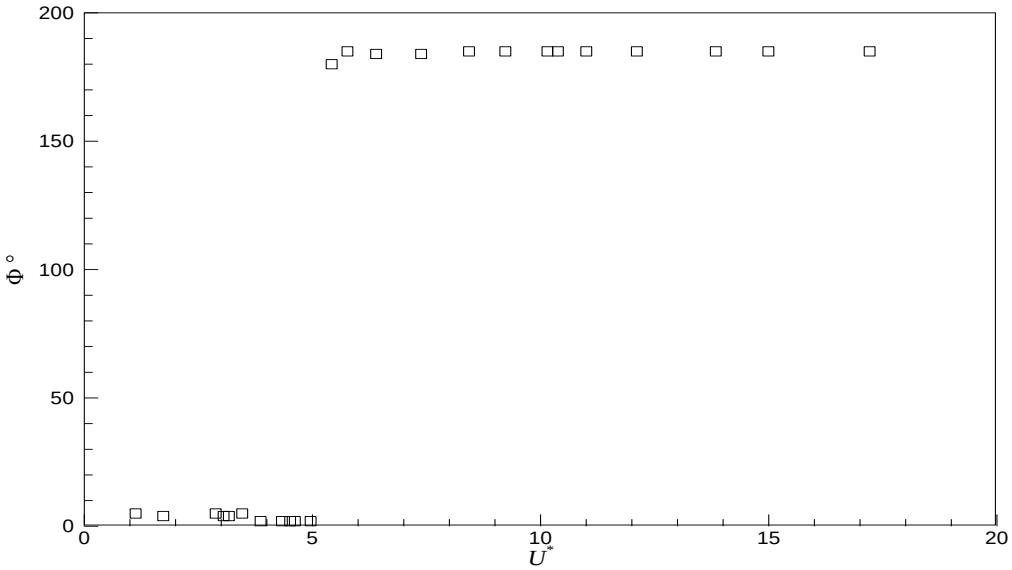

Figure 3-11: Phase angle versus reduced velocity of the oscillating cylinder, ($m^* = 2.4,\ m^*\zeta = 1.3\times10^{-2}$)

The vortex shedding mode and structure of the vortices alter the aerodynamic loading and damping of the cylinder. Consequently, this affects the response of the cylinder. On the other hand, the frequency and amplitude of the oscillations changes the shedding mode and structure of the vortices. Thus, studying the structure of the vortices and shedding modes facilitates understanding of the connection between the shedding modes and the structural response at different Reynolds numbers. Following the interpretation of Williamson and Roshko [64], flow visualization behind the oscillating cylinder is explored in Figure 3-12. In the literature, 2S and 2P vortex shedding modes are reported for this problem, see e.g. [60]. As illustrated schematically in Figure 3-13, in 2S mode, two single vortices are fed into the downstream per shedding cycle and in 2P mode, two vortex pairs appear per shedding cycle. Figure 3-12 shows the vortex pattern behind the oscillating cylinder for the studied incident flow conditions. At low reduced velocities, the flow has enough time to generate repeatable vortex patterns, and small amplitudes keep the shedding area narrow, thus a pure periodic 2S mode appears as illustrated in Figure 3-12(a). By increasing the reduced velocity and reaching the initial-upper transition region, the amplitude beats, and the required time and space to complete a full 2P or 2S shedding cycle is not available. Therefore, the mode alternates between 2S and 2P; see Figure 3-12 (b-e). The mode switching in this region is related to the previously mentioned beating behavior in the displacement response and loading. By increasing the reduced velocity and reaching the upper branch region, the vortex street keeps expanding, and the 2P mode becomes dominant; Figure 3-12 (f-j). This change in shedding mode coincides with the phase angle shift from 0 to +180 degrees. The widest

vortex street appears in the upper-lower transition where the frequency ratio jumps at the end of the lock-in region (see Figure 3-8). By further increasing the reduced velocity, the vortex street becomes narrower, see Figure 3-12 (k), and it seems that the vortex pattern tends to return to 2S mode afterward. The vortex structures in different regions and alternation of the shedding modes in the transition regions are in agreement with the experiments of Brika and Laneville [60] and Williamson and Roshko [64].

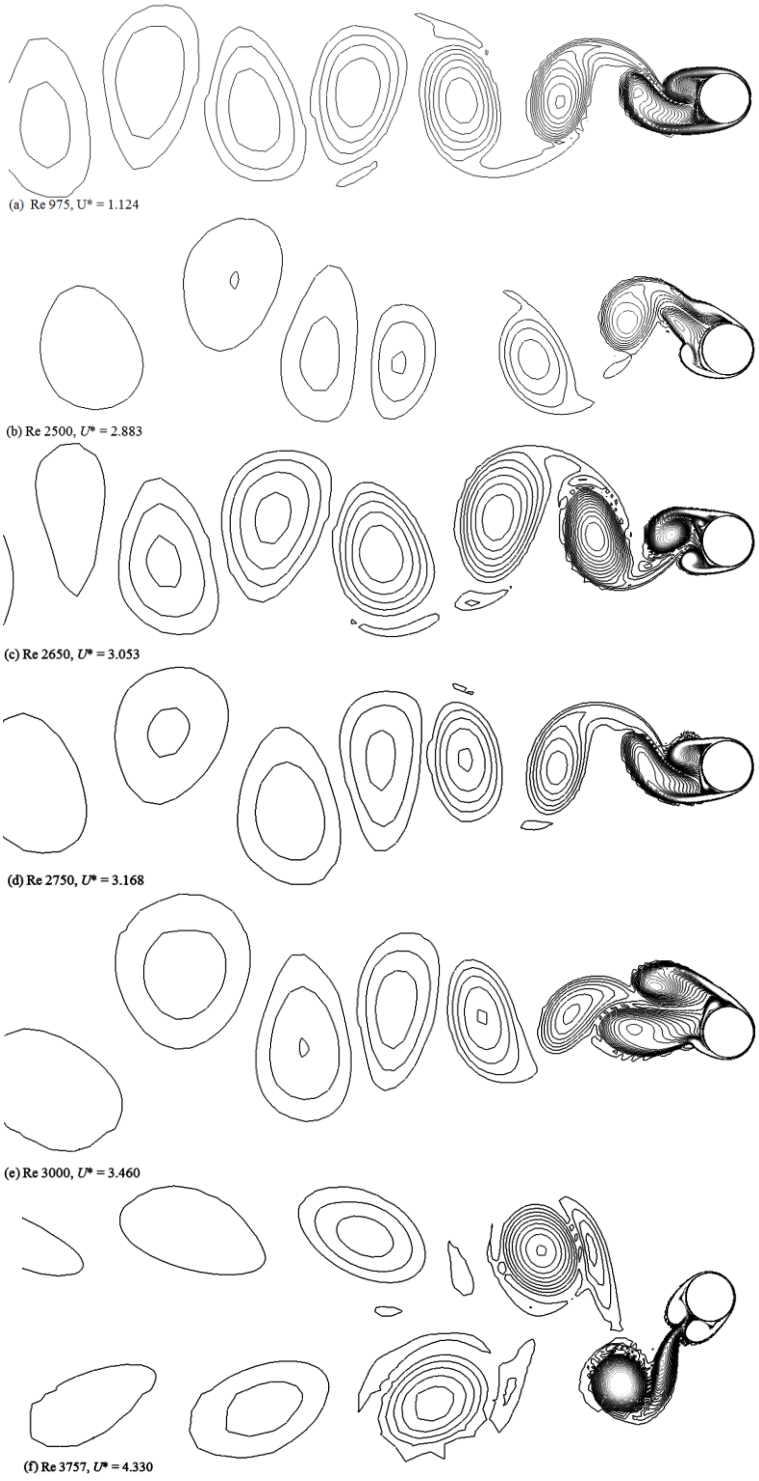

Figure 3-12: Instantaneous vorticity contours for different Reynolds numbers of the oscillating cylinder, ($m^* = 2.4,\ m^*\zeta = 1.3\times10^{-2}$)

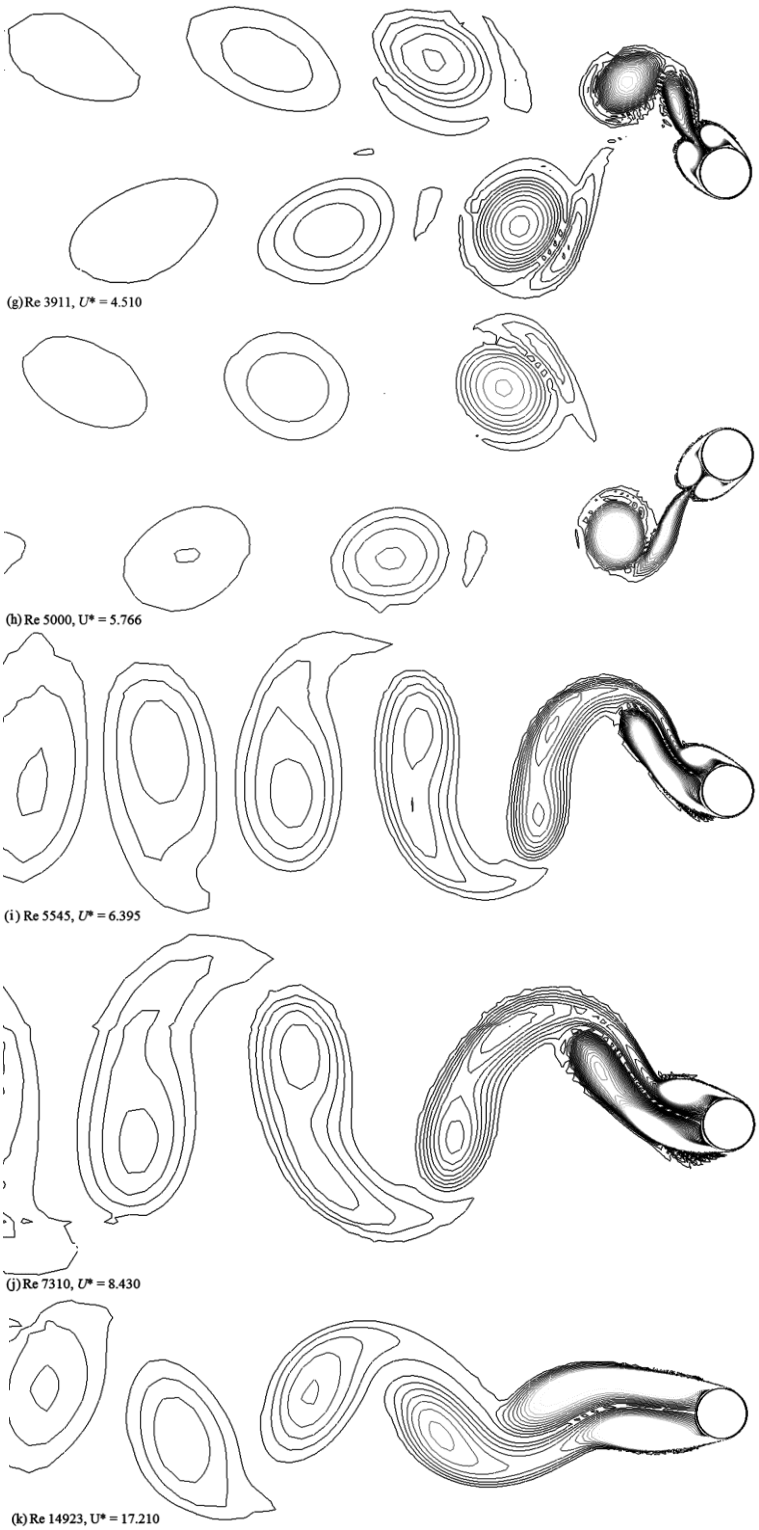

Figure 3-12 (cont'd): Instantaneous vorticity contours for different Reynolds numbers of the oscillating cylinder

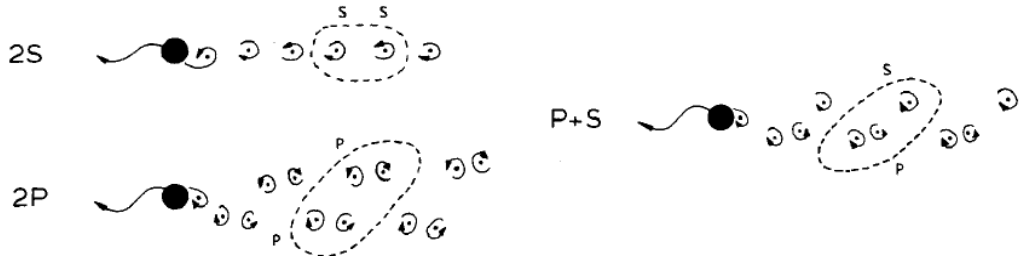

Figure 3-13: Sketches of vortex shedding patterns, reproduced from Williamson and Roshko [64]

Finally, in Figure 3-14, the computational results are summarized in one graph to facilitate analyzing different aspects of VIV response and their effects on each other. A first observation is the coincidence of the maximum drag force and the maximum amplitude with the shift of phase angle from 0 to 180 degrees. At this point, the vortex shedding mode switches to 2P, as well. The lock-in region, where the frequency ratio reaches almost a constant value, starts at the upper-lower branch border, and ends when the displacement amplitude drops to a small value. At this point, the drag force and the amplitude reach their lowest values, and the frequency ratio starts to increase.

In the absence of DNS and LES models for moderate Reynolds numbers applications, the present cost-effective numerical methodology shows that URANS models can be efficiently used to predict the salient features of the flow around freely vibrating bluff bodies including the near wake structure, the shedding modes, and unsteady loading. Moreover, the numerical results including structural and frequency responses, vortex shedding modes, phase angle, and history of developing large displacements, are compared with experiments and show very good agreement.

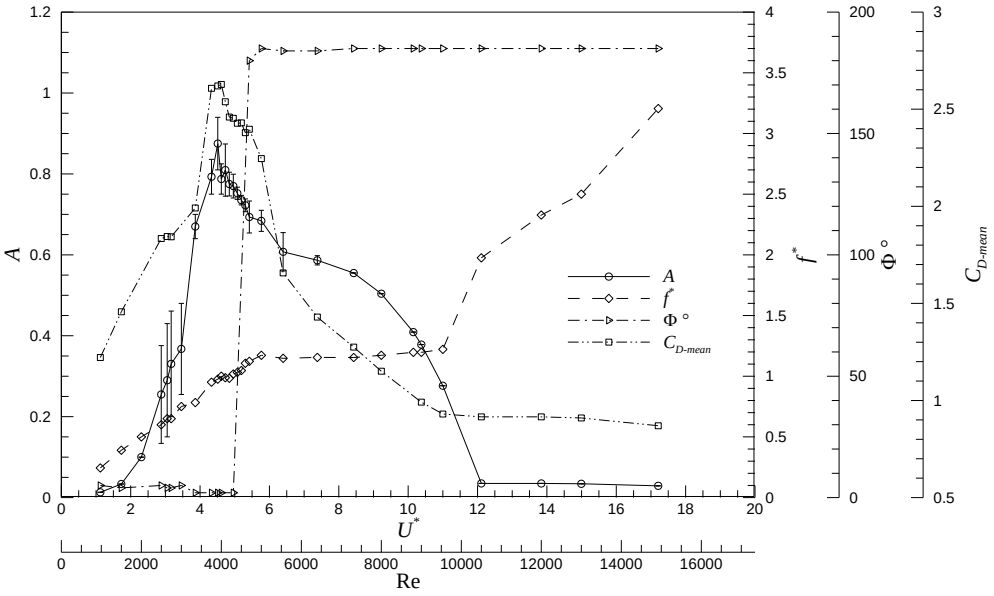

Figure 3-14: Summary of computational results

3.3 Iced Conductor Galloping

In this section, in-plane cross-sectional oscillations of an elastically mounted iced-conductor are studied with a three-degree-of-freedom model in the horizontal, vertical and torsional (rotational) directions using FSI analysis [65]. In this problem, the displacement vector of the EOM becomes $\{q\} = (x, y, \theta)^T$. In order to compare results with the wind tunnel experiment of Keutgen and Lilien [27], the predefined ice profile shown in Figure 3-2, which is the M. Tunstall's shape #1 [66], with maximum thickness of 132% of the bare cable radius, is adapted over a conductor cross section with 32.5 mm diameter. The initial angle of attack of the incident wind on the iced conductor is 30 degrees, which also corresponds to the initial ice accretion angle in this problem. The non-dimensional time step, $U_\infty \Delta t / D$, is selected on the basis of satisfactory numerical performance described in §3.4. The structural properties are taken from [27]; the natural frequencies (in Hz) of the solid bluff body on flexible supports are 0.995, 0.845,

and 0.865 in the horizontal, vertical, and torsional directions, respectively. The mass per unit length of the cylinder is 3.25 kg/m, and based on the available data and geometry, the mass moment of inertia per unit length is estimated as 0.0394 kg-m^2/m (no explicit value for this parameter is given in [27]). The structural damping is set to 0.08% of critical viscous damping for horizontal and vertical motions, and 0.3% for rotation. The ice density is assumed of 0.7 g/cm^3, and the incident flow conditions vary from wind speeds of 2.4 to 19.4 m/s, corresponding to Re values of 6000 to over 49400.

Figure 3-15 shows the detailed flow field and stream lines around the body for different Reynolds numbers. As shown the flow separates at maximum ice thickness on the upper part of iced cylinder. This separation point is much earlier than that of the bare conductor, making a larger wake and separation zone, and causing greater aerodynamic loading compared to the bare conductor. Hence, the size of wake is directly governed by the maximum amplitude of rotations.

Aerodynamic loading for Reynolds numbers 9000 and 12736 are plotted in Figure 3-16, which illustrates that unlike the bare conductor, the time-averaged lift (C_y) and moment (C_{mz}) coefficients are not zero.

By increasing Reynolds number, the frequency of vortex shedding increases, the Vortex Street becomes wider, and consequently the loading frequency increases from 10 Hz at Re 6000 to around 65 Hz at Re 49414, see [65] for details. The computational results are compared in Table 3-2 with those available from the wind tunnel experiment. In this table, f_0 is the frequency of the motion

of the solid body, A, the maximum amplitude, X, the horizontal, Y, the vertical, and θ, the rotational directions. There is a good agreement between the numerical and wind tunnel results: The frequency is the same for the three directions of motion in each case, with a 3% underestimation from the computational model. There is less variability in the prediction of the amplitude of the translational oscillations, with a maximum difference of about 8%. However, torsional amplitudes are different. As the response frequencies and other amplitudes are in good agreement, it is deemed plausible to explain this difference by the uncertainty of the mass moment of inertia used in the model, which could only be estimated from the available data.

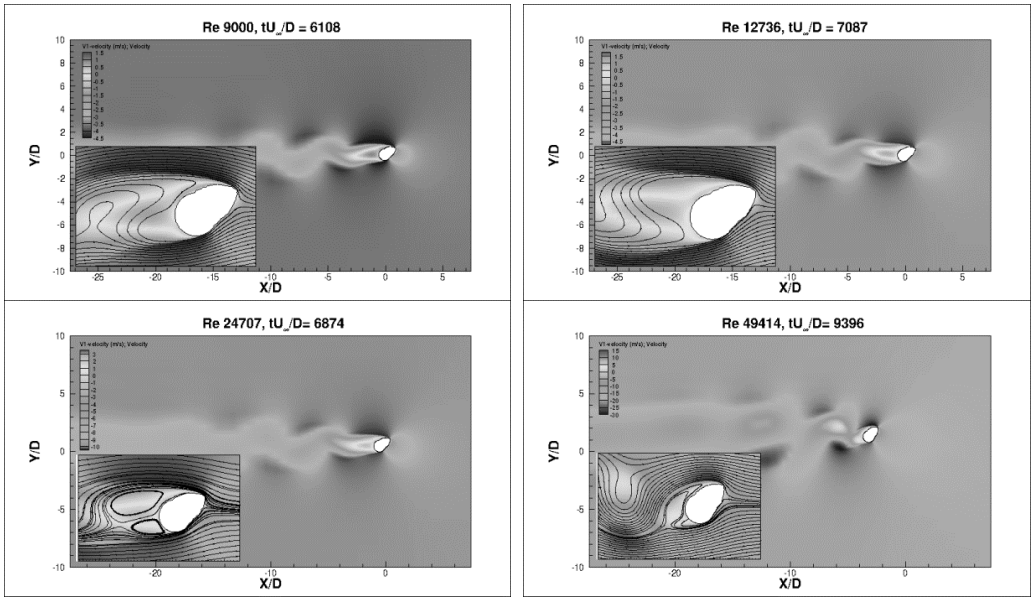

Figure 3-15: Flow field details and velocity magnitude contours

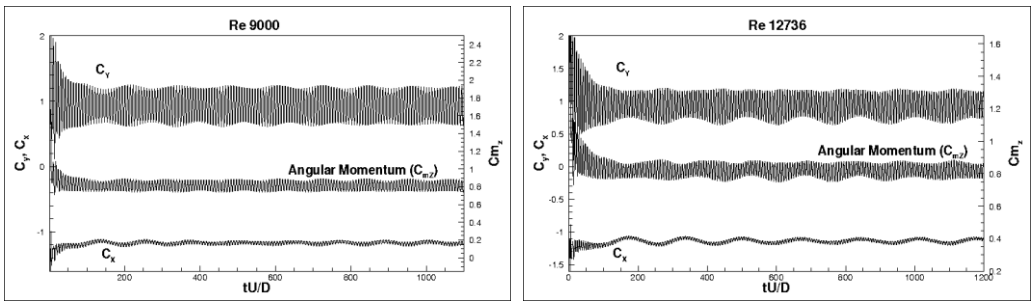

Figure 3-16: Unsteady aerodynamic loading at Re 9000 and 12736

Table 3-2: Comparison of results with Keutgen and Lilien [27]

Test	U(m/s)	Re	Amplitude			$f_0\,(Hz)$		
			A_X/D	A_Y/D	θ°	X	Y	θ
Current	9.7	24707	0.55	0.85	5.6	0.85	0.86	0.86
Ref. [67]	9.7	24707	0.51	0.91	15.2	0.89	0.89	0.89

Cables moving in air are high mass ratio bodies; therefore, depending on the Reynolds number two branches of responses are expected, the initial excitation and lower branches. In the initial excitation branch, the amplitude of the oscillations increases with Reynolds number, while in the lower branch, by increasing the Reynolds number, the amplitude decreases (see [30, 60] for detailed definitions of response branches and other physical behavior of the high mass ratios). The frequency ratio, on the other hand, is close to unity for both branches except at very high Reynolds numbers. However, the range of Reynolds numbers for conductor galloping is generally low and falls in the initial branch of response. In Table 3-3, the results obtained from the numerical simulations are summarized. The results show that in the range of Reynolds numbers studied, the fundamental frequencies of the cable motion (f_0) are close to the natural

frequencies of the oscillator (f_n), i.e. the frequency ratio, f^*, is close to unity. In addition, the amplitudes of the conductor motion in all three directions tend to increase monotonically with Reynolds number, which shows that they all fall in the initial branch of response.

Table 3-3: Amplitudes and fundamental frequencies of conductor motion

Re	Amplitude			$f_0(Hz)$			$f^* = f_0 / f_n$		
	A_X/D	A_Y/D	θ°	X	Y	θ	X	Y	θ
6000	0.043	0.048	0.38	0.992	0.839	0.870	0.997	0.993	1.006
9000	0.084	0.105	0.84	1.000	0.848	0.865	1.005	1.004	1.000
12736	0.143	0.215	1.56	0.977	0.854	0.854	0.982	1.011	0.987
24707	0.552	0.849	5.62	0.839	0.858	0.858	0.843	1.015	0.992
49414	3.903	3.577	23.52	0.992	0.824	0.810	0.997	0.975	0.936

The trajectory of the centroid of the iced conductor in the x-y plane is known as the galloping ellipse. The size and shape of this trajectory are important factors in the transmission line design to determine the clearance distance between the adjacent conductors. Figure 3-17 shows the galloping ellipses for different Reynolds numbers. As shown, at lower Reynolds numbers, initially, the conductor motion starts with similar amplitudes in both the horizontal and vertical directions, making for an X-shaped trajectory. Then, after a sustained motion is established, the horizontal amplitude decreases, while the vertical amplitude is almost invariant, and the ellipses become narrower in the horizontal direction (see denser lines in the figure), i.e. the horizontal amplitude decreases. At higher Reynolds numbers, the ratio of the vertical to horizontal amplitudes is larger than

unity from the start, and the galloping ellipses become progressively more vertical. However, trends of the motion are lost when increasing Reynolds number beyond 49000 and the elliptic trajectories appear random. This behavior is linked to the change of the shape of Vortex Street and the shedding pattern.

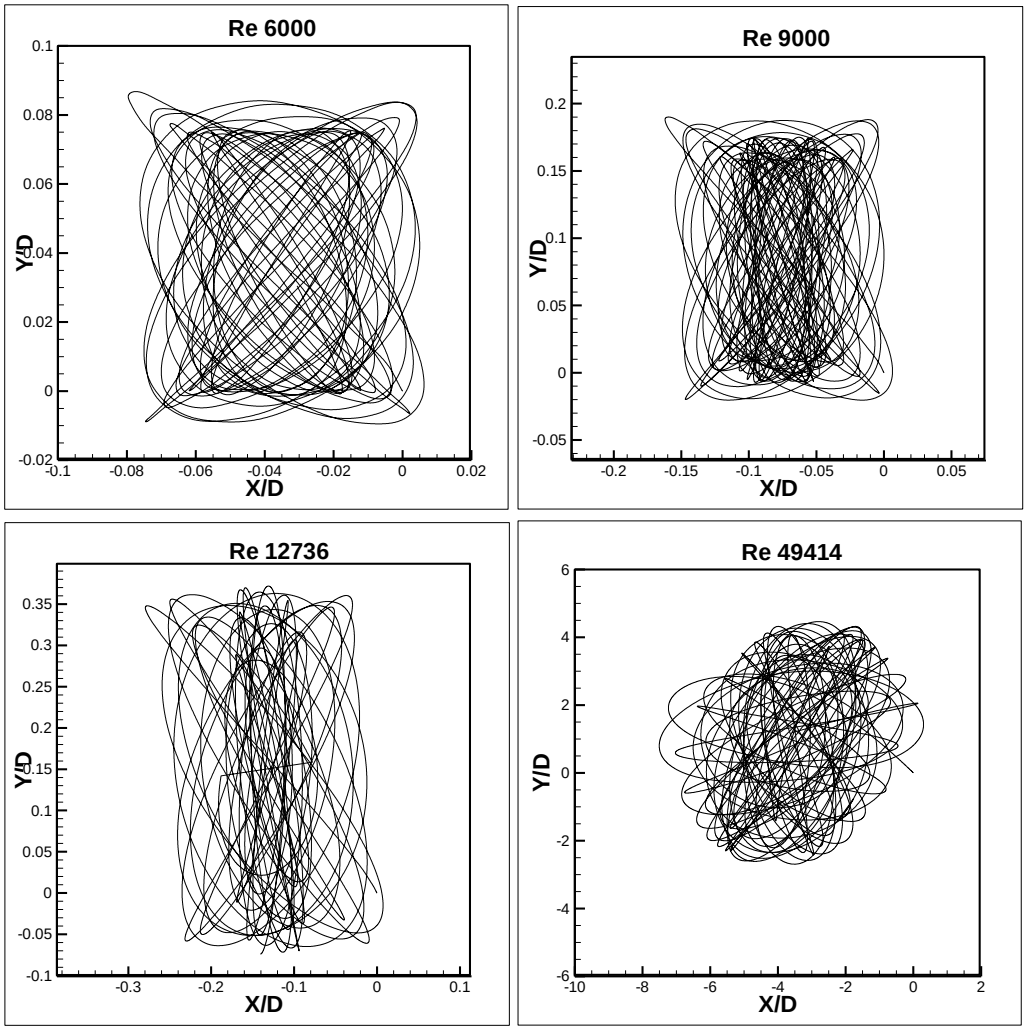

Figure 3-17: Centre of mass displacement (galloping ellipses) for different Reynolds numbers; axis scales are different for each case

3.4 Effect of Ice Shape, Wind Speed, and Wake on Galloping

In order to study the effect of the ice shape on the galloping of conductors, three cases of bare, thin smooth (glaze), and thick rough (rime) iced conductors are considered [10, 11]. In the case of thin ice, the predefined ice profile is a crescent shape with maximum thickness of 10% of the bare conductor diameter (D) at peak, and for thick ice, the profile is irregular with 30% of the diameter thickness at maximum (Figure 3-18). Moreover, to study the wake-induced vibrations at the same time, two conductors with similar profile and initial conditions are placed with typical bundle spacing of 14D. The initial angle of attack of the incident wind on the iced conductors is 30 degrees, which represents the initial ice accretion angle. The velocity range of 10-40 m/s is considered in order to study the effect of wind speed on the structural response of the conductors with horizontal, vertical, and torsional (rotational) degrees-of-freedom. The structural parameters are similar to the test case mentioned in the previous section.

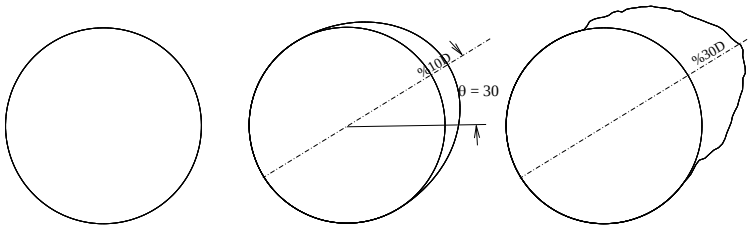

Figure 3-18: Bare conductor (no ice), glaze, and rime ice profiles

Figure 3-19 shows the response of the bare conductors at free-stream velocities of 10 and 40 m/s. The horizontal displacement of the windward conductor starts with large initial amplitude but is quickly damped. The initial amplitude in the horizontal direction increases with free-stream velocity, and, in all test cases, the oscillations decay around the final settlement point. The same observation is made

for conductors in the wake apart from the amplitude of the initial displacement, which is smaller than that of the windward conductors. Moreover, the damping rate is lower for conductors in the wake. The vertical and torsional displacements are negligible for windward conductors, and increasing the velocity has only small effects on the amplitude of these oscillations, while the vertical and torsional oscillations of the leeward conductors are slightly larger at higher velocities. However, the amplitudes of these oscillations remain small all the time compared to the horizontal displacements. Because of the symmetric shape of the bare conductors, the only source of the moment is the shear stress over the surface, and in this regime of the flow, the shear stress is small. Hence, small torsional amplitudes are predictable. An interesting observation is the direct relation between the amplitude of the torsional and vertical displacements. In Figure 3-20, the displacements of the center of mass (galloping ellipse) at various free-stream velocities are plotted. At all velocities and for both conductors, the galloping ellipses are horizontal, representing negligible vertical displacements. Thus, in the bare (no-ice) condition, the likelihood of vertical galloping is negligible as expected.

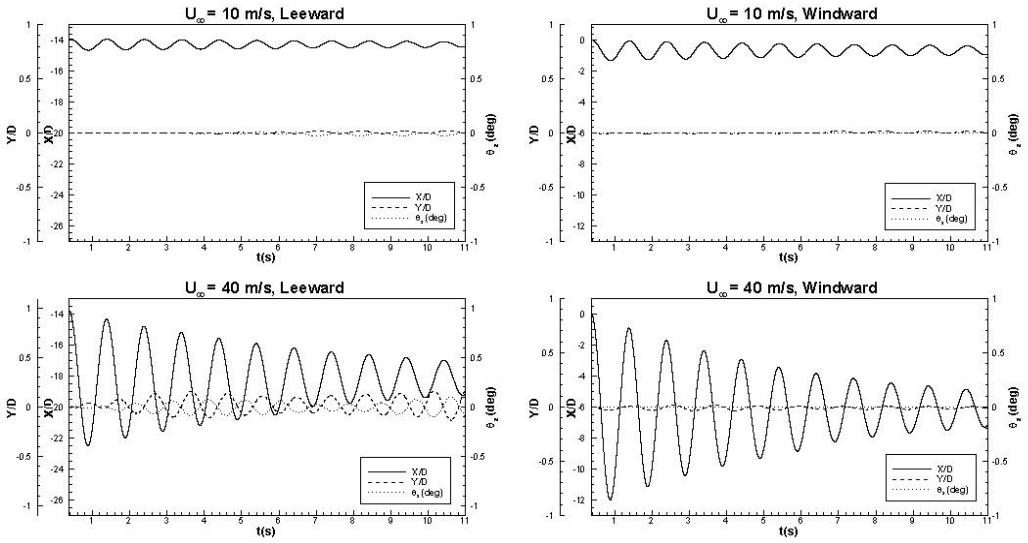

Figure 3-19. Time history of displacements of bare conductors

Figure 3-21 illustrates the vorticity contours for the bare conductors at incident wind of 40 m/s. The shedding mode behind the windward conductor is close to 2S while the leeward conductor, which is placed in the wake of the other conductor, experiences the 2P mode. As the vertical displacements of the conductors are quite small, the shedding mode does not change through time. Also, investigation of the vortex patterns at lower velocities shows minor differences in the shedding modes, although, the frequency of the shedding increases with velocity. Different shedding patterns lead to varying inflow, both in direction and magnitude, and variable loading over the conductor in the wake. Hence, this shows that applying the wind tunnel test results with the quasi-steady flow assumption can lead to inaccurate results for wind/wake-induced vibrations.

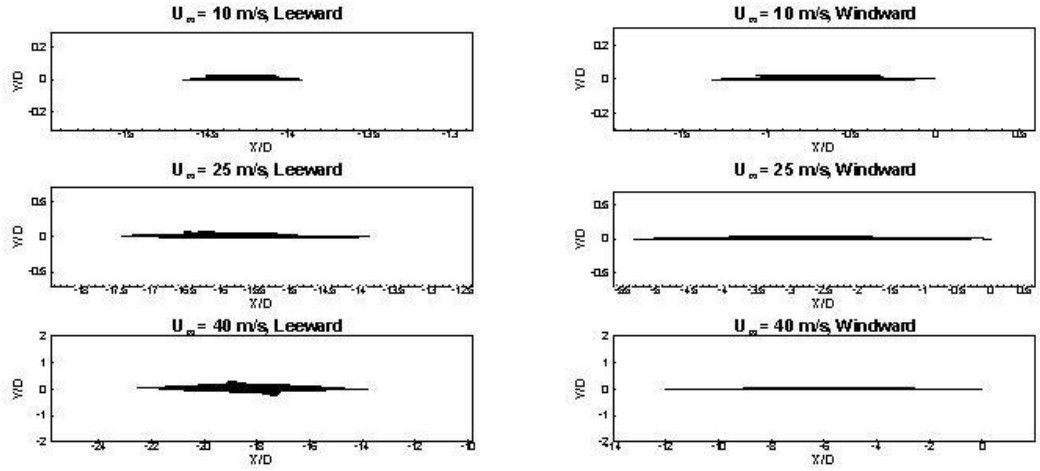

Figure 3-20: Centre of mass displacement (galloping ellipse) of bare conductors

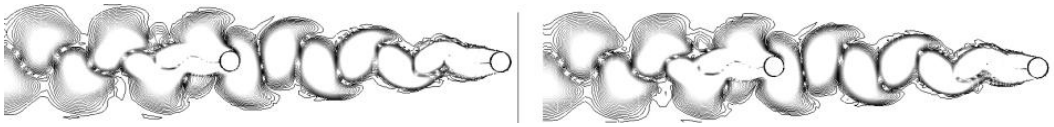

Figure 3-21: Vorticity contours for bare conductors at various positions

The oscillations of the glaze-iced conductors at free-stream velocities of 10 and 40 m/s are presented in Figure 3-22. Similar to the bare conductors, the horizontal displacements start with large initial amplitude and increase with free-stream velocity. The maximum amplitude of the horizontal oscillation in this case is in the same order of the bare case; however, the damping behavior is different. At low velocities the horizontal oscillations are of regular shape and get damped with the same rate as the bare conductors; however, at higher velocities oscillations beat with an irregular pattern and amplitude. The horizontal amplitude of the leeward conductor motion is smaller than that of the windward one, and its beating response is quite different. Close investigation of the vertical and torsional displacements shows that unlike the bare conductors, these oscillations are considerable. At 10 m/s, the vertical displacements reach 0.2D at peak for both windward and leeward conductors, while the torsional amplitude is around 0.5

degrees. The vertical and torsional displacements are sustained at low velocities. By increasing the velocity, the response and amplitude change dramatically. At 40 m/s, the vertical amplitude increases through time and just within 10 seconds reaches the 9.5D and 12.5D for the windward and leeward conductors, respectively. Similar to the no-ice case, the conductor in the wake experiences larger vertical displacement than the windward conductor. The torsional amplitudes of the windward and leeward conductors at 40 m/s reach 7 and 9 degrees, respectively. The windward torsion damps slowly, while the torsional motion amplitude of the leeward conductor increases. This observation illustrates the relation between the torsional and vertical displacements. The larger vertical and torsional amplitudes for the leeward conductors are related to the wake effects and higher inflow fluctuations that in-the-wake objects experience.

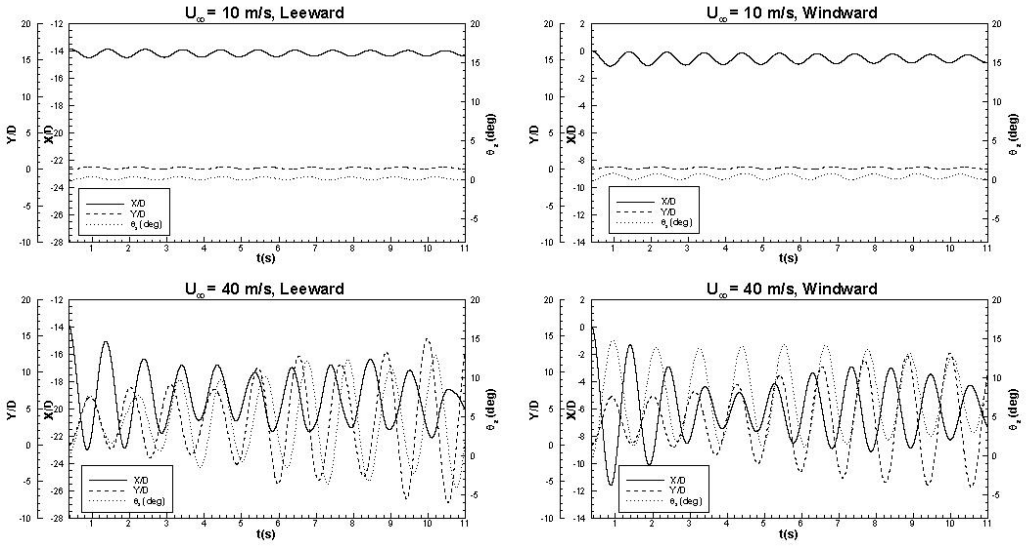

Figure 3-22: Time history of displacements of glaze iced conductors

In Figure 3-23, galloping ellipses at various velocities are plotted for the glaze iced conductors. At low velocities, the horizontal displacements are slightly

smaller than the vertical, making the galloping ellipse reclined horizontally; however, by increasing the velocity, the magnitude of the vertical displacements becomes much larger which makes the ellipses vertical.

Figure 3-24 shows the vorticity contours for the glaze iced conductors at 40 m/s. The shedding mode for both conductors is similar; however, the structure and width of the vortices in the wake change with the amplitude of the vertical and torsional motions. This phenomenon creates a completely different loading experience for the conductor in the wake. Moreover, as the structural response is a hysteresis, neglecting the wake effect in non-FSI computations can lead to inaccurate results.

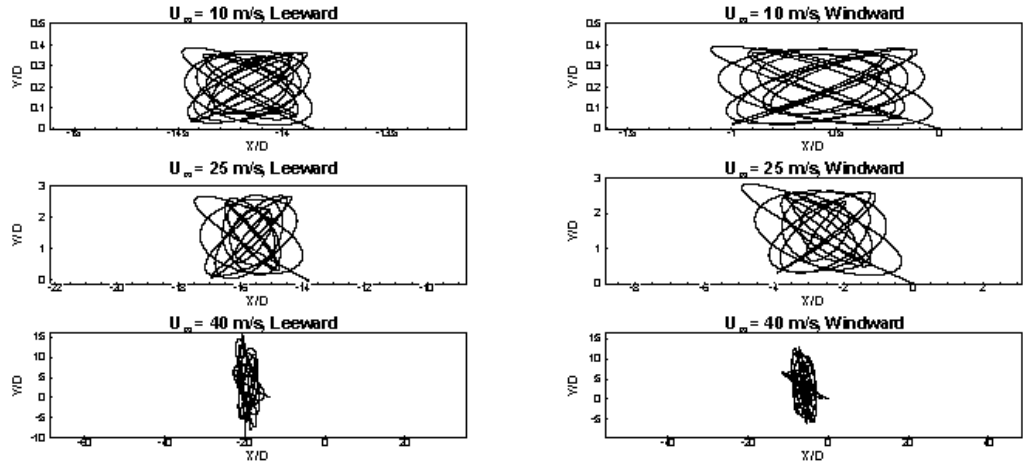

Figure 3-23: Centre of mass displacement (galloping ellipse) of glaze iced conductors

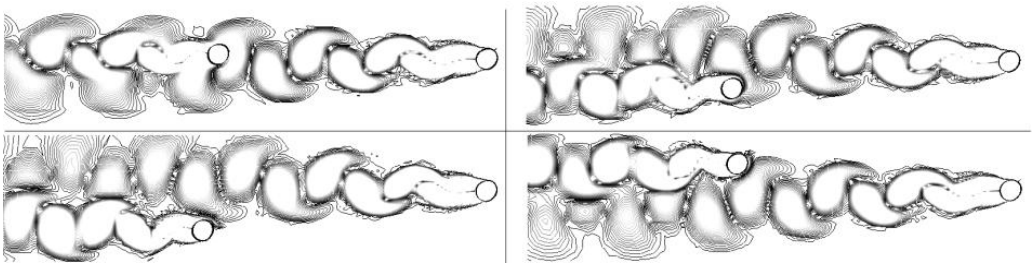

Figure 3-24: Vorticity contours for glaze iced conductors at various positions

Figure 3-25 shows the oscillations of the rime-iced conductors at free-stream velocities of 10 and 40 m/s. As shown, at low velocity, the structural response of the conductors is similar to the bare and glaze iced cases, but with higher amplitudes. At 10 m/s, the horizontal, vertical, and torsional displacements are periodic. The horizontal displacements of both conductors damp around the static settlement point; however, the torsional and vertical displacements persist with limited amplitudes. By increasing the free-stream velocity, the amplitude of the horizontal displacement raises and the response becomes chaotic. For instance, at 40 m/s, the initial horizontal displacements of the windward and leeward conductors become 15D and 8D, respectively. Investigation of the vertical and torsional displacements shows that in 6 s the vertical amplitudes of the windward and leeward conductors reach 28D and 23D, respectively, with peak-to-peak values of 56D and 46D, and the torsional amplitudes reach 13 degrees for both conductors. These displacements keep increasing through time until they reach a prescribed maximum horizontal amplitude (i.e. the conductors are prevented from passing each other in the horizontal direction, a situation that may happen at higher velocities in the rime loading case) after which the computations are stopped. It should be noted that the vertical amplitude of the bare and glaze ice cases at the same instance (6 s) are 0.2D and 8D, respectively; therefore, the conductors with 30% rime ice are more susceptible to galloping than the glaze iced conductors.

The galloping ellipses for the rime-iced conductors are illustrated in Figure 3-26. At low velocities, the galloping ellipses of the windward conductor are

horizontal, while those of the conductors in the wake are vertical. Similar to the glaze ice case, by increasing the velocity, the vertical oscillations become larger than the horizontal displacements, thus the galloping ellipses become vertical.

In Figure 3-27, the vorticity contours of the rime-iced conductors at 40 m/s are plotted at various positions. The Vortex Street structure and strength of the vortices depend on the relative structural displacements (along the 3 degrees of freedom) of the conductors. As the structural displacements in the vertical and torsional directions are very large, especially at higher velocities, the unsteady flow field in the wake of the windward conductor becomes complicated. Hence the loading experience and response of the two conductors are quite different. In such a case, using a quasi-steady based method will become even more inaccurate than for previous test cases.

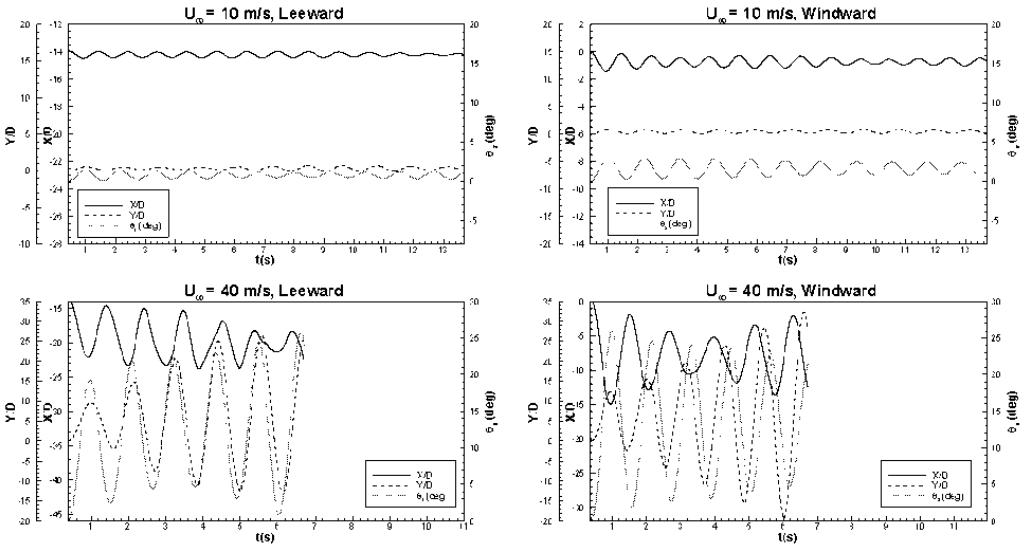

Figure 3-25: Time history of displacements of rime iced conductors

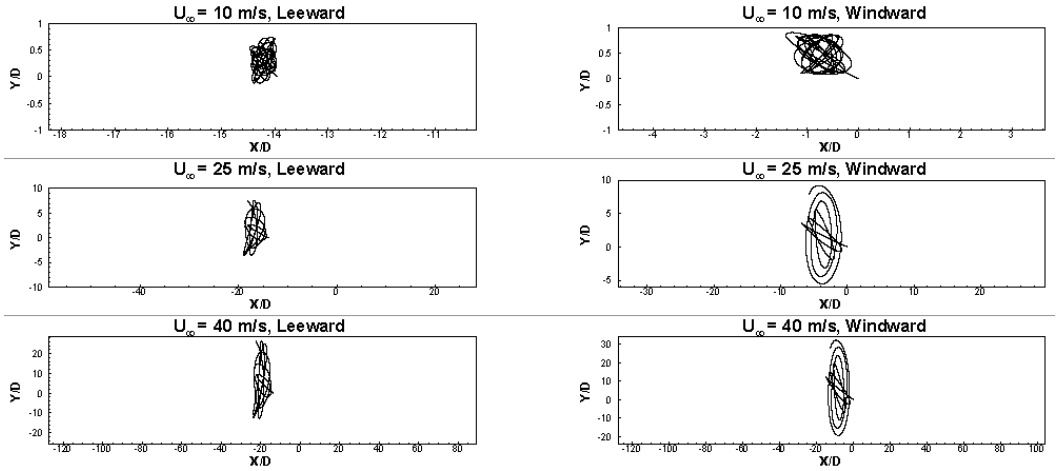

Figure 3-26: Centre of mass displacement (galloping ellipse) of rime iced conductors

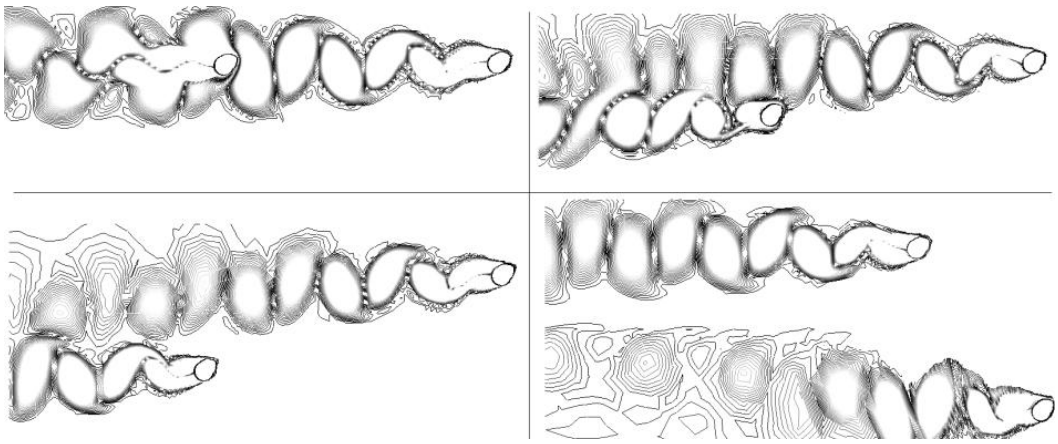

Figure 3-27: Vorticity contours for rime-iced conductors at various positions

3.5 Influence of Ice Location

The orientation of the ice deposit with respect to the incident wind, the iced conductor profile, and the magnitude of the incident wind velocity are combined parameters that influence the likelihood of galloping, although it is difficult to assign a confidence level to such predictions. In this section, the effects of the ice orientation and magnitude of the incident wind velocity on overhead conductor galloping are studied.

In order to study the effect of the initial ice deposit orientation with respect to incident wind flow on conductor galloping, a symmetric glaze iced conductor with maximum ice thickness of 37% of the conductor diameter is considered at different initial orientations (φ) relative to the incident wind. Figure 3-28 illustrates the geometry of the model, the flow boundary conditions, while the top right insert shows the profile of the iced conductor and defines the angle φ. The incident wind velocity range of 10-30 m/s is considered. The natural frequencies of translational galloping oscillations of the iced conductor on flexible supports, representing the mid span oscillations of a typical high voltage line conductor, are 0.995 Hz and 0.845 Hz in the horizontal and vertical directions, respectively, and the rotational frequency is twice the vertical frequency. The iced conductor mass, moment of inertia, and stiffness are chosen in such a way to match these conditions. Structural damping is typically very small (up to 0.5% of critical damping for vertical motions, and up to 2% for rotation), and assigning accurate values is a difficult task; however, structural damping cannot be neglected at low frequencies such as in the present study. On the basis of wind tunnel experiments and previous studies [1, 10, 65], the structural viscous damping ratio is set to 0.08% for horizontal and vertical motions and 1.5% for rotation. It should be emphasized that as the results will be compared against Den-Hartog's instability criterion, the 1.5% is chosen for rotational damping ratio in order to weaken the effect of rotation on the amplitude of transverse oscillations.

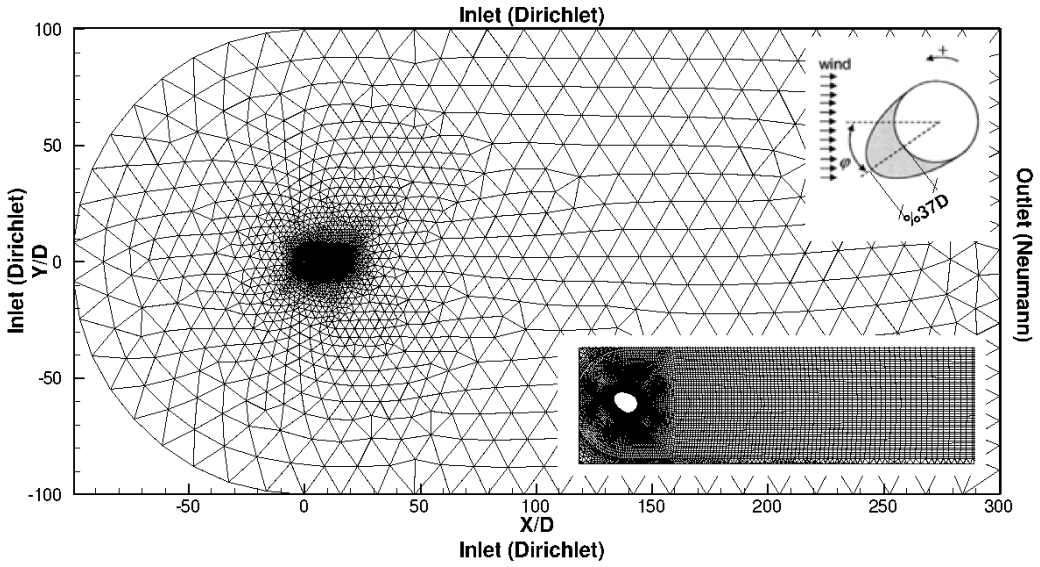

Figure 3-28: Computational mesh, boundaries, and ice profile

3.5.1 Den-Hartog instability zone

In order to numerically investigate the Den-Hartog criterion for the studied iced conductor profile, the unsteady flow field around the profile at various orientations is solved and the unsteady loading over the body is computed. The calculations are continued until the vortex patterns behind the body are fully developed and then the time averaged aerodynamic coefficients are calculated. In Figure 3-29, the computed time-averaged aerodynamic coefficients of the non-moving (fixed) iced conductor versus the initial ice deposit orientation are plotted; the derivative of the lift coefficient is also included in the figure. Based on Den-Hartog's galloping criterion, the iced conductor is subject to instability only at a very small area around 180^{o} (see Figure 3-29), which confirms that this criterion, due to its simplicity, can only describe a small portion of the instability domain and is a poor predictor of instability limits of a multi-degree-of-freedom system.

In other words, there might be other instability conditions outside of the Den-Hartog's instability zone (see §3.5.2 for more evidences).

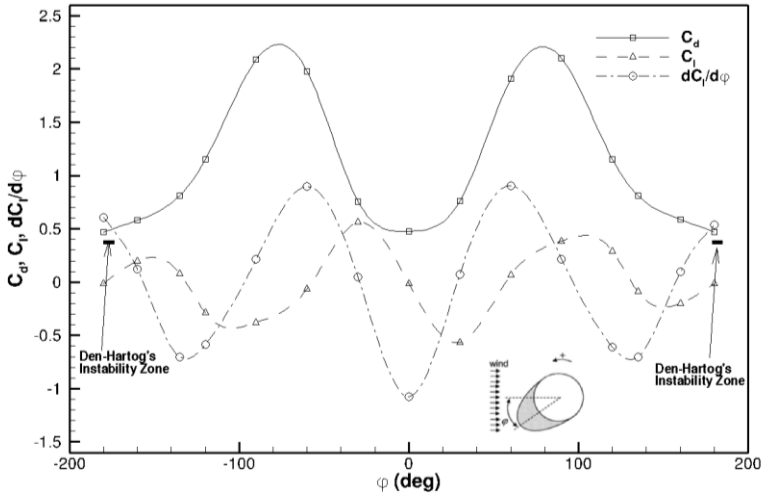

Figure 3-29: Computational time-averaged aerodynamic coefficients versus ice deposit orientation

3.5.2 Aeroelastic instability zone

In the case of heavily separated flow over bluff bodies, such as the present case, the unsteady loading and aerodynamic damping are functions of both the incident velocity (or more precisely Reynolds number) and the profile of the bluff body. By means of the computational aeroelastic approach, these effects are included in the study; therefore, predicting instabilities can be more accurate. In Figure 3-30, displacement trajectories of the center of mass (galloping ellipses) of the iced conductor at incident velocity of 10 m/s are plotted. At $\varphi = 0$, the amplitude of oscillations is very small and the galloping ellipse is horizontal. By increasing $|\varphi|$ φ, the oscillations become larger and the galloping ellipses stretch in the vertical direction. As shown in the figure, the vertical displacements reach their maximum value at $\varphi = \pm 30°$, which coincides with the maximum time-averaged lift

coefficient (see Figure 3-29). By further increasing φ, the time-averaged lift coefficient decreases and drag increases. Hence, the amplitude of vertical displacements decreases very fast and the horizontal amplitude increases; as shown in the figure; at $\varphi = 60°$, the galloping ellipses stretch horizontally. The maximum horizontal displacement occurs at $90°$, which coincides with the maximum drag coefficient. As φ is further increased, the time-averaged lift coefficient grows to a second peak while the drag decreases; therefore, the galloping ellipses shrink horizontally and stretch vertically to a local maximum at around $120°$; however, the amplitude of vertical displacements in this case is smaller than the amplitude predicted for $\varphi = \pm 30°$. Finally as φ reaches $180°$, all displacements are greatly reduced. As indicated by the galloping ellipses, all displacements for all initial orientations diminish through time; this means that the iced profile is immune to large galloping displacements at incident wind velocity of 10 m/s.

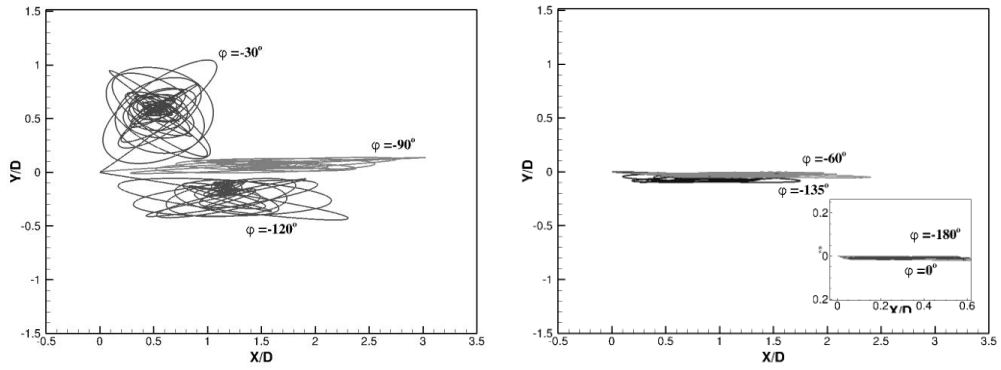

Figure 3-30: Center of mass motion at various initial iced profile orientations with respect to incident wind velocity of 10 m/s

The same study is performed for incident wind velocities of 20 m/s and 30 m/s. Figure 3-31 shows the galloping ellipses for several ice deposit orientations at

incident wind velocity of 20 m/s. As the first observation, one can see that the amplitude of translational vibrations in both directions increases with wind velocity. Moreover, it can be seen that the general trend of the structural response is more or less similar to that of the 10 m/s case except at $\varphi = \pm 60°$ where the large displacements increase and reach a limit cycle (see also Figure 3-34). This indicates that for $\varphi = \pm 60°$, the aerodynamic damping is negative and its magnitude is larger than the value of structural damping assigned in the model. The instability of this particular iced profile orientation is not predicted by Den-Hartog's criterion.

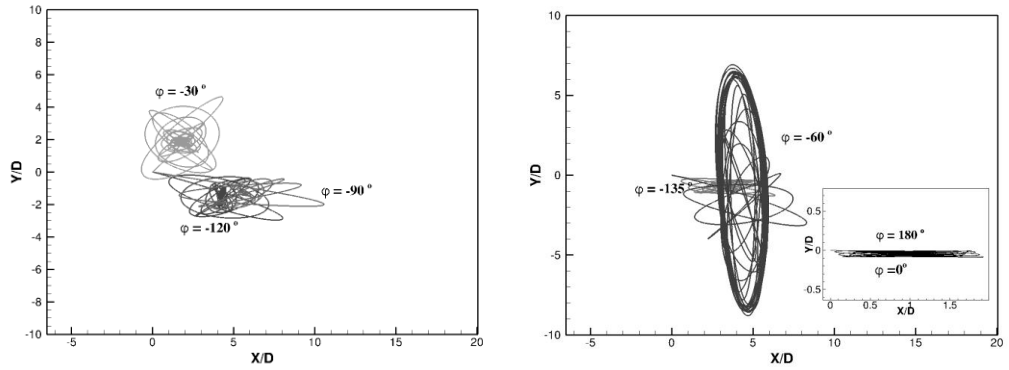

Figure 3-31: Center of mass motion at various initial iced profile orientations with respect to incident wind velocity of 20 m/s

In Figure 3-32, the galloping ellipses for several ice deposit orientations for incident wind velocity of 30 m/s are shown. Similar to the 20 m/s case, the amplitude of the translational vibrations in both directions increases with incident wind velocity which shows the velocity-dependency of the displacements; however, the structural response is significantly different from the previous two cases and more unstable regions are present. As shown in the figure, the oscillations at different initial ice orientations damp quickly except for the

following regions: $\varphi = \pm 30, \pm 60, 180^{\circ}$. This shows that the negative aerodynamic damping at these regions prevails the structural damping, increasing the likelihood of large amplitude instabilities. At $\varphi = \pm 30^{\circ}$, as illustrated by the vertically reclined ellipse in Figure 3-32, the horizontal oscillations decrease rapidly; however, the vertical displacements increase and reach a limit cycle with the highest peak-to-peak amplitude among all other test cases. This response is quite different from the lower incident wind velocities. In the case of $\varphi = \pm 60^{\circ}$, the oscillations are similar to the 20 m/s; i.e. the oscillations reach a limit cycle in which the peak-to-peak horizontal amplitude at limit cycle is the highest among other orientations. Finally, at $\varphi = 180^{\circ}$, the horizontal oscillations damp quickly, while the vertical displacements increase with a very small rate. The small amplitude increase rate is due to zero time-averaged lift coefficients (see Figure 3-29). Therefore, the instability for $\varphi = 180^{\circ}$ can be type of vortex-induced vibrations in which the oscillations are caused due to load fluctuations, and the amplitude at limit cycle is expected to be in the order of the conductor diameter. It should be noted that although the aeroelastic computations are accomplished for a same amount of physical time for all test cases, only in the latter case, the vertical oscillations are not reached a limit cycle. This response and the slow pace of the instability can be seen well at the relevant phase plot in Figure 3-33.

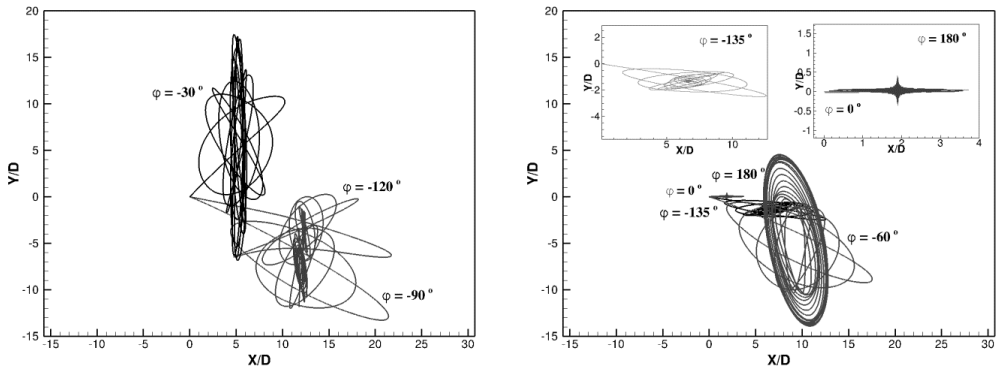

Figure 3-32: Center of mass motion at various initial iced profile orientations with respect to incident wind velocity of 30 m/s

Phase plots, rate of change of a variable versus the variable itself, are practical illustrations to study response of a system and analyze the instabilities and determine any potential limit cycles. In the following figures, the phase plots of the transverse displacements, i.e. the transverse velocity of the oscillations versus the transverse displacements are provided at select ice orientations for 20 m/s and 30 m/s incident wind velocities. Figure 3-33 represents the phase plots for transverse displacements at $\varphi = 180^{\circ}$. As shown, the amplitude of the oscillations increases gradually for 30 m/s, yet there is no stable limit cycle for the duration of the computations. However, for 20 m/s, the phase plot shows that the oscillations slow down and the amplitude of the displacements decrease rapidly. The phase plots for $\varphi = -60^{\circ}$ (Figure 3-34) confirm one stable limit cycle for both incident wind velocities. By investigating phase plots at $\varphi = -30^{\circ}$, see Figure 3-35, we can see that at 20 m/s the oscillations damp out very fast, while at 30 m/s, displacements converge to a large amplitude limit cycle.

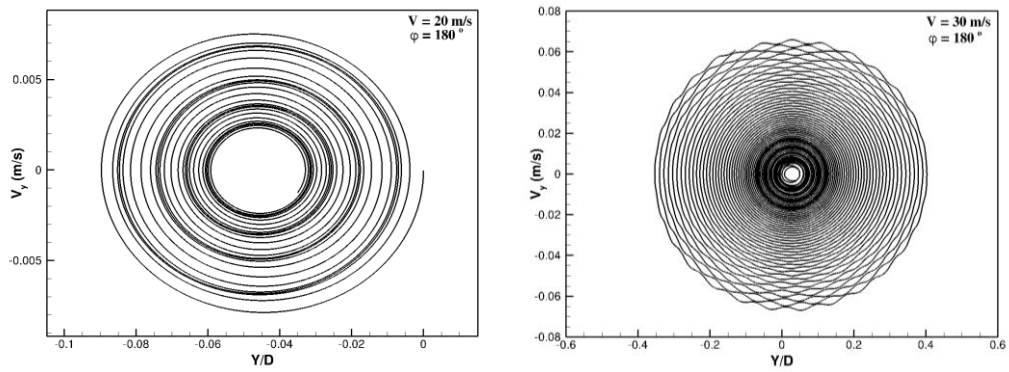

Figure 3-33: Phase plot of transverse displacements at $\varphi = 180^{\circ}$ for incident wind velocities of 20 m/s and 30 m/s

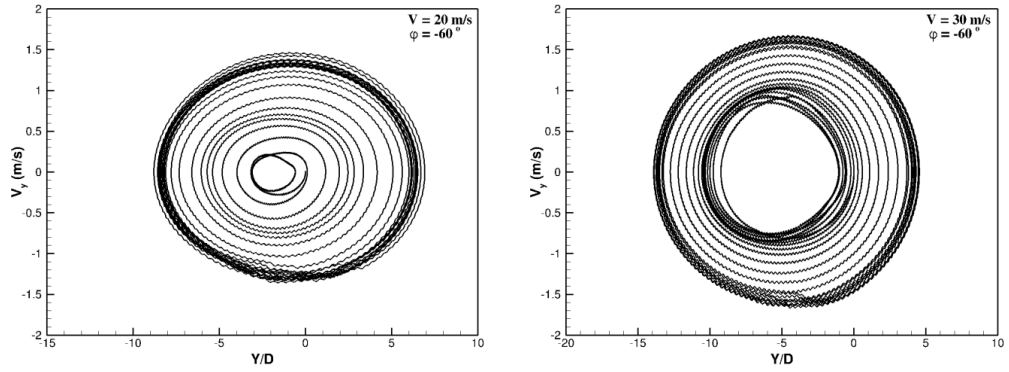

Figure 3-34: Phase plot of transverse displacements at $\varphi = -60^{\circ}$ for incident wind velocities of 20 m/s and 30 m/s

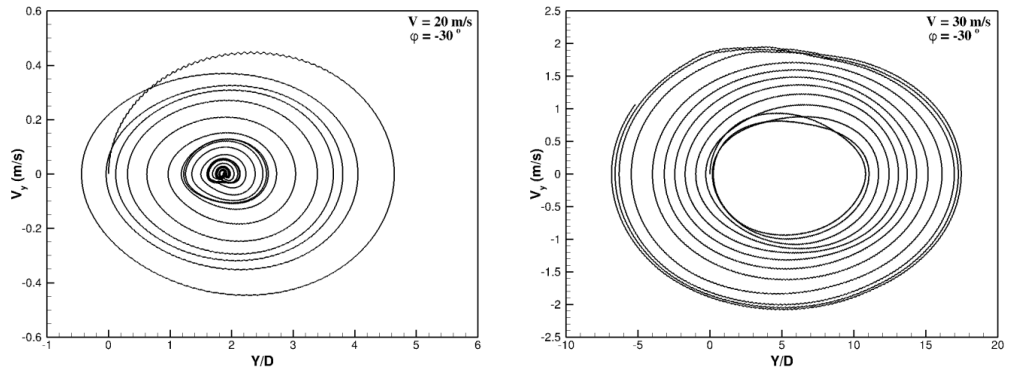

Figure 3-35: Phase plot of transverse displacements at $\varphi = -30^{\circ}$ for incident wind velocities of 20 m/s and 30 m/s

3.6 Three-Dimensional Galloping

In this section, three dimensional test cases are covered. A single conductor with predefined ice profile of a three-span transmission line is studied. For this line, a field galloping record and numerical simulation based on quasi-steady assumption are available for the sake of comparison.

3.6.1 Single conductor of three-span transmission line

A three-span single-conductor line with cable elements is simulated with physical parameters outlined in Table 3-4. This test case is chosen based on an available field test and numerical studies in the literature [23]. Wind blows with speed of 4.1 m/s over the line with constant D-shaped profile adapted uniformly on the conductor (see Figure 3-36), and its initial orientation with respect to the horizon is 10 degrees. Each span consists of 10 cable elements (30 elements in total). The CFD analysis is performed over 30 sections using 120 CPUs (4 CPUs per section) for 15 days.

Table 3-4: Physical parameters of line #1

Parameter	Notation	Value	Unit
Axial rigidity	AE	13.3	10^6 N
Axial-torsional coupling	B_T	0	N m rad^{-1}
Torsional rigidity	GJ	101	N m^2 rad^{-1}
Horizontal tension	H_h	21.73	10^3 N
Span	L_h	125.9	m
Remote span stiffness	K_{ST}	76.21	10^3 N m^{-1}
Insulator horizontal stiffness	K_{Ix}	1017	N m^{-1}
Insulator swing stiffness	K_{Iz}	1362	N m^{-1}
Length of insulator	L_I	2.1	m
Weight of insulator	W_I	490	N
Damping ratio	ξ	0.02	10^{-2}
Target frequency to damp	f	0.474	Hz
Bare conductors diameter	d	18.8	10^{-3}m
Mass per unit length	μ	1.53	kg m^{-1}
Mass moment of inertia	I	57.02	10^{-4} kg m^2 m^{-1}
First moment of area (y-dir)	S_y	0.459	10^{-3} kg m m^{-1}
First moment of area (z-dir)	S_z	-0.145	10^{-3} kg m m^{-1}

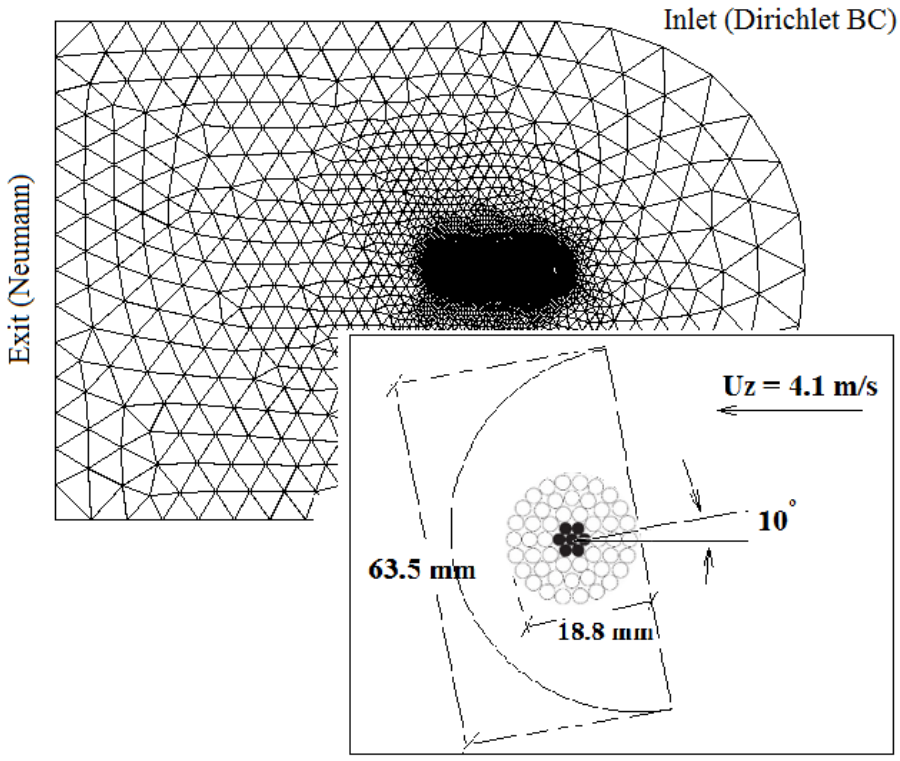

Figure 3-36: 2D cut of the computational fluid grid and D-shaped ice profile

The unsteady time accurate flow solutions are computed at each time step for all sections. In Figure 3-37, the instantaneous turbulent viscosity is shown, and in Figure 3-38, the streamlines are plotted at simulated time of 31 s. As shown, details of the flow are adequately captured by simulation; the near vortices behind the cylinder, the circulation zone, stagnation and separation points, and other features of the flow are captured. Time accurate simulation of the flow is crucial in fluid-structure interaction (FSI) simulations as this is directly related to the time history of the fluid loading and the aerodynamic damping. This becomes more important for flows with inherent unsteadiness such as the current case of flow over the bluff body. Improper flow simulation can impose excessive positive artificial aerodynamic damping which can lead to unrealistic over-damping of displacements and consequent misleading predictions.

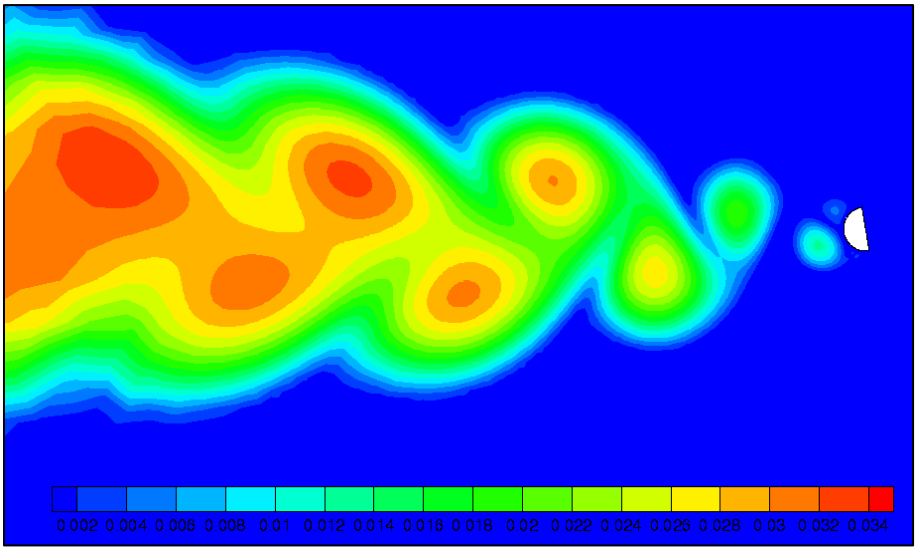

Figure 3-37: Instantaneous turbulent viscosity at mid-span

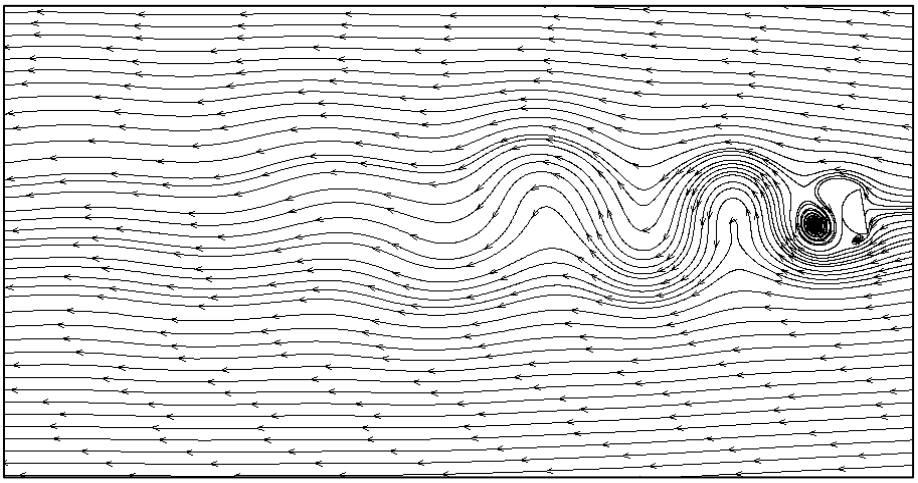

Figure 3-38: Instantaneous stream lines at mid-span

In Figure 3-39 to Figure 3-42, the snapshots of the conductor motions are plotted at different time steps from different perspectives. The velocity vectors (red vectors) at the direction of the displacements are superimposed to show the higher modes, and the resultant nodal forces are shown (blue vectors).

In order to visually investigate the behavior of the conductor through time, the most flexible point in the system is usually chosen. This point is the mid-span, which has the maximum initial sag with the minimum stiffness. In Figure 3-43,

the first 51 seconds of the vertical displacements at mid-span of the middle conductor is plotted, and in Figure 3-44, the horizontal and torsional displacements of the same node are illustrated. As shown, the horizontal displacements damp quickly while the vertical and torsional displacements start growing, and growth of vertical motions is with beating. It should be noted that the torsional motion plotted includes the rotation due to horizontal and vertical displacement of the conductor. This rotation becomes zero as horizontal displacements damp. As shown in the figures, the time histories of the torsional and vertical displacements change with a similar trend and very close frequency with almost zero phase difference. This behavior is well known in literature as vertical-torsional coupling and is corner stone of the galloping instability. This coupling is well shown numerically in Figure 3-45.

In order to better visualize behavior of the instabilities, investigating phase plots is useful. In a phase plot, displacement is plotted versus variation of the displacement (or simply velocity). In Figure 3-46, the phase plot of the vertical displacements is portrayed. The plot starts from origin (the rest initial condition) and expands in time. Two initial dark areas where multiple lines lay on each other show the unstable limit cycles and the initial beating behavior of the displacements. Further expansion of the phase plot confirms the tendency of the oscillations to amplify, and shows presence of the negative damping in the system (caused by both structural system and flow field). The imposed structural damping is always positive; hence, the aerodynamic damping should be negative

and larger in magnitude than structural damping to impose this instability. This negative damping is always required in the flow-induced instabilities.

In Figure 3-47, the phase plot of the horizontal displacements is depicted. This plot reveals presence of a very large horizontal damping in the system. The structural damping is very small; hence, the horizontal aerodynamic damping should be positive and large in magnitude. As the time averaged drag force is positive and amplitude of the variations of drag due to vortex shedding is much smaller than averaged drag, the instantaneous drag is positive all the time. Therefore, a large aerodynamic damping in horizontal direction is imposed over the system making all swinging displacements settle quickly. The galloping ellipse of the mid-span is shown in Figure 3-48. This shows the development of the vertical and horizontal displacements in single plot and shows the required clearance. The frequency of the vertical and torsional oscillations is in good agreement with field tests (see Table 3-5), and as mentioned above, a large-amplitude transverse oscillations is expected due to negative damping shown in the results; however, comparison of the amplitudes should be postponed until future simulations[1].

Table 3-5: Comparison of predicted and measured results at mid-span

	Plunge	Torsion	Galloping Ellipse
Current results	0.5609 Hz	0.5661 Hz	1.1°
Filed measure (from [23])	~ 0.51 Hz	~ 0.50 Hz	0.8°

[1] Due to multiple limitations including supercomputers limitations to run for a long enough time, continuing simulations for a longer time was not feasible.

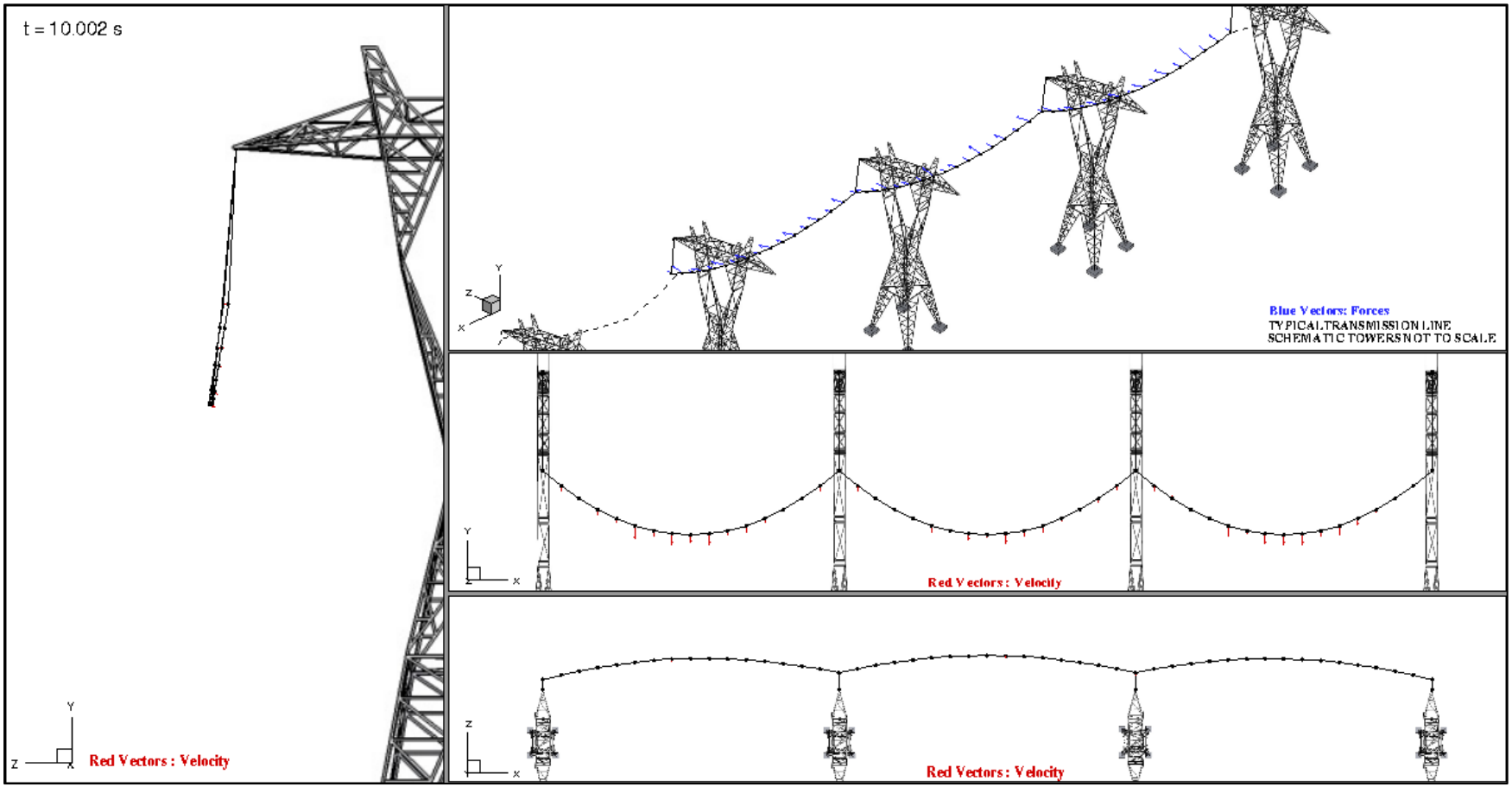

Figure 3-39: Snap-shot of the conductor motions, t =10.0 s

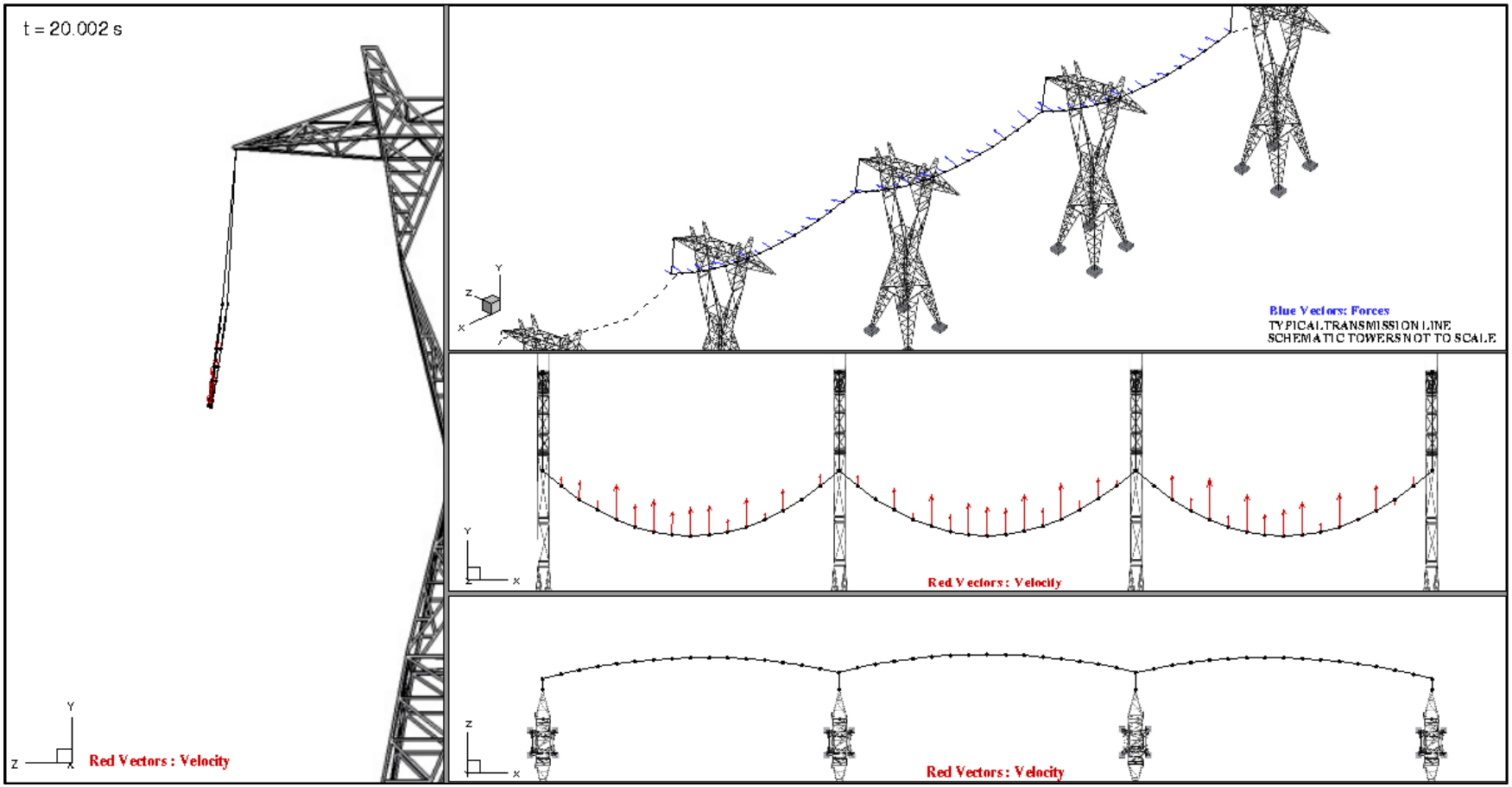

Figure 3-40: Snap-shot of the conductor motions, t =20.0 s

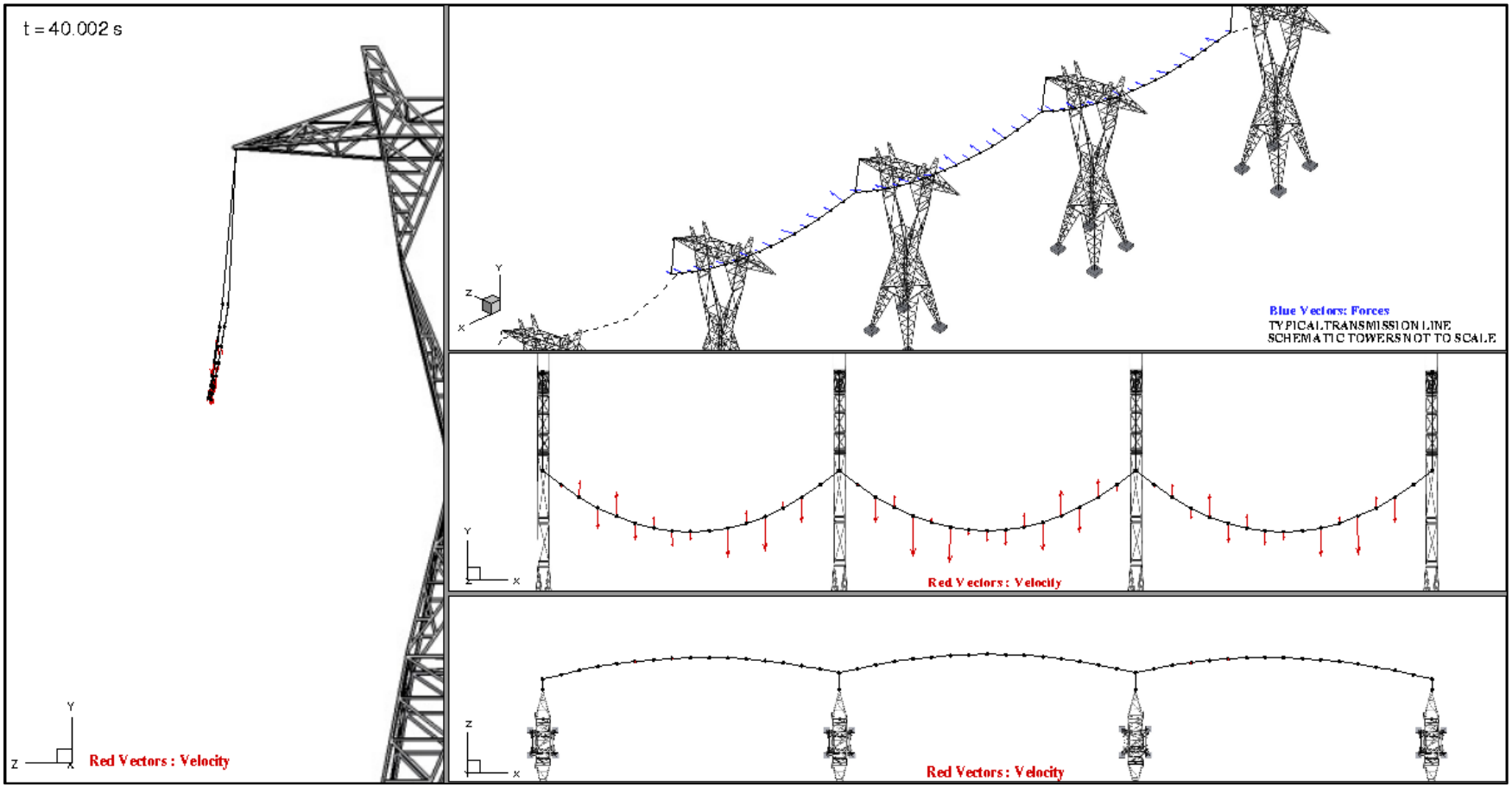

Figure 3-41: Snap-shot of the conductor motions, t =40.0 s

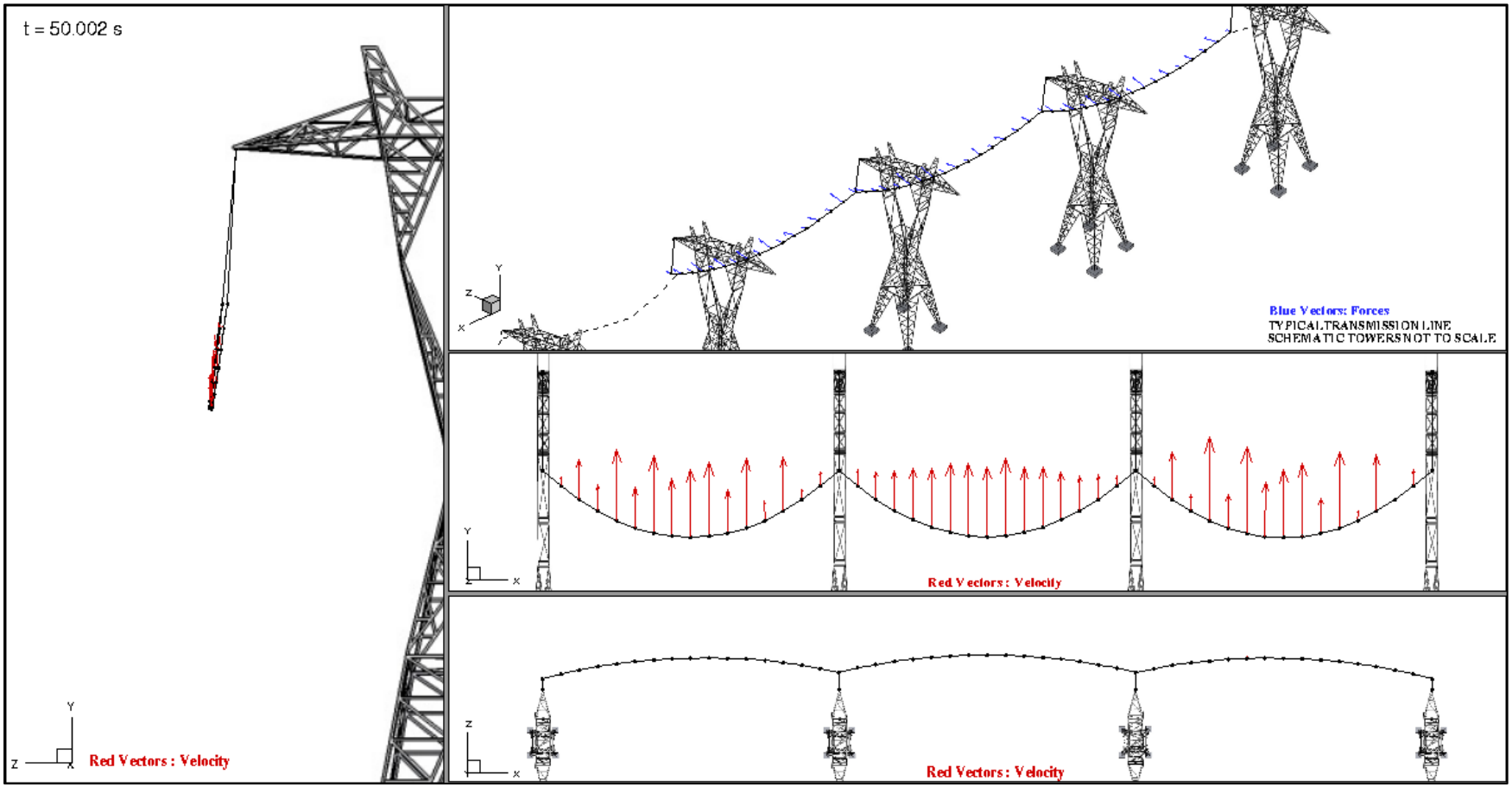

Figure 3-42: Snap-shot of the conductor motions, t =50.0 s

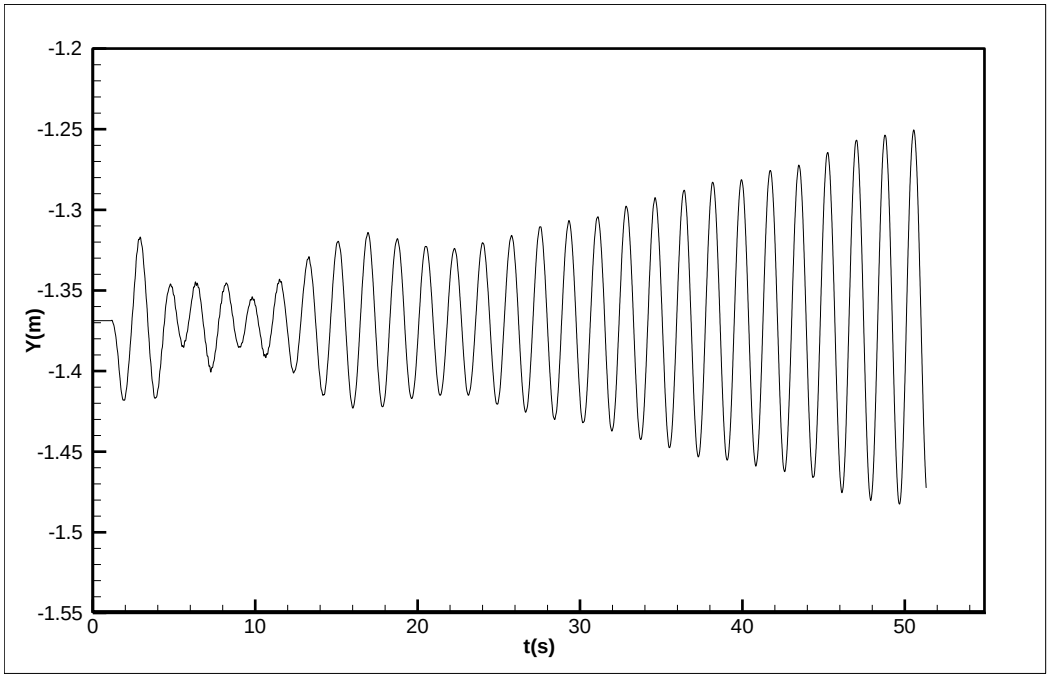

Figure 3-43: Mid-span vertical displacements

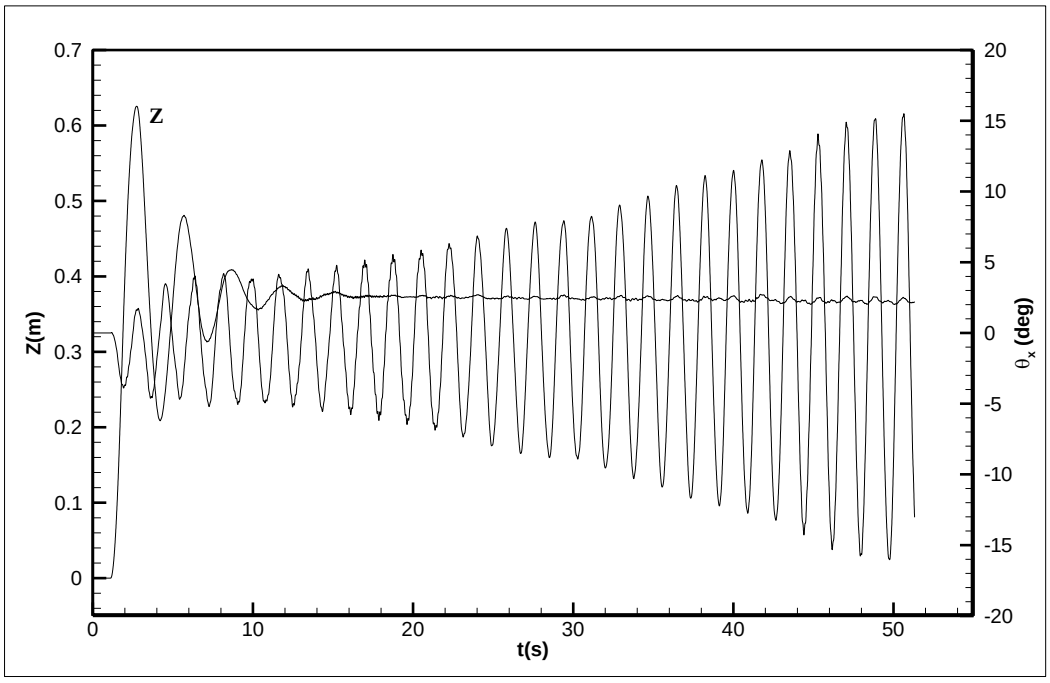

Figure 3-44: Mid-span horizontal and torsional displacements

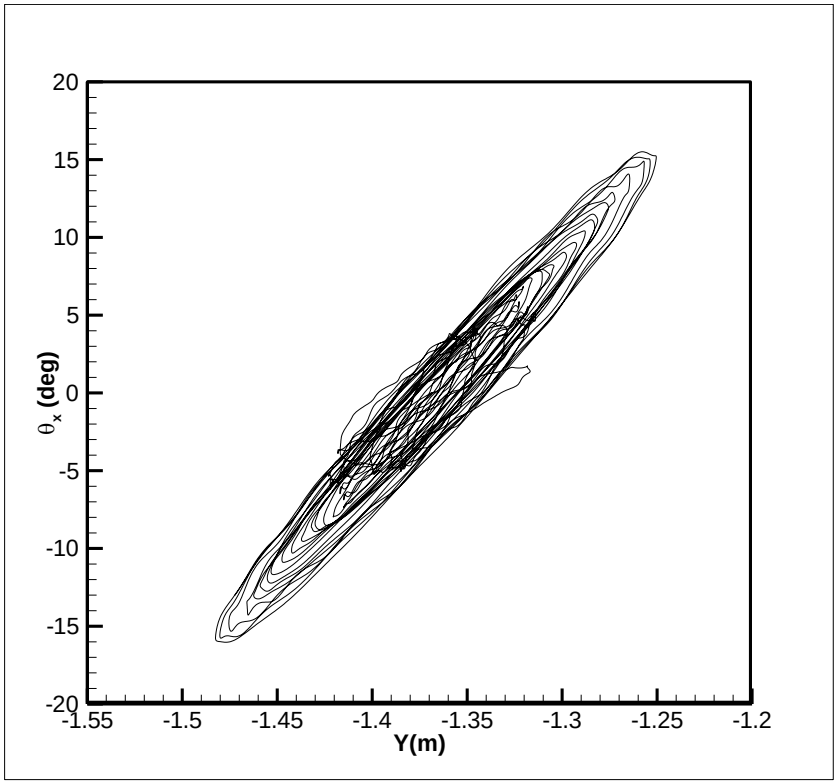

Figure 3-45: Torsional versus vertical displacement at mid-span (torsional-vertical coupling)

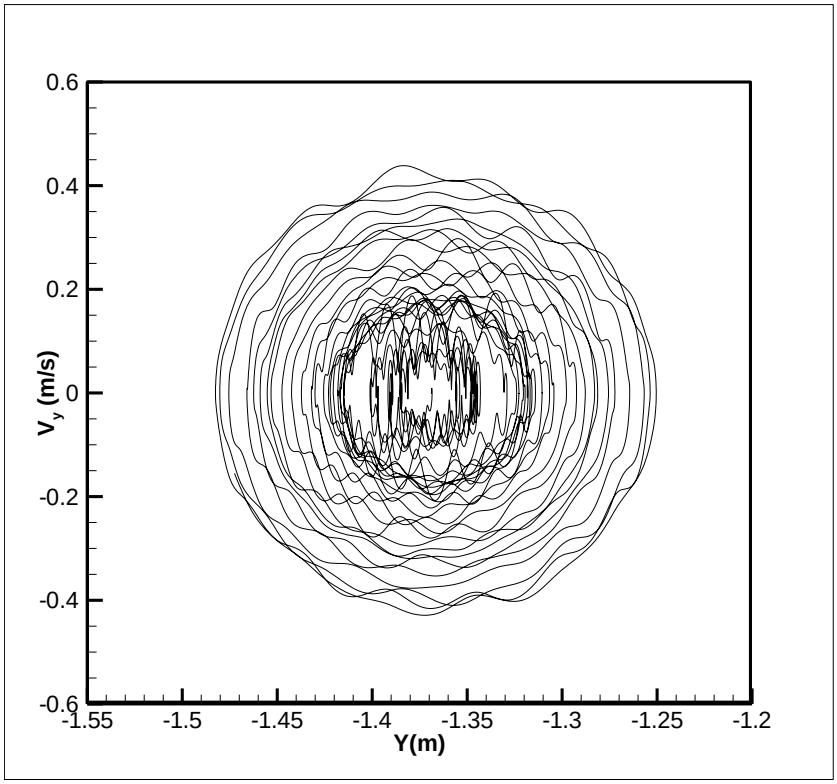

Figure 3-46: Mid-span phase plot of vertical displacements

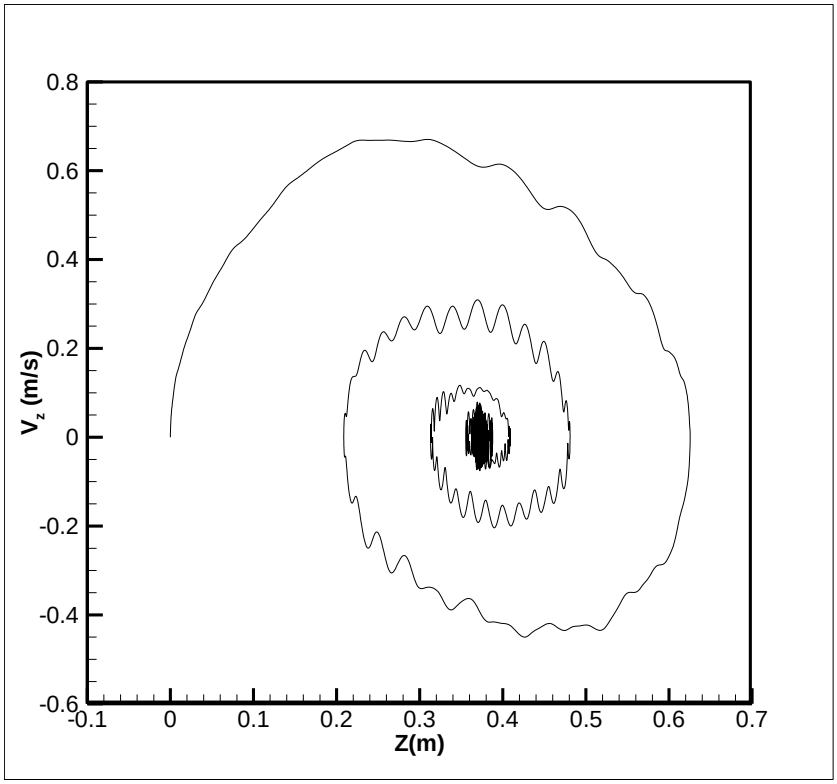

Figure 3-47: Mid-span phase plot of horizontal displacements

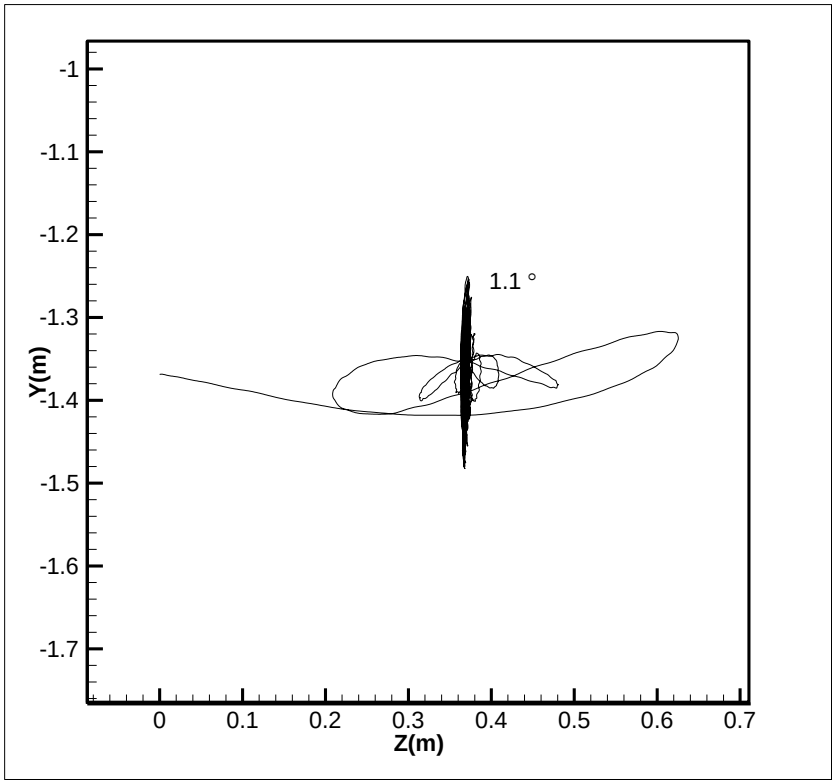

Figure 3-48: Mid-span galloping ellipse (center of mass displacement)

In Figure 3-49 and Figure 3-50 the time histories of the tension at mid-span and tower are shown respectively. Investigating these graphs discloses that the frequency of variations of tension is equal to the frequency of the vertical displacements. However, as expected, the tension and vertical displacements have 180 degrees of phase difference, i.e. maximum tension happens at the lowest vertical position of the mid-span. An interesting observation is the effect of unsteady swinging at unsteady tension of the tower (first-node), while in the mid-span this effect is not observed.

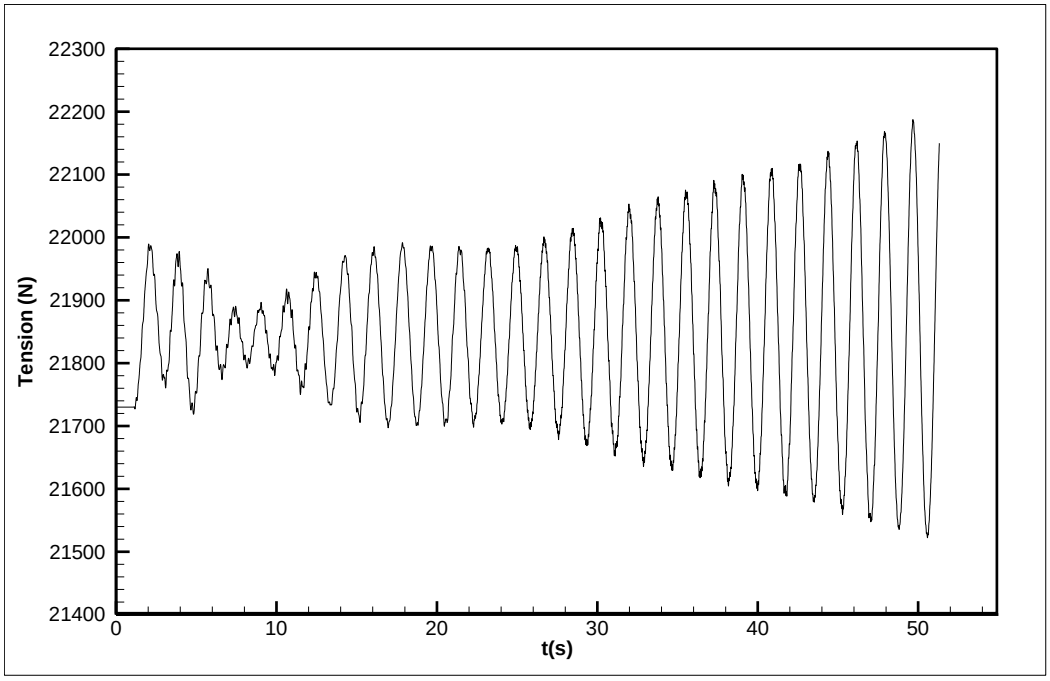

Figure 3-49: Mid-span tension history

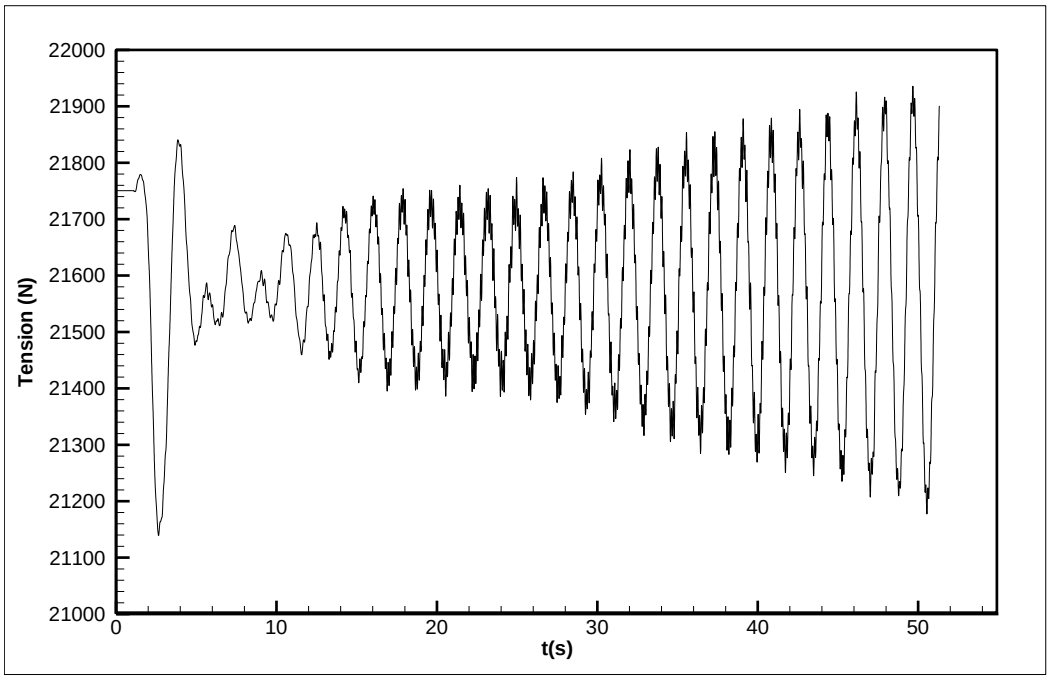

Figure 3-50: Tower-node tension history

CHAPTER 4: Concluding Remarks

In the following, the originality, summary of the results, and recommendations for future work are discussed.

4.1 Originality

In this research, an analytical framework is developed for the 3D computational simulation of cable galloping in a coupled fluid-structure interactive way. The present work offers much more realistic details of the true situation. These developments are embedded into a practical (manageable) fully computational aeroelastic tool to study wind-induced motions of conductors in 2D and 3D for single and bundled conductors. It is capable of simulating different kinds of instabilities including aeolian vibrations, vortex-induced vibrations, and galloping of any profile. It is also able to handle variable ice profiles throughout the span. The methodology developed is completely independent of the field test and wind tunnel measurement. The quasi-steady assumption, used in other studies, is also eliminated in the present work. Moreover, the effects of ice accretion, amount of ice, orientation and shape of ice on galloping are studied.

The developed tool is user-friendly and coupled with FENSAP-ICE (as the CFD solver). The approach is general enough to be applicable to the dynamics of tall buildings in CWE (see [68]). Finally, to the best of our knowledge, from open literature, this is the first code developed and successfully validated to study transmission line galloping instability, using only computational methods for both fluid and structure.

4.2 Conclusion

In this research, various types of transmission line instabilities are introduced and their impact on reliability and serviceability of electrical power networks are discussed. The galloping event is shown as an important design criterion. By following a historical background, different mechanisms to describe this event are investigated and benefits and drawbacks of each method are referenced. The developed methodology is a two-way loosely coupled fluid-structure interaction analysis consisting of three key modules: Computational Fluid Dynamics (CFD), Computational Structural Dynamics (CSD), and communication and data-handling modules.

Subsequent to successfully completion of preliminary standard validation tests of each fluid and solid solvers and transfer module individually, the transverse vortex-induced vibration of a circular cylinder with low mass-damping is studied as the first test case for compilation of the all modules. In the absence of Direct Navier-Stokes (DNS) and Large Eddy Simulation (LES) models, as these are computationally expensive particularly for unsteady cases, the present numerical methodology shows that URANS models can be efficiently used to predict the salient features of the flow around freely vibrating bluff bodies, including the near wake structure, the shedding modes, and unsteady loading. Moreover, the numerical results are compared with experiments and show very good agreement. More importantly, the numerical results of the vibrating cylinder show an encouraging improvement over the previous studies in capturing the upper branch of the response.

Then, the galloping oscillation of an iced profile for which an experimental benchmark test case is available is studied, and results are found in general agreement with the experiment. Instability of the profile at other incident velocities is also investigated. Moreover, the effect of incident velocity on the flow field, the aerodynamic loading, oscillations, and the galloping ellipses is examined.

The computational fluid-structure interaction of the windward and leeward conductors at velocity range of 10-40 m/s is studied next in three icing conditions. The structural response of the conductors, effect of incident wind velocity on horizontal, vertical, and torsional amplitudes of the conductors motion, orientation of the galloping ellipses, in-the-wake structural response, structure of the vortex street, relation between vertical and torsional displacements, and the effect of various conditions on the onset of galloping have been studied. The simulation results show that a small amount of ice accretion (in the order of 0.1 D) on conductors with a favorable free-stream velocity can lead to undamped large oscillations. Moreover, when the shape, surface roughness and amount of accreted ice modify the conductor profile in such a way that the aerodynamic loading amplifies considerably, such as the rime ice case in this study, the amplitude of displacements will increase through time and a galloping event will be likely. It is also shown that due to the complicated flow field around the objects in the wake, using methods based on the quasi-steady flow assumption and wind tunnel tests to predict galloping events can lead to inaccurate results.

Then, computational aeroelastic instability of an iced conductor with various iced profile orientations at three incident wind velocities of 10 m/s, 20 m/s and 30 m/s is studied and the results are compared with the predictions using Den-Hartog's instability criterion. The Den-Hartog's instability analysis shows only a small instability zone around $\varphi = \pm 180°$ while the aeroelastic computations show no instability for this particular orientation at incident wind velocities of 10 and 20 m/s. However, at velocity of 30 m/s, the computations reveal a slowly growing instability. Due to zero time-averaged lift at $\varphi = \pm 180°$, this instability is not expected to end up with a large amplitude oscillation.

Moreover, aeroelastic computations show that there is no unstable initial ice orientation for incident wind velocity of 10 m/s. For incident wind velocity of 20 m/s, a large amplitude limit cycle oscillation is observed at $\varphi = \pm 60°$, and for 30 m/s case, unstable zones at $\varphi = \pm 60°$ and $\pm 30°$ are detected, which are not predicted by Den-Hartog's model. In summary, the results show the failure of the Den-Hartog's aerodynamic criterion to predict all potential instability zones and provide evidences that galloping instability is a velocity-dependent and damping-controlled, namely controlled by aerodynamic damping. Hence, accurately predicting the likelihood of galloping instabilities requires an aeroelastic approach.

The final test case was galloping of a single conductor three-span transmission line. The results in terms of frequencies, instability, and galloping ellipse characteristics are in good agreement with the field test; however, due to a very

long CPU time required to complete the 3D simulations, and because of lack of uninterrupted computational resources, comparison of amplitudes were postponed to the future work. It should be noted that the trend of oscillations and behavior of the galloping ellipses are promising, and they show the expected instability nature of the transmission line under study.

4.3 Future work

In order to extend and improve the galloping tool, some potential directions are listed below.

- It is recommended to simulate the presented 3D case for a longer time in order to achieve the final limit cycle.

- As the code is capable of handling bundled cases, it is suggested to complete the bundled test case as well.

- The tool is able to handle wind-induced vibrations of the tall buildings (see [68] for authors publication concerning tall buildings vibration using the present tool). It is proposed to extend this capability and make it user friendly with extended features for more complex problems.

- Currently, the number of Q3D sections is equal to the number of the cable elements, it is recommended to improve the code to make them independent, and eventually decrease the number of fluid sections while increasing the number of cable elements. This will reduce the numerical

computational time and will improve the accuracy of structural solution. Moreover, this independency will give more freedom to users.

- One of the main obstacles during the course of this research was huge CPU-time of the CFD. In fact, in all simulations 99% of the wall time was spent by CFD simulations. Therefore, it is highly recommended to explore the reduced order methods (ROM) to decrease the simulation time and decrease the number of full CFD calculations.

- Once the speed-up gained, the possibility of coupling of the framework with unsteady icing is recommended.

REFERENCES

[1] J.-L. Lilien, P. Van Dyke, J.-M. Asselin, M. Farzaneh, K. Halsan, D. Havard, D. Hearnshaw, A. Laneville, M. Mito, C.B. Rawlins, M. St-Louis, D. Sunkle, A. Vinogradov, "Task Force B2.11.06, State of the art of conductor galloping", Technical Brochure 322. CIGRÉ (International Council of Large Electrical Networks), Scientifc Committee B2 on Overhead Lines, 2007.

[2] "EPRI Transmission line reference book: Wind-induced conductor motion", Electric Power Research Institute, Palo Alto, CA: 2006. 1012317, 2006.

[3] R.D. Blevins, "Flow-induced vibration", Krieger, Malabar, Florida, 1994.

[4] M.P. Païdoussis, S.J. Price, E. de Langre, "Fluid-Structure Interactions - Cross-Flow-Induced Instabilities", Cambridge University Press, 2011.

[5] C. Chen, F., Ballengee, D., B., "Vortex shedding from circular cylinders in an oscillating stream", AIAA journal, 9(2), 340-62, 1971.

[6] M.M. Zdravkovich, "Flow around circular cylinders: a comprehensive guide through flow phenomena, experiments, applications, mathematical models, and computer simulations", Oxford science publications, Oxford University Press, Oxford; New York, 1997.

[7] Y. Zhou, S.X. Feng, M.M. Alam, H.L. Bai, "Reynolds number effect on the wake of two staggered cylinders", Physics of Fluids, 21(12), 125105-14, 2009.

[8] M. Farzaneh, "Atmospheric icing of power networks", Springer, Dordrecht, London, 2008.

[9] A. Borna, Wagdi G. Habashi, G. McClure, "Numerical Study of Influence of Ice Location on Galloping of an Iced Conductor", in "The 2012 Int'l Conference on Advances in Wind and Structures", Korea, Seoul, 2012.

[10] A. Borna, W.G. Habashi, G. McClure, S.K. Nadarajah, "Numerical Modeling of Ice Accretion Effects on Galloping of Transmission Line Conductors", in "9th International Symposium on Cable Dynamics", Shanghai, China, 135-142, 2011.

[11] A. Borna, W.G. Habashi, G. McClure, S.K. Nadarajah, "Numerical investigation of iced-conductor oscillations in the wake of windward conductors", in "Sixth M.I.T. Conference on Computational Fluid & Solid Mechanics", Cambridge, MA, USA, p. 14, 2011.

[12] J.P. Den-Hartog, "Transmission Line Vibration Due to Sleet", Transactions of the American Institute of Electrical Engineers, 51(4), 1074-1076, 1932.

[13] G.V. Parkinson, D. Dicker, "Wind-Induced Instability of Structures [and Discussion]", Philosophical Transactions of the Royal Society of London. Series A, Mathematical and Physical Sciences, 269(1199), 395-413, 1971.

[14] Y. Nakamura, K. Hirata, "Critical geometry of oscillating bluff bodies", Journal of Fluid Mechanics, 208, 375-393, 1989.

[15] G. Parkinson, "Phenomena and modelling of flow-induced vibrations of bluff bodies", Progress in Aerospace Sciences, 26(2), 169-224, 1989.

[16] R.M. Corless, G.V. Parkinson, "A model of the combined effects of vortex-induced oscillation and galloping", Journal of Fluids and Structures, 2(3), 203-220, 1988.

[17] O. Nigol, P.G. Buchan, "Conductor Galloping Part I - Den Hartog Mechanism", IEEE Transactions on Power Apparatus and Systems, PAS-100(2), 699-707, 1981.

[18] O. Nigol, G.J. Clarke, "Conductor Galloping and Control Based on Torsional Mechanism", in "IEEE Power Engineering Society Winter Meeting", Paper No C74016-2, New York, 1974.

[19] O. Nigol, P.G. Buchan, "Conductor Galloping-Part II Torsional Mechanism", IEEE Transactions on Power Apparatus and Systems, PAS-100(2), 708-720, 1981.

[20] Y.M. Desai, A.H. Shah, N. Popplewell, "Galloping Analysis for Two-Degree-of-Freedom Oscillator", Journal of Engineering Mechanics, 116(12), 2583-2602, 1990.

[21] P. Yu, Y.M. Desai, A.H. Shah, N. Popplewell, "Three-Degree-of-Freedom Model for Galloping. Part I: Formulation", Journal of Engineering Mechanics, 119(12), 2404-2425, 1993.

[22] P. Yu, Y.M. Desai, N. Popplewell, A.H. Shah, "Three-Degree-of-Freedom Model for Galloping. Part II: Solutions", Journal of Engineering Mechanics, 119(12), 2426-2448, 1993.

[23] Y.M. Desai, P. Yu, N. Popplewell, A.H. Shah, "Finite element modelling of transmission line galloping", Computers & Structures, 57(3), 407-420, 1995.

[24] X. Wang, Lou, Wen-Juan, "Numerical Approach to Galloping of Conductor", in "The Seventh Asia-Pacific Conference on Wind Engineering", Taipei, Taiwan, 2009.

[25] J. Chadha, W. Jaster, "Influence of turbulence on the galloping instability of iced conductors", IEEE Transactions on Power Apparatus and Systems, 94(5), 1489-1499, 1975.

[26] P. Van Dyke, "Galop Induit sur une Ligne Expérimentale à l'Aide de Profilés en D sur un Conducteur Simple avec ou sans Entretoises Interphases (Galloping Induced on an Experimental Line with D-Shape Profiles on a Single Conductor with and without Interface Spacers)", PhD Thesis, Faculty of Engineering, Department of Mechanical Engineering, Université de Sherbrooke, Sherbrooke (Québec), Canada, 2007.

[27] R. Keutgen, J.L. Lilien, "Benchmark cases for galloping with results obtained from wind tunnel facilities validation of a finite element model", IEEE Transactions on Power Delivery, 15(1), 367-374, 2000.

[28] M. Pomarède, E. Longatte, J.-F. Sigrist, "Numerical simulation of an elementary Vortex-Induced-Vibration problem by using fully-coupled fluid solid system computation", International Journal of Multiphysics, 4(3), 273-291, 2010.

[29] W. Guoxing, W. Shuqing, L. Huajun, "Numerical investigation of vortex-induced vibrations for flow past a circular cylinder", Journal of Ocean University of China (English Edition), 5(2), 174-180, 2006.

[30] C.H.K. Williamson, R. Govardhan, "Vortex-Induced Vibrations", Annual Review of Fluid Mechanics, 36(1), 413-455, 2004.

[31] H. Al-Jamal, C. Dalton, "Vortex induced vibrations using Large Eddy Simulation at a moderate Reynolds number", Journal of Fluids and Structures, 19(1), 73-92, 2004.

[32] E. Guilmineau, P. Queutey, "Numerical simulation of vortex-induced vibration of a circular cylinder with low mass-damping in a turbulent flow", Journal of Fluids and Structures, 19(4), 449-466, 2004.

[33] A. Borna, W.G. Habashi, G. McClure, S.K. Nadarajah, "CFD-FSI simulation of vortex-induced vibrations of a circular cylinder with low mass-damping ", Wind and Structures, 16(5), 411-431, 2013.

[34] W.G. Habashi, "Advances in CFD for in-flight icing simulation", Journal of Japan Society of Fluid Mechanics, 28(2), 99-118, 2009.

[35] W.G. Habashi, M. Aubé, G. Baruzzi, F. Morency, P. Tran, J.C. Narramore, "FENSAP-ICE: A full-3d in-flight icing simulation system for aircraft, rotorcraft and UAVS", in "24th Congress of International Council of the Aeronautical Sciences", Yokohama, Japan 2004.

[36] O.C. Zienkiewicz, R.L. Taylor, J.Z. Zhu, "The finite element method : its basis and fundamentals", Elsevier Butterworth-Heinemann, Oxford; Boston, 2005.

[37] J. Donea, A. Huerta, J.-P. Ponthot, A. Rodríguez-Ferran, "Chapter 14: Arbitrary Lagrangian–Eulerian Methods", in "Encyclopedia of Computational Mechanics", Editors (E. Stein, R.D. Borst, and T.J.R. Hughes), John Wiley, Chichester, West Sussex, 2004.

[38] S.B. Pope, "Turbulent flows", Cambridge University Press, Cambridge; New York, 2000.

[39] R.H. Nichols, "Turbulence Models and Their Application to Complex Flows", Revision 4.01, University of Alabama at Birmingham, 2010.

[40] P.R. Spalart, S.R. Allmaras, "A one-equation turbulence model for aerodynamic flows", AIAA-92-0439, 1992.

[41] J.E. Bardina, Huang, P. G., Coakley, T. J., "Turbulence modeling validation, testing, and development", NASA technical memorandum 110446, National Aeronautics and Space Administration, Ames Research Center; National Technical Information Service, Moffett Field, CA, 1997.

[42] C. Lepage, "A tight two-way fluid-structure coupling for aeroelastic computations in the time domain", PhD, Mechanical and Industrial Engineering, Concordia University, Montreal, 2004.

[43] G.S. Baruzzi, W.G. Habashi, J.G. Guevremont, M.M. Hafez, "A second order finite element method for the solution of the transonic Euler and Navier-Stokes equations", International Journal for Numerical Methods in Fluids, 20(8-9), 671-693, 1995.

[44] G.S. Baruzzi, "A second order finite element method for the solution of the transonic Euler and Navier-Stokes equations", Mechanical and Industrial Engineering, Concordia University, 1995.

[45] Newmerical Technologies Int., "NTI solutions, Manual and test cases for FENSAP-ICE", Newmerical Technologies Int., 2010.

[46] K.-J. Bathe, "Finite Element Procedures", Cambridge, 2006.

[47] J.W. Leonard, "Tension structures : behavior and analysis", McGraw-Hill, New York :, 1988.

[48] W.M. Henohold, J.J. Russell, "Equilibrium and natural frequencies of cable structures (a nonlinear finite element approach)", Computers & Structures, 6(4–5), 267-271, 1976.

[49] K.G. McConnell, C.N. Chang, "A study of the axial-torsional coupling effect on a sagged transmission line", Experimental Mechanics, 26(4), 324-329, 1986.

[50] A.S. Veletsos, G.R. Darbre, "Dynamic stiffness of parabolic cables", Earthquake Engineering & Structural Dynamics, 11(3), 367-401, 1983.

[51] N.M. Newmark, "A method of computation for structural dynamics", Journal of Engineering Mechanics, ASCE, 85 (EM3) 67-94, 1959.

[52] M. Paz, W. Leigh, "Structural Dynamics Theory and Computation", 5th ed., Kluwer Academic Publishers, New York, 2004.

[53] "ADINA Systems online Manuals", ADINA R&D Inc., 71 Elton Ave, Watertown, MA 02472, USA., 2009.

[54] R.K. Jaiman, X. Jiao, P.H. Geubelle, E. Loth, "Assessment of conservative load transfer for fluid-solid interface with non-matching meshes", International Journal for Numerical Methods in Engineering, 64(15), 2014-2038, 2005.

[55] S. Piperno, C. Farhat, B. Larrouturou, "Partitioned procedures for the transient solution of coupled aroelastic problems Part I: Model problem, theory and two-dimensional application", Computer Methods in Applied Mechanics and Engineering, 124(1-2), 79-112, 1995.

[56] C. Farhat, M. Lesoinne, P. Le Tallec, "Load and motion transfer algorithms for fluid/structure interaction problems with non-matching discrete interfaces: Momentum and energy conservation, optimal discretization and application to aeroelasticity", Computer Methods in Applied Mechanics and Engineering, 157(1-2), 95-114, 1998.

[57] R.K. Jaiman, X. Jiao, P.H. Geubelle, E. Loth, "Conservative load transfer along curved fluid-solid interface with non-matching meshes", Journal of Computational Physics, 218(1), 372-397, 2006.

[58] U. Fey, M. Konig, H. Eckelmann, "A new Strouhal-Reynolds-number relationship for the circular cylinder in the range 47 [less-than] Re [less-than] 2 x 10[sup 5]", Physics of Fluids, 10(7), 1547-1549, 1998.

[59] A. Khalak, C.H.K. Williamson, "Dynamics of a Hydroelastic Cylinder with very Low Mass and Damping", Journal of Fluids and Structures, 10(5), 455-472, 1996.

[60] D. Brika, A. Laneville, "Vortex-induced vibrations of a long flexible circular cylinder", Journal of Fluid Mechanics Digital Archive, 250(-1), 481-508, 1993.

[61] A. Khalak, C.H.K. Williamson, "MOTIONS, FORCES AND MODE TRANSITIONS IN VORTEX-INDUCED VIBRATIONS AT LOW MASS-DAMPING", Journal of Fluids and Structures, 13(7-8), 813-851, 1999.

[62] Z.Y. Pan, W.C. Cui, Q.M. Miao, "Numerical simulation of vortex-induced vibration of a circular cylinder at low mass-damping using RANS code", Journal of Fluids and Structures, 23(1), 23-37, 2007.

[63] H. Blackburn, R. Henderson, "Lock-in behavior in simulated vortex-induced vibration", Experimental Thermal and Fluid Science, 12(2), 184-189, 1996.

[64] C.H.K. Williamson, A. Roshko, "Vortex formation in the wake of an oscillating cylinder", Journal of Fluids and Structures, 2(4), 355-381, 1988.

[65] A. Borna, W.G. Habashi, S.K. Nadarajah, G. McClure, "A Computational Aeroelastic Approach to Predict Galloping of Iced Conductors with 3 Degrees of Freedom", in "The 14th International Workshop on Atmospheric Icing of Structures", Chongqing University, China, B2_5_ID163, 2011.

[66] M. Tunstall, L.T. Koutselos, "Further studies of the galloping instability & natural ice accretion on overhead line conductors", in "4th Int. Workshop on Atmospheric Icing of Structures", Paris, 1998.

[67] O. Chabart, J.L. Lilien, "Galloping of electrical lines in wind tunnel facilities", Journal of Wind Engineering and Industrial Aerodynamics, 74-76, 967-976, 1998.

[68] Yue Zhang, Amir Borna, Rooh A. Khurram, Wagdi G. Habashi, "Hybrid RANS/LES method for FSI simulations of tall buildings", in "The 2012 Int'l Conference on Advances in Wind and Structures", Korea, Seoul, 2012.